UNIVERSITÉ DE MONTRÉAL

LEFT VENTRICULAR VIABILITY MAPS: FUSION OF MULTIMODAL IMAGES OF CORONARY MORPHOLOGY AND FUNCTIONAL INFORMATION

PASCALE BÉLIVEAU

INSTITUT DE GÉNIE BIOMÉDICAL

ÉCOLE POLYTECHNIQUE DE MONTRÉAL

MÉMOIRE PRÉSENTÉ EN VUE DE L'OBTENTION

DU DIPLÔME DE MAÎTRISE ÈS SCIENCES APPLIQUÉES

(GÉNIE BIOMÉDICAL)

DÉCEMBRE 2009

UNIVERSITÉ DE MONTRÉAL

ÉCOLE POLYTECHNIQUE DE MONTRÉAL

Ce mémoire intitulé:

LEFT VENTRICULAR VIABILITY MAPS: FUSION OF MULTIMODAL IMAGES OF CORONARY MORPHOLOGY AND FUNCTIONAL INFORMATION

présenté par: BÉLIVEAU Pascale

en vue de l'obtention du diplôme de : Maîtrise ès Sciences Appliquées

a été dûment accepté par le jury d'examen constitué de :

M. MARTEL Sylvain, Ph. D., président

Mme CHERIET Farida, Ph. D., membre et directrice de recherche

M. O'DONNELL Tom, Ph. D., membre et codirecteur de recherche

M. DUONG Luc, Ph. D., membre

DÉDICACE

À mon mari Samuel

et à ma mère Solange

ACKNOWLEDGEMENTS

I would first like to thank my supervisors Farida Cheriet and Tom O'Donnell who guided me throughout this project. Their patience, help and support was much appreciated and I greatly enjoyed working with both of them. They have shared their knowledge in cardiology and medical imaging and I learned a great deal from these topics from both of them. I would also like to thank Gareth Funka-Lea and Frank Sauer for the opportunity that was given to me to complete my work in association with Siemens Corporate Research and spend two internships with them in Princeton, New Jersey. My stay was greatly appreciated and I cherished the contact I had with renowned researchers. Thanks to Drs. Setser and White for their interest and work in this project. Their ideas and interpretation were extremely valuable. Thanks to the members of the jury, Luc Duong and Sylvain Martel for accepting and reviewing the present masters' thesis.

I enjoyed working in the LIV4D laboratory at École Polytechnique de Montréal. Thanks to Philippe Debanné, associate researcher in the lab. I appreciated the acquaintances I made: Rola Harmouche, Lama Seoud, Fouzi Benboujja, Olivier Dionne, Fantin Girard, Jérémie Thériault, Hervé Lombaert, Pascal Fallavollita, Rafik Bourezak, Thomas Hurtut, Kinda Anna Saddi and everyone else who participated in creating a good work environment where the exchange of knowledge was enjoyable. Thanks to Aris Sotiras from École Centrale de Paris for his advice and for discussing my work.

Finally I would like to thank Samuel, my husband, who supported me and gave me valuable scientific advice. Special thanks also go to my mother Solange who always believed in me, for her support and encouragement. Both of them have stood by me through many hours of work. Thanks also to my family, my uncle and aunt and cousins.

RÉSUMÉ

Les maladies coronariennes demeurent encore la première cause de décès aux Etats-Unis étant donné que le taux de mortalité lié à ces maladies enregistré en 2005 est d'une personne sur cinq. Les sténoses (obstructions des artères coronaires) se manifestent par un rétrécissement du diamètre des coronaires, produisant une ischémie soit une réduction du flot sanguin vers le myocarde (le muscle cardiaque). Dans les cas les plus graves, les cellules qui composent le myocarde meurent définitivement et perdent leur fonction contractile. En présence de cette maladie les cliniciens ont recours à l'imagerie médicale pour étudier l'état du myocarde afin de déterminer si les cellules qui le composent sont mortes ou non ainsi que pour diagnostiquer les sténoses dans les coronaires. Actuellement, le clinicien utilise l'imagerie nucléaire pour étudier la perfusion du myocarde afin de déterminer son état. Une projection de cette information sur un modèle segmenté du myocarde, soit le modèle à 17-segments, établie le lien entre les zones atteintes et les coronaires qui sont les plus responsables de leur irrigation. Ce n'est que par la suite, lors d'une angiographie, que le clinicien pourra identifier les sténoses et possiblement intervenir par revascularisation. Une autre méthode de visualisation de la structure coronarienne et de la présence de sténoses est la méthode Green Lane. Le clinicien reproduit la structure des coronaires sur une carte circulaire en se basant sur l'angiographie. L'objectif de notre projet de recherche est de créer un modèle spécifique au patient où il serait possible de voir les territoires coronariens sur la surface du myocarde fusionnés avec la viabilité myocardique. Ce modèle s'adapterait au patient et permettrait l'étude d'autres groupes de coronaires, ce qui n'est pas possible avec le modèle à 17-segments qui est fixe et ne présente que les trois groupes principaux de coronaires (coronaire droite, gauche et circonflexe). De plus, ce modèle divise la surface de l'épicarde en segments à partir de données statistiques qui sont limitées par la nature et la représentativité de l'échantillon de la population considérée et ne permet pas de visualiser la distribution de perte de viabilité sur la surface épicardique.

D'autre part, la disponibilité de volumes d'angiographie par tomodensitométrie (ATDM) permet de visualiser les structures coronariennes en 3D et d'en déduire les territoires associés sur la surface épicardique. En effet cette modalité permet d'obtenir ces structures grâce à un agent de contraste qui rehausse leur visibilité. Les territoires coronariens peuvent alors être déterminés à l'aide d'un algorithme de Dijkstra appliqué sur la surface de l'épicarde en 3D, avec comme point de départ les points surfaciques les plus proches des coronaires. À chaque point est assignée une couleur correspondant à la coronaire qui se trouve la plus proche. Par la suite, nous utilisons des volumes par imagerie par résonance magnétique à rehaussement tardif (IRM-RT). Cette modalité a déjà fait ses preuves en terme de fiabilité lors de l'évaluation de la viabilité du myocarde. Un agent de contraste est administré et persiste dans les zones de perte de viabilité, un phénomène expliqué par l'éjection plus rapide de l'agent de contraste par les cellules saines. La viabilité intra-murale est étudiée entre les deux surfaces du myocarde. Les deux volumes sont obtenus de la Cleveland Clinic aux États-Unis. Avant de projeter les informations sur un modèle circulaire similaire au modèle à 17-segments il faut d'abord établir la correspondance de structures dans les deux modalités. Une méthode de recalage utilise l'ICP ("iterative closest point") pour aligner les modèles de manière rigide dans le sens du grand axe et complète l'alignement de manière manuelle dans le sens du petit axe où un manque de caractéristiques empêche un recalage complet basé seulement sur les modèles surfaciques disponibles. Disposant à la fois des modèles surfaciques du myocarde dans les deux modalités, il est possible d'effectuer un recalage par correspondance de primitives afin de fusionner les informations structurelles et fonctionnelles. Nous avons choisi l'analyse par composante principale pour aligner les modèles surfaciques afin de déterminer la direction de distribution maximale des points dans l'espace 3D. Ce recalage s'est avéré performant pour l'alignement dans le sens du grand axe du cœur par contre le manque de primitives correspondantes dans le sens du

petit axe limite la méthode. Il s'agit de plus d'un recalage rigide alors que le cœur est constamment en mouvement et engendre des déformations non rigides. Les splines d'approximation par plaques minces sont donc utilisées afin d'effectuer un recalage élastique des modèles. De plus, la disponibilité des deux volumes d'intensité permet de compléter le recalage multimodal en se basant sur l'information mutuelle calculée à partir des deux volumes. Une fois le recalage complété en 3D, il est possible de projeter l'information de 3D vers 2D sur une carte et obtenir un modèle complet de territoires coronariens augmenté par la viabilité myocardique. Le clinicien peut donc observer les zones de perte de viabilitié et les associer à un groupe de coronaires responsables de leur irrigation. Notre méthode est comparée à un modèle Green Lane afin d'évaluer les différentes étapes de l'approche proposée. Dans cette méthode le clinicien se réfère à une angiographie pour déterminer la position des coronaires en 3D et reporte cette structure sur une carte circulaire 2D. Afin de faciliter la comparaison, le clinicien a manuellement tracé ce qu'il considère être la bordure des territoires.

Notre évaluation clinique a été effectuée sur des données de 6 patients au total, 4 pour lesquels il était possible de calculer les territoires coronariens, 4 autres pour lesquels la viabilité pouvait être étudiée dans les volumes IRM-RT et 2 pour lesquels les informations structurelles et fonctionnelles étaient disponibles. L'évaluation de l'algorithme de calcul des territoires coronariens s'effectue en comparant les surfaces de territoires obtenus par notre méthode et les surfaces obtenues par la méthode Green Lane. L'aire des surfaces correspondantes est divisée par la surface totale puis multipliée par 100%. La validation de la méthode de recalage se fait de manière qualitative.

Nous avons ainsi réussi à créer une carte continue et spécifique au patient où la perfusion coronarienne du myocarde (et donc les territoires coronariens) est visible et fusionnée avec l'information de viabilité du myocarde. Par défaut de disponibilité de données nous

n’avons pas pu représenter la carte complète pour tous les patients. Par contre, l’évaluation de l’établissement des territoires coronariens a démontré une correspondance moyenne de surface de 87% (évalué sur tous les patients), soit une valeur supérieure au résultat obtenu avec le modèle à 17-segments (78.8%), tous les deux étant comparés à la méthode Green Lane. De plus, la carte finale que nous avons générée permet bien d’associer les zones de perte de viabilité myocardique aux coronaires responsables.

Nous avons réussi à créer un modèle augmenté qui montre à la fois la viabilité et les territoires coronariens sur une même carte continue et spécifique au patient. Cette représentation comporte des limites. Il est possible d’observer de la distorsion sur les anneaux extérieurs de notre modèle. De plus les cliniciens qui ont évalué notre modèle comprennent l’image globale mais éprouvent des difficultés à interpréter la viabilité. Le recalage que nous avons utilisé est de plus limité. Premièrement il est difficile d’assurer une capture des deux volumes au même moment du cycle cardiaque, même lorsque contrôlé avec un électrocardiogramme. La présence d’agent de contraste dans le myocarde d’images IRM-RT et son absence dans les images ATDM (dans cette modalité l’agent n’est présent que dans les coronaires, rend le recalage par information mutuelle plus difficile. De plus le modèle de déformation élastique que nous utilisons est déduit à partir de la surface du myocarde et donc ne tient pas compte des voxels avoisinants. Les résultats qualitatifs que nous obtenons indiquent un recalage optimal mais les différences entre les solutions de déformations possibles sont souvent non significatives, ce qui nous pousse à croire que nous détectons un recalage maximal sans pouvoir obtenir un niveau de précision satisfaisant. La méthode d’identification des artères coronaires reste à raffiner puisque la segmentation de ces structures est effectuée manuellement par un expert.

ABSTRACT

Coronary heart disease (CHD) can be attributed to the build up of plaque in the coronary arteries (atherosclerosis) which leads to ischemia, an insufficient supply of blood to the heart wall, which results in myocardial dysfunction. When ischemia remains untreated an infarction may appear (areas of necrosis in cardiac tissues) and consequently the heart's contractility is affected, which may lead to death. This disease is the basis of one of every five deaths in the United States during 2005, elevating this disease to the largest cause of death in United States. In standard clinical practice, perfusion and viability studies allow clinicians to examine the extent and the severity of CHD over the myocardium. Then, by consulting a population-based coronary territory model, such as the 17-segment model, the clinician mentally integrates affected areas of myocardium, found in nuclear or magnetic resonance imaging, to coronaries that typically irrigate this region with blood. However, population-based models do not fit every patient. There are individuals whose coronary tree structure deviates from that of the majority of the population. In addition, the 17-segment model limits the number of coronary groups to three: left coronary artery (LAD), right coronary artery (RCA) and left circumflex (LCX). Moreover this map is not continuous; it divides the myocardial surface in segments.

Our objective is therefore to create a patient-specific map explicitly combining coronary territories and myocardial viability. This continuous model would adapt to the patient and allow the study of groups of coronary unavailable with standard models. After having identified loss of viability, the clinician would use this model to infer the most likely obstructed coronary artery responsible for myocardial damage. Visualization of the loss of viability along with coronary structure would replace the physician's task of mentally integrating information from various sources.

Anatomic (or structural) information of the heart is available with Computer Tomography Angiography (CTA). A contrast agent is administered through the arm and spreads until it reaches the coronaries. A CT scan is performed at that moment and coronaries appear bright on the resulting images. The surfaces of the myocardium (epicardium and endocardium) are identifiable and coronary anatomy of individual patients can be determined by experienced physicians. Once the coronary arteries and LV surface is recovered, coronary territories can be computed over the epicardial surface using the Dijkstra algorithm. This method finds the shortest path from a source point, a point on a coronary projected onto the LV surface, to all other point of the surface. Each point on the surface is then assigned a label corresponding to the closest coronary.

Cardiac function may be inferred from Delayed Enhancement Magnetic Resonance (DEMR) images. In this protocol, a contrast agent is administered to the patient and image acquisition is done after a known delay corresponding to the wash out rate of healthy myocardial cells. After that delay, any cells still retaining the contrast agent are considered dead. This phenomenon is hypothesized to be caused by the slow wash out rate of dead cells. Thus, bright areas of the myocardium indicate a possible site of scar.

Fusion of both modalities (CTA and DEMR) is needed in order to guarantee the correspondence of structure and function in the final map. We chose to accomplish an initialization of registration by Principal Component Analysis (PCA) which determines and aligns the directions of maximal variance of two clouds of points (the surface points of the LV in both modalities). As a result, the LV in both DEMR and CTA images are roughly lined up in 3D.

This rough estimation of the registration suffers from two drawbacks. First, it is a rigid registration and the heart deforms non-rigidly. Second, the LV is rotationally symmetric in the short axis plane so this aspect of the alignment may not be correct. Once the DEMR and CTA images have been roughly aligned by PCA, we can proceed to a

more precise registration and exploit the intensity information contained in each available volume with mutual information. Thin plate spline (TPS) fitting consists of finding a deformation according to given source and target landmarks. We apply it to obtain an elastic registration of myocardial surfaces. Once a 3D registration has been completed, a projection can be performed from 3D to 2D. Thus, a complete model is obtained where coronary territories are overlaid with viability information for a specific patient.

Clinical evaluation was done over 6 patients. Coronary territories could be computed for four of them and viability information was available for four others. Both structural and functional information was available for two patients. Validation for our computed coronary territories was done by a comparison with the Green Lane method. In this method, given a coronary angiogram of the patient, the coronary arteries and branch vessels are transcribed onto a standard diagram by an expert cardiovascular imager and resulting coronary territories are drawn by an expert. By employing the Green Lane method to create ground truth we were able to quantify the correctness of both our territory map as well as the 17-segment model. Overall, the average percent correlation between our CTA-derived maps and the ground truth was 87%. The 17-segment model comparison resulted in a correlation of 79%. Registration was evaluated qualitatively.

We achieved our goal of creating a patient-specific coronary territory map fused with a viability map which presents the functional as well as structural information of interest to the clinician for the diagnosis of CHD. While the presented results are an improvement over the 17-segment model, some criticism can be formulated for each step of our method and there is place for improvement at different levels. First, distortion is seen from the projection of texture from 3D to 2D. The texture is therefore altered and the physician has to be made aware of this fact. Second, since both images are from different modalities and acquired at differing times, it is hard to guarantee that the images

represent the exact same time in the cardiac cycle even if ECG gaiting is performed. Third, the presence of contrast agent in the myocardium in DEMR images and the absence of this agent in the myocardium (though not the coronaries) in CTA make it harder to have a registration method that is intensity-based. Finally, the registration is directly dependant on the quality of the segmentation in both modalities and our deformation model applies only to surface points.

In conclusion, our fused model showing myocardial viability and coronary structure should allow the clinician to establish a correspondence between a loss of viability and a specific coronary. Moreover our method allows the clinician to associate a territory with any branch vessel. Although there are some improvements to bring to the model, we have advanced with regards to the previous methods. Further development of the method could lead to a diagnosis tool usable in clinical practice in the presence of CHD.

CONDENSÉ

Introduction

Les maladies du cœur peuvent être causées par l'accumulation de plaque à l'intérieur des artères coronaires (on parle d'athérosclérose) [1]. On nomme sténose le rétrécissement causé par cette accumulation. Cet état peut mener à une ischémie : une insuffisance du volume de sang acheminé vers le muscle cardiaque (le myocarde). Non traité, il peut mener à une nécrose du myocarde (la mort des cellules du muscle) et la contraction du muscle cardiaque peut s'en trouver affectée. Puisque le cœur pompe le sang vers le reste du corps, une dysfonction du myocarde peut mener à la mort du patient. Les maladies coronariennes ont causé la mort d'une personne sur 5 durant l'année 2005, la plaçant au premier rang des causes de décès au Etats-Unis [2]. La revascularisation est une procédure qui tente de rétablir le flot sanguin vers le muscle cardiaque dans le but de retrouver les contractions cardiaques normales du cœur.

En présence de maladie coronarienne, l'imagerie médicale peut assister le clinicien lors du diagnostique. Il cherche à connaître l'état du myocarde et plus spécifiquement l'état du ventricule gauche (VG) afin de déterminer si les cellules qui le composent sont viables ou non. En effet, la revascularisation est une procédure qui ne sera bénéfique que pour les patients dont les cellules cardiaques sont encore viables et qui peuvent donc récupérer leur fonction de contraction. La revascularisation n'est considérée que dans les cas ou une récupération du myocarde est possible. Les connaissances sur la viabilité du myocarde peuvent donc aider au niveau préopératoire afin de planifier la procédure d'intervention ou dans le but de tenter de prédire les résultats de l'intervention.

Le clinicien a alors recours à de l'imagerie fonctionnelle tel l'imagerie nucléaire ou par résonance magnétique pour étudier l'état du myocarde. Le clinicien cherche ensuite à localiser les sténoses qui peuvent être la cause des dommages au muscle cardiaque. Afin de faire ce lien les cliniciens utilisent couramment un modèle, le modèle à 17-segments [34], qui établie une association entre la surface du myocarde et un groupe d'artères coronnariennes. Ce modèle est basé sur un modèle probabiliste de la distribution des coronaires sur le myocarde en se basant sur la population en générale. Suite à ceci le clinicien a souvent recours à une angiographie afin de déterminer la structure coronarienne du patient et localiser les sténoses dans les coronaires. Cette modalité d'image permet d'observer l'agent de contraste se propageant dans les artères, en visualisant la distribution et le diamètre. Un rétrécissement ou même l'arrêt de propagation de l'agent se produit en présence d'athérosclérose. La structure des coronaires peut être étudiée avec la méthode Green Lane. En observant une angiographie le clinicien dessine la structure coronarienne sur un diagramme circulaire et peut aussi y tracer des territoires coronariens (voir Figure 1). Au cours de l'angiographie le clinicien peut aussi effectuer la revascularisation.

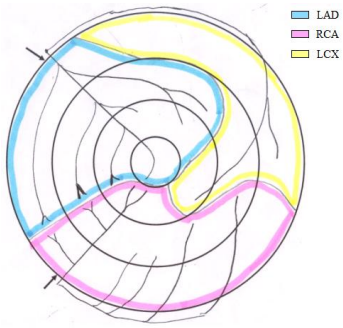

Figure 1 : Diagramme résultant de la méthode Green Lane. Le tracé bleu indique les bordures du territoire associé au groupe de coronaires gauches, le jaune à la coronaire circonflexe et le rose à la coronaire droite.

Notre objectif de recherche est de créer un modèle d'assistance au clinicien lors du diagnostique afin de lui permettre d'étudier la perfusion du myocarde par les coronaires, et donc de connaître la forme de l'arbre coronarien d'un patient tout en visualisant l'étendue de la perte de viabilité du myocarde. Ce modèle serait un modèle spécifique au patient, un avantage par rapport au modèle à 17-segments utilisé présentement et qui est basé sur une moyenne de la distribution des coronaires dans la population. Ce modèle ne tient pas compte des variations qu'il est possible d'observer dans la structure coronarienne d'un patient à l'autre [38]. Il suppose par exemple une structure coronarienne à dominance droite alors que qu'elle peut être de dominance gauche ou de codominance pour certains patients [38]. La structure coronarienne est visible à l'aide d'angiographie par tomodensitométrie (ATDM), une modalité qui rehausse les coronaires par administration d'agent de contraste lors d'une acquisition par tomodensitométrie (TDM). Nous voulons de plus utiliser la modalité par résonance magnétique avec rehaussement tardif (IRM-RT) afin de limiter l'exposition du patient à des agents radioactifs. En effet, l'IRM-RT a été reconnue comme étant une modalité d'imagerie fiable pour l'étude de la viabilité myocardique [90] et est de plus non invasive (comparée à une angiographie par exemple). Afin d'obtenir un modèle augmenté il faut préalablement effectuer un recalage des volumes disponibles. En effet, sans recalage les

informations seraient projetées de manière indépendante et le clinicien pourrait obtenir de l'information erronée concernant une coronaire faussement associée à une perte de viabilité myocardique. Le cœur étant constamment en mouvement, l'électrocardiogramme ne garantie pas l'acquisition des images au même instant du cycle cardiaque. Les approches conventionelles pour le recalage de ces deux volumes appliquent l'algorithme ICP ("Iterative Closest Point") sur des modèles surfaciques disponibles dans les deux modalités. Cette méthode consiste à mettre en correspondance deux modèles de surface en se basant sur un calcul de distance minimale entre les surfaces et points qui les composent [3]. Le recalage est complété de manière manuelle afin d'assurer une correspondance d'orientation dans le sens du petit axe, ce qui ne peut être accompli de façon automatique pour cause de manque de caractéristiques dans cette direction. Nous cherchons donc de plus à automatiser ce processus.

Revue de littérature

Suite à une étude de la viabilité myocardique, le clinicien a recours à un modèle d'association de régions du myocarde à un groupe d'artères coronariennes. Le modèle à 17-segments a été recommandé par l'AHA et est présenté à la figure 2. Chaque cercle concentrique du modèle correspond à un niveau d'élévation par rapport à l'apex tel que montré à la figure 2. Ce modèle divise le myocarde en segments, chacun associé à un groupe d'artères : la partie inférieure gauche (segments 3, 4, 9, 10, et 15) coloré de brun est associée à la coronaire droite, la partie supérieur gauche (segments 1, 2, 7, 8, 13, 14 et 17) de couleur bleu à la coronaire gauche et celle de droite en vert à la circonflexe (segments 5, 6, 11, 12 et 16). Ce modèle est construit à partir de la population mais ne reflète pas l'arbre coronarien d'un patient spécifique. Il existe en effet certaines personnes pour qui des segments ne correspondent pas aux coronaires associées par le modèle [38].

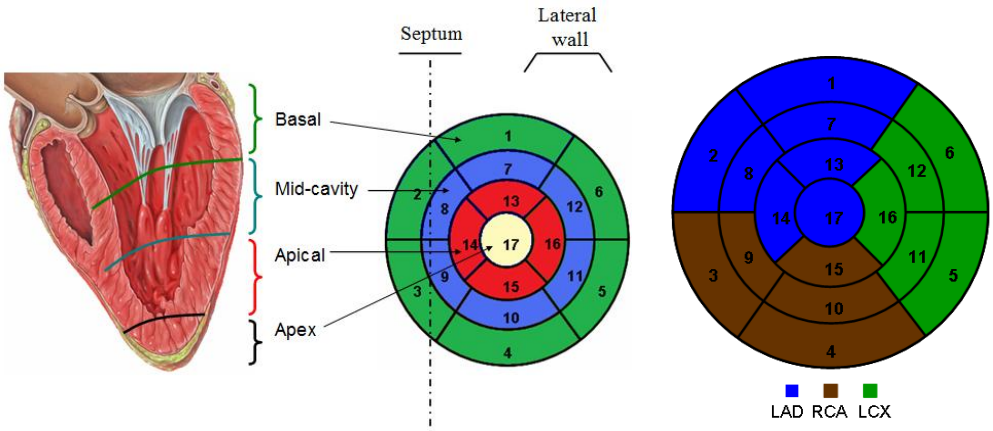

Figure 2 : Explication (image de gauche) et modèle originale (image de droite) à 17-segments.

Différentes modalités d'images existent pour assister le clinicien lors du diagnostique. Les structures anatomiques sont visibles à l'aide de l'ATDM. Un agent de contraste est administré au patient au travers du bras et se propage jusqu'aux artères coronaires. Un scan CT est effectué au moment où l'agent de contraste se trouve dans les coronaires et elles apparaissent donc plus claires dans les images résultantes. Il est ainsi possible de visualiser la structure tridimensionnelle de l'arbre coronarien. Cette modalité ne permet pas d'étudier l'état du myocarde et le clinicien a recours à de l'imagerie fonctionnelle où les effets de la maladie sur le muscle sont visibles. L'imagerie par résonance magnétique (IRM) avec rehaussement tardif (IRM-RT) peut être utilisée. L'emphase est mise sur les tissues morts dans les images. L'avantage de l'IRM-RT sur l'imagerie nucléaire est de limiter l'exposition du patient à des agents ionisants. Elle est de plus non invasive en comparaison à l'angiographie par exemple. L'IRM-RT utilise un agent de contraste qui persiste dans les zones de pertes de viabilité, au contraire des autres cellules dont on présume une éjection plus rapide du produit de leur environnement.

Des vues spécifiques sont définies lors de l'étude d'images cardiaques. Deux sont dans le sens du grand axe (la direction dans laquelle le ventricule gauche est le plus long) et une dans le sens du petit axe dans laquelle le ventricule gauche semble circulaire. Le ventricule droit et gauche sont visibles dans la vue du grand axe horizontal mais seule le VG est visible dans la vue du grand axe verticale.

Recalage multimodal d'images médicales de structures cardiaques

Il existe deux catégories de méthodes de recalage d'images médicales [119]: par correspondances de primitives ou d'intensités [124]. La première exploite les formes géométriques et nécessite la sélection de points de contrôles ou la segmentation d'organes. Il est possible de se fier à des segmentations telle la segmentation de l'endocarde et de l'épicarde. Par contre, le recalage ne pourra se faire que dans le sens du long axe puisqu'aucun repère du myocarde ne permet d'associer correctement les deux segmentations dans le sens du petit axe du cœur. Les faibles variations de courbures dans le sens du petit axe ne peuvent pas être exploitées. En effet, le muscle cardiaque est constamment en mouvement et se déforme. Il est impossible de garantir que deux acquisitions de modalités différentes soient prises au même instant du cycle cardiaque, même sous contrôle avec électrocardiogramme. De plus les patients souffrant de maladies cardiovasculaires peuvent avoir un VG de forme altéré due à la maladie. Seuls les points d'insertion, qui sont les points d'encrage du ventricule droit sur le gauche, sont disponibles, mais ceci nécessiterait la segmentation du ventricule droit. La méthode de recalage avec analyse par composante principale (ACP) a déjà été exploitée avec succès [126]. Cette méthode calcule la direction de dispertion maximale de points dans un espace 3D à partir d'une matrice de covariance créée à partir d'une matrice de position 3D des points des modèles disponibles dans les deux modalités. Il s'agit d'un recalage rigide.

Afin de mettre en correspondance les deux modèles, un champ de déformation peut être appliqué en exploitant le modèle des splines plaque mince [168], [169]. Il s'agit d'une méthode de recalage élastique qui s'effectue en se basant sur un ensemble de points de contrôles correspondants. Le champ de déformation est trouvé en cherchant à minimiser l'énergie nécessaire afin de courber une plaque mince à partir d'une position initiale vers une destination connue. L'énergie en une position (*x,y*) sur une plaque mince est proportionnelle à la dérivée seconde en un point hors du plan : $\left(\frac{\partial^2 z}{\partial x^2}\right)^2 + 2*\left(\frac{\partial^2 z}{\partial x \partial y}\right)^2 + \left(\frac{\partial^2 z}{\partial y^2}\right)^2$ où *z* est une fonction de *x* et de *y* et dépend des positions des points de contrôles et est définie par une fonction de base *U* qui minimise : $\iint_{\Re^2}\left(\left(\frac{\partial^2 z}{\partial x^2}\right)^2 + 2*\left(\frac{\partial^2 z}{\partial x \partial y}\right)^2 + \left(\frac{\partial^2 z}{\partial y^2}\right)^2\right) dxdy$. La généralisation décrit des composantes u_k avec des points sources et destinations et *n* est le nombre de points sources. Il faut donc minimiser une somme individuelle de composantes d'après :

$$J_m^d(u) = \sum_{k=1}^{d} J_m^d(u_k) \qquad \text{et} \qquad J_m^d(u_k) = \sum_{\alpha_1+\ldots+\alpha_d=m} \frac{m!}{\alpha_1!\ldots\alpha_d!} \int_{\Re^4} \left(\frac{\partial^m u_k}{\partial x_1^{\alpha_1} \ldots \partial x_d^{\alpha_d}} \right)^2 dx .$$

Une fois le maximum obtenu à partir du recalage par correspondance de primitives il faut encore exploiter le recalage par correspondance d'intensités. Ce calcul se base sur les valeurs d'intensités contenues dans l'image afin de faire une étude statistique de leur distribution dans chacune des images. L'information mutuelle utilise le calcul d'entropie, soit $H = -\sum_i p_i \log p_i$, où p_i est la probabilité d'occurrence d'une intensité dans une image, et le calcul de probabilité jointe, soit $H(A,B) = -\sum P_{A,B}(a,b) \log(P_{A,B}(a,b))$, où

$P_{A,B}(a,b)$ est la probabilité d'avoir l'intensité *a* dans l'image *A* et l'intensité *b* dans l'image *B* à une même position relative. Ces probabilités sont évaluées à partir d'histogrammes.

Objectifs de recherche

L'objectif principal est donc de représenter les zones de perfusion myocardique des coronaires dans le cas de patients soufrant de troubles cardiaques causés par des maladies coronariennes à partir de volume ATDM, couplé avec de l'information fonctionnelle de la viabilité myocardique obtenue à partir d'un volume IRM-RT. Un recalage de surfaces provenant des deux modalités permet donc d'établir la fusion de l'information structurelle et fonctionnelle afin de visualiser l'ensemble de l'information intégrée sur une carte circulaire à deux dimensions. Le premier objectif est donc de déterminer les territoires coronariens sur la surface du myocarde à partir de surfaces du VG et de la segmentation de coronaires dans un volume ATDM. Le deuxième objectif est l'obtention d'une fusion des deux modalités qui implique un recalage de la surface du cœur en utilisant les modalités CT et IRM en trois dimensions. Ceci est accompli dans un premier temps en se basant sur la segmentation des surfaces myocardiques à partir d'un volume ATDM et d'un volume IRM-RT puis en se basant sur les intensités contenues dans les volumes. Le troisième objectif consiste à obtenir une carte de viabilité myocardique établie à partir de la segmentation des surfaces du myocarde (épicarde et endocarde) dans un volume IRM-RT recalé. Le dernier objectif est la projection simultanée des territoires coronariens ainsi que de la viabilité du myocarde sur une carte circulaire en 2D, similaire au modèle 17-segments présentement utilisé en clinique. Cette carte permettra d'associer les tissus cardiaques affectés aux artères coronariennes qui les irriguent. Les étapes sont décrites à la figure 3.

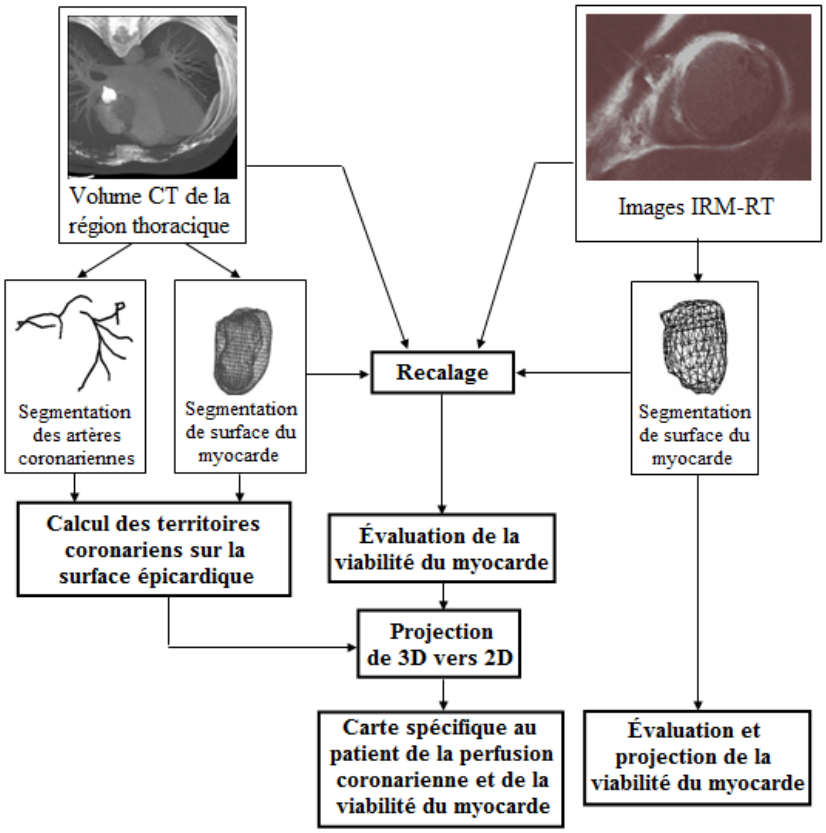

Figure 3 : Étapes de création d'une carte spécifique au patient montrant à la fois la viabilité du myocarde et les territoires coronariens.

Méthodologie

Les acquisitions des volumes ATDM sont produites par un scanner Sensation 16/64 (Siemens Medical Solution, Forcheim, Allemagne). Pour tous les patients une segmentation de l'épicarde et de l'endocarde est obtenue. Une segmentation des coronaires est fournie sous forme de liste de points identifiés manuellement par un cardiologue expérimenté. Les points des coronaires sont disponibles sous trois groupes soient : 1) coronaire gauche (CG), 2) coronaire droite (CD) et 3) coronaire circonflexe (CX). Le clinicien peut fournir d'autres groupes de coronaires s'il le désire. Ceci offre

l'avantage d'étudier l'irrigation du myocarde par des branches de coronaires principales. Afin de déterminer les territoires coronariens, nous avons premièrement utilisé un algorithme de croissance de région en choisissant comme points sources les points du modèle surfacique les plus proches des coronaires fournies. Une expansion progressive des régions se produisaient. Cette approche s'est avérée longue et de plus comportaient le défaut d'associer un point de la surface au groupe de coronaires dont la région l'atteignait en premier, ne tenant pas compte des distances sur la surface. Afin de palier à ces limites, nous avons plutôt choisi d'exploiter l'algorithme de Dijkstra qui calcule les distances sur des surfaces géodésiques à partir d'un point source. Nous avons donc fait le calcul de distance pour chaque point de contrôle par rapport à tous les autres points du modèle. L'association d'un point se fait à la coronaire la plus proche et la couleur de celle-ci lui est assignée (CG en bleu; CD en rouge; CX en vert; branches en jaune). Nous obtenons ainsi une surface tridimensionnelle subdivisée en régions coronariennes.

Le recalage des modèles surfaciques segmentés dans les deux modalités permettra de fusionner la structure des coronaires et la viabilité du myocarde. Une initialisation est accomplie à l'aide d'une ACP qui met en correspondance les modèles provenant de deux modalités différentes. Une suite de déformations élastiques suivie par des transformations dans l'espace est effectuée et comparée à l'aide d'un calcul d'information mutuelle. Les valeurs d'informations mutuelles sont comparées une fois l'algorithme terminé et la valeur maximale obtenue est celle indiquant la meilleure transformation. Une transformation est composée d'une translation du point centrale du VG et d'une rotation autour du long axe du cœur tel que présenté à la figure 5. Les limites du domaine de transformation sont déterminées de manière empirique : 1/8 de la distance du myocarde dans le sens du grand axe, 1/4 dans le sens du petit axe (toutes directions confondues) et 20^{o} d'inclinaison maximale du modèle par rapport au long axe.

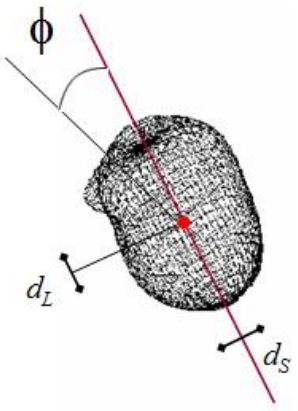

Figure 5 : Domaine de transformation lors du calcul de l'information mutuelle.

La viabilité du myocarde est visible dans des volumes IRM-RT en analysant les intensités du signal des images. Les images ont été acquises à l'aide d'une machine à 1.5 Tesla de modèle Sonata (Siemens Medical Solutions, Erlangen, Allemagne). Les images sont acquises environ 20 minutes après avoir administré l'agent de contraste. L'étude de la viabilité est effectuée de manière trans-murale (c'est-à-dire entre l'épicarde et l'endocarde) en analysant les intensités contenues dans le volume IRM-RT. Les intensités traversées entre un point du modèle de l'endocarde et son homologue sur l'épicarde en termes de coordonnées polaires (voir figure 4) sont cumulées et restent intactes.

Figure 4 : Évaluation de la viabilité trans-murale à l'aide de modèles segmentés et identification des coordonnées polaires de chaque point.

La projection des territoires coronariens et la viabilité du myocarde recalé sur une carte circulaire 2D se fait par projection de coordonnées polaires 3D en 2D. Les anneaux de différentes élévations par rapport à l'apex sur le myocarde sont projetés sur le disque à une distance proportionnelle du centre tel que montré à la figure 6. Cette projection place le septum vers la gauche du disque et la disposition des coronaires est similaire au modèle à 17-segments (voir figure 6). Le recalage établi entre les volumes permet de conserver la correspondance de régions entre les deux modalités sur la carte 2D suite à la projection.

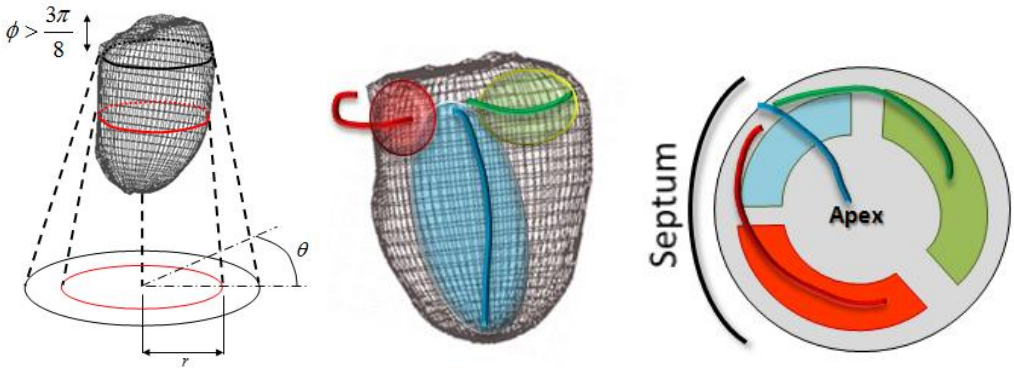

Figure 6 : Projection 3D vers 2D (image de gauche) et orientation du modèle projeté (image du milieu et de droite).

Résultats

Les territoires coronariens sur la surface du myocarde ont été calculés en 3D puis projetés vers la carte 2D. Les résultats pour le patient 1 et 2 sont montrés à la figure 7. Un quatrième groupe est formé par une branche de la CG pour le patient 1. Le tableau 1 compare les territoires coronariens calculés selon notre méthode avec le modèle de territoires obtenu à l'aide de la méthode Green Lane. Par la suite le même calcul est effectué pour comparer le modèle 17-segments au modèle Green Lane. L'aire des surfaces correspondantes est divisée par la surface totale puis multipliée par 100%.

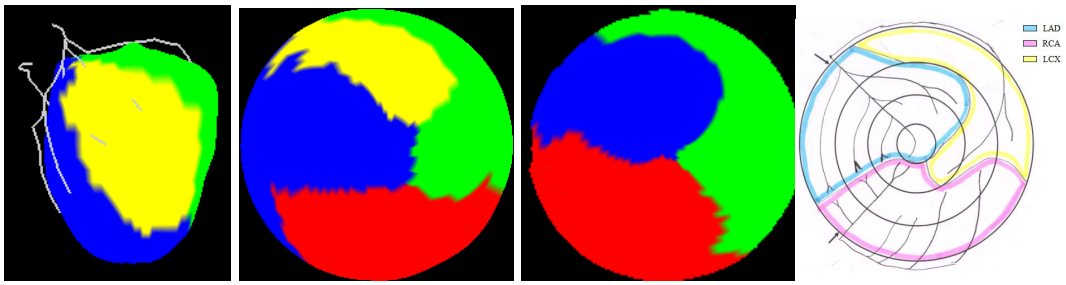

(a) (b) (c) (d)

Figure 7 : Territoires pour le Patient 1 en 3D et sur une carte 2D avec quatre groupes de coronaires (a,b) et pour le patient 2 selon notre méthode (c) comparé au résultat de la méthode Green Lane.

Tableau 1 : Comparaison en pourcentage de correspondance des territoires coronariens calculés selon notre méthode ainsi que le modèle à 17-segments avec le résultat de la méthode Green Lane.

	Calculé vs. Green Lane	**17-segment vs. Geen Lane**
Patient 1	95.28	79.10
Patient 2	83.14	73.00
Patient 3	87.17	81.70
Patient 4	84.80	81.40
Moyenne	87.59	78.80

Un exemple de recalage rigide par PCA est montré à la Figure 8. Une déformation des modèles par TPS est montré à la Figure 9. L'alignement des volumes avant le recalage final est montré à la figure 10 suivit par un exemple de résultat final de recalage obtenu à l'aide de l'information mutuelle (Figure 11).

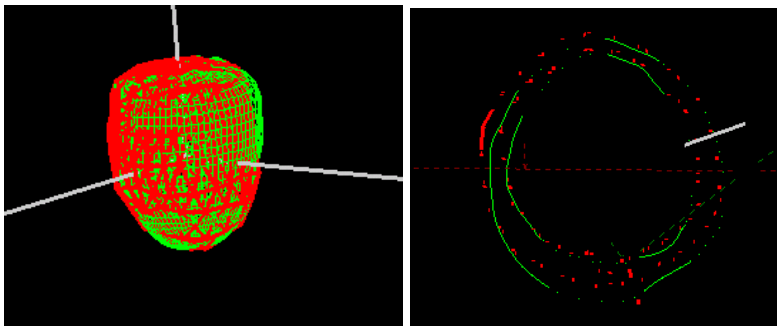

Figure 8 : Modèles surfaciques suite au recalage par analyse de composantes principales. Le modèle rouge indique la surface dans l'IRM-RT et le vert dans le volume CT.

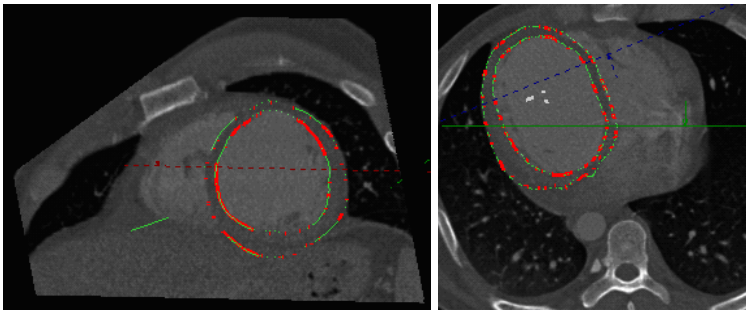

Figure 9: déformation des modèles surfacique suite à TPS.

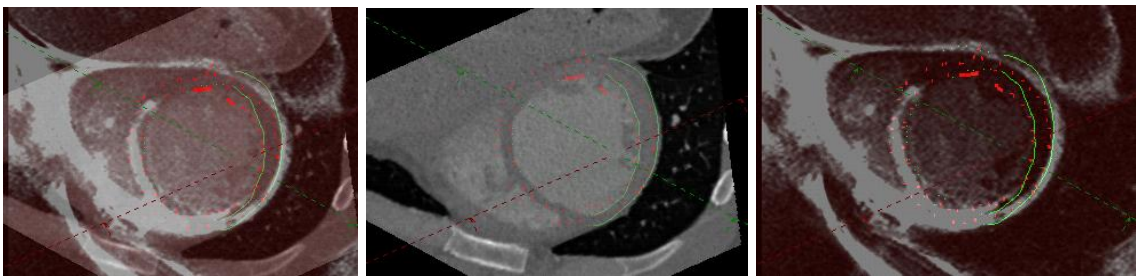

(a) (b) (c)

Figure 10 : Aligment avant recalage par information mutuelle pour le patient 1 : les deux volumes superposés (a), CT (b) et IRM-RT (c).

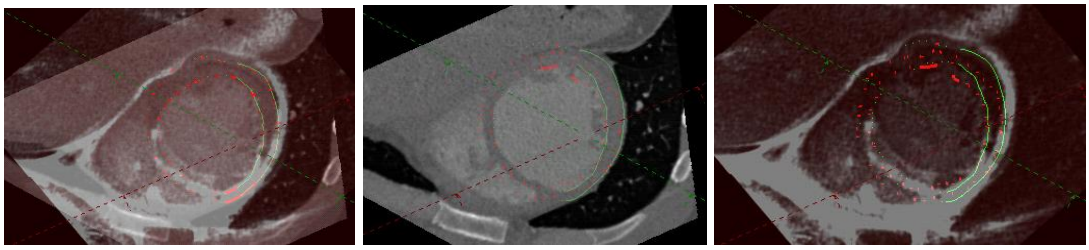

(a) (b) (c)

Figure 11 : Résultat final de recalage pour le patient 1 : les deux volumes superposés (a), CT (b) et IRM-RT (c).

Les résultats de projection de viabilité sont montrés à la figure 12 pour les patients 1, 3, 5 et 6. Dans le cas où le modèle surfacique couvre une surface qui dépasse les limites du volume DEMR, certains points ne peuvent pas se faire assigner une intensité vue l'absence d'information de viabilité. Ceci correspond à la section bleu sur les modèles de viabilité. La carte de perfusion coronarienne du myocarde jumelée à la projection de viabilité est montrée pour deux patients à la figure 13. Il est possible de percevoir une perte de viabilité au niveau de la CG pour le patient 1 (figure 13 a), ce qui est effectivement le cas chez ce patient qui a un blocage à 70% de cette coronaire.

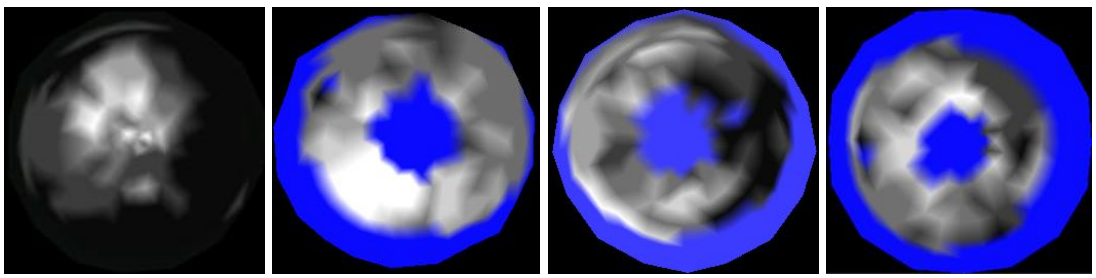

Figure 12 : Carte de viabilité pour les patients 1, 3, 5 et 6.

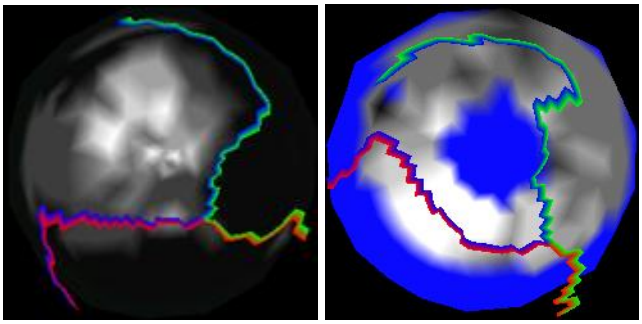

(a) (b)

Figure 13: Modèle de perfusion coronarienne du myocarde sur la viabilité myocardique trouvé selon notre méthode pour le Patient 1 (a) et pour le Patient 3 (b).

Conclusion

Nous avons réussi à créer une carte spécifique au patient où la perfusion coronarienne du myocarde (et donc les territoires coronariens) est visible et fusionnée avec l'information de la viabilité du myocarde. Par manque de disponibilité de données nous n'avons pas pu représenter la carte complète pour tous les patients. Les territoires obtenus pour les patients correspondent en général au modèle obtenu par le clinicien à l'aide de la méthode Green Lane. De plus la carte finale permet bien d'identifier les zones de perte de viabilité myocardique en les associant aux coronaires responsables de leur irrigation. Par contre, il est possible d'observer de la distorsion sur les anneaux extérieurs de notre modèle. De plus, les cliniciens qui ont évalué notre modèle comprennent l'image globale mais éprouvent des difficultés à interpréter la viabilité. Le recalage que nous avons utilisé est de plus limité. Premièrement il est difficile d'assurer une capture d'image au même instant du cycle cardiaque, même lorsque contrôlé avec un électrocardiogramme. La présence d'agent de contraste dans le myocarde d'images IRM-RT et son absence pour les images ATDM (dans cette modalité il n'est présent que dans les coronaires) rend le

recalage par information mutuelle plus difficile. De plus le modèle de déformation que nous utilisons est déduit à partir du myocarde et ne tient donc pas compte des voxels avoisinants.

Les résultats qualitatifs que nous obtenons indiquent un recalage optimal mais les différences entre les solutions de déformations possibles sont souvent non significatives, ce qui nous pousse à croire que nous détectons un recalage maximal sans pouvoir obtenir un niveau de précision satisfaisant. La méthode d'identification des artères coronariennes reste à raffiner puisque la segmentation de ces structures est effectuée manuellement par un expert.

TABLE OF CONTENTS

LIST OF TABLES

LIST OF FIGURES

LIST OF APPENDICES

LIST OF ABBREVIATIONS

AHA	American heart association
AV	Atrioventricular node
BMS	Bare metal stent
CABG	Coronary artery bypass graft
CAD	Computer aided diagnosis
CT	Computer tomography
CTA	Computer tomography angiography
CHD	Coronary heart disease
DEMR	Delayed enhancement magnetic resonance
DES	Drug eluting stent
DICOM	Digital imaging and communications in medicine
ECG	Electrocardiogram
GPU	Graphical processing unit
GPVI	Generalized partial volume interpolation
IVUS	Intravascular ultrasound
LAD	Left anterior descending
LCX	Left circomflexe
LV	Left ventricle
MDCT	Multidetector computer tomography

MI	Mutual information
MPR	Multi-planar reconstruction
MR	Magnetic resonance
NN	Nearest neighbor
ONCAB	On-pump coronary artery bypass
OPCAB	Off-pump coronary artery bypass
PCA	Principal component analysis
PDA	Posterior descending artery
PET	Positron emission tomography
PTCA	Percutaneous transluminal coronary angioplasty
PVI	Partial volume interpolation
RA	right atrium
RCA	Right coronary artery
RF	radio frequncy
RV	Right ventricle
SA	Sinoatrial node
SAN	Short axis normal
SPECT	Single photon emission computer tomography
TMR	Transmyocardial laser revascularization
TPS	Thin plate spline
US	Ultrasound

INTRODUCTION

Coronary heart disease (CHD) can be due to the build up of plaque in the coronary arteries (atherosclerosis) [1] which leads to ischemia, an insufficient supply of blood to the heart wall, which results in myocardial dysfunction. When ischemia remains untreated an infarction may appear (areas of necrosis in cardiac tissues) and consequently the heart's contractility is affected. Since the left ventricle (LV) of the heart is responsible for forcing the blood to the entire body, myocardium (heart wall) dysfunction can therefore lead to death. Cardiovascular diseases account for 33.5% of all deaths that occurred in United States in 2005 and CHD is the cause of one of every five deaths that occurred during that year raising this disease as the largest cause of death in United States [2]. Revascularization therapy is an intervention that tries to reestablish a normal blood flow through coronary arteries in an attempt to recover contractile function of the heart wall.

In the context of CHD, medical imaging assists clinicians through computer aided diagnosis (CAD). Knowledge of myocardium viability is helpful prior to any intervention for planning purposes and for predicting the outcome of procedures. Revascularization therapy is only considered when there is hope of recovery for the myocardium. States of the myocardium in case of CHD are hibernation, stunning or scarring [42]. In the first case, the myocytes lessen their contractile activity due to the reduction in blood flow affecting the heart's overall contractility. Stunning is a state of myocardium dysfunction which follows a period of ischemia. In this case recovery of myocardial cells contraction is possible. For scarring, the myocytes are permanently damaged and will never recover their contractile property [36]. Perfusion and viability studies allow clinicians to examine the extent and the severity of CHD over the myocardium. Aided by a population-based model, the clinician can relate affected areas of myocardium to coronaries that typically

irrigate this region with blood. However, this model does not fit to every patient whose coronary tree structure might deviate from that of the majority of the population.

After assessing myocardial dysfunction, the clinician can proceed to a catheterization to locate coronary lesions. This consists in inserting a guide wire into the patient's artery until it reaches the origin of the heart's coronaries. While a series of X-rays is being captured, a contrast agent is administered that will propagate along the coronaries' path. The result is a movie showing the dye propagating through the coronaries. In lesion sites, coronaries appear to narrow or are blocked completely in which case the dye stops spreading. This method of evaluation of coronary lesions might result in complications in rare cases, such as the puncture of vessels or adjacent organs or difficulties at the puncture site where the guide wire is first introduced where hematoma could develop.

Different imaging modalities allow visualization of a patient's function or anatomy and might be used in CAD in the presence of CHD. Anatomic (or structural) information is available with Computer Tomography Angiography (CTA). A contrast agent is administered through the arm and spreads until it reaches the coronaries. A CT scan is performed at that moment and coronaries appear bright on the resulting images. The surfaces of the myocardium (epicardium and endocardium) are identifiable as well and coronary anatomy of individual patients can be determined by experienced physicians. This modality is however deprived of any functional information and the effect of the disease on the cardiac muscle cannot be studied. Myocardial function, and therefore identification of damaged tissues, is possible with nuclear studies (PET, SPECT), that enhance sites of damaged tissues, as well as delayed enhancement magnetic resonance (DEMR), that enhances dead tissues. The advantage of DEMR over the previous modalities is the non exposure to ionizing radiation. In DEMR, the persistence of a contrast agent in the myocardial cells allows for the identification of myocardium

corresponding to dead tissues since the agent remains longer in dead cells (hypothesized to be due to the slow washout of agent by myocardial cells). The location of dead tissues on images is therefore possible by identifying brighter regions in the myocardium in DEMR images. This modality therefore offers viability information and has proven reliable in highlighting the extent of infarcted myocardium [4].

Intervention for revascularization in the presence of CHD benefits from knowledge of a patients' myocardial viability. In standard clinical practice, patients do not typically receive both a CTA and a DEMR (or nuclear study). Rather, the clinician relies on an MR study, followed but a coronary angiogram. The MR or nuclear images allow locating damaged or dead areas over the myocardium. He then refers to a population based model (such as the 17-segment model) that guides him to the highest probable stenosed coronary responsible for the lesion (this could be scar or ischemia). Structural damage to the coronaries may be inferred from CT angiograms. The clinician is interested in locating the coronary arteries including sites of plaque accumulation inside a coronary and that alters blood flow. This procedure involves a catheter insertion, which might imply a possible risk for the patient. Moreover, the individual patient's coronary anatomy might deviate from the standard models and lead to misinterpretation of the patient's state. Furthermore, the 17-segment model includes the main coronary arteries but not the location of specific diagonal branches.

We aim to fuse both function and structural information to aid in the clinical procedure. The goal of this thesis is therefore to provide a means to determine, in a patient-specific manner, if a patient will benefit from an intervention, such as a revascularization by stent or bypass, and moreover might save a patient from undergoing a catheterization in the case where non-viable (dead) tissue is identified. We make the case that fusing CTA and DEMR (or nuclear) will allow us to answer the question: which coronaries feed which

regions and will those regions benefit from intervention? DEMR is chosen for this study since it does not involve exposure of the patient to ionizing agents and since it has proven reliable for viability studies [4]. Thus we endeavor to create patient-specific 2D viability maps, similar to the 17-segment model and that would allow the physician to visualize the association of regions of myocardium that are found to contain non-viable (dead) or damaged tissue with a particular coronary artery. This involves registration of both structural and functional images from CTA and DEMR respectively. Those modalities have the advantage of being considered non invasive (as opposed to catheterization) and their fusion allows synergistic interpretation of available information.

The second chapter of this thesis describes the anatomy of a healthy heart, as well as CHD and its impact on the heart's organs. Therapeutic interventions as well as modalities used are presented as well. In Chapter 3, methods used to create viability maps are listed and the results obtained are shown in Chapter 4. Finally Chapter 5 concludes the work done for this thesis and enumerates possible future work.

CHAPITRE 1 LITTERATURE SURVEY

Myocardial viability and stenosis location (position of obstruction in coronaries) are crucial information to the physician in order to attempt a prognosis of an intervention in the presence of coronary artery disease. To properly describe this pathology, the anatomy and function of the healthy heart will first be presented, followed by a description of the different physiological alterations induced by CHD. A study of currently used modalities and a review of existing methods of registration and of coronary territory estimation will also be presented.

1.1 Anatomy, physiology and function of the healthy heart

The chambers

The heart is located in the thorax, in a sac known as the pericardium between the lungs and composed of four chambers: the right and left atria and the right and left ventricles (Figure 1.1). The interventricular septum (Figure 1.1) delineates the compartments of the left and right ventricles [5]. Valves ensure the correct blood flow direction between the different chambers of the heart and the cavities connected to them. The right atrium and the right ventricle are separated by the right atrioventricular valve, also known as the tricuspid valve. In the same way the left atrium and left ventricle are separated by the mitral valve. The pulmonary valve separates the right ventricle from the pulmonary artery. The aortic valve separates the LV from the aorta.

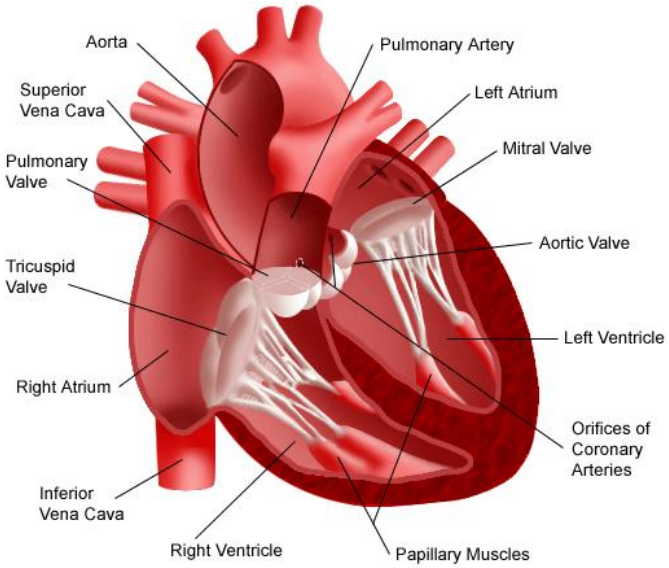

(a)

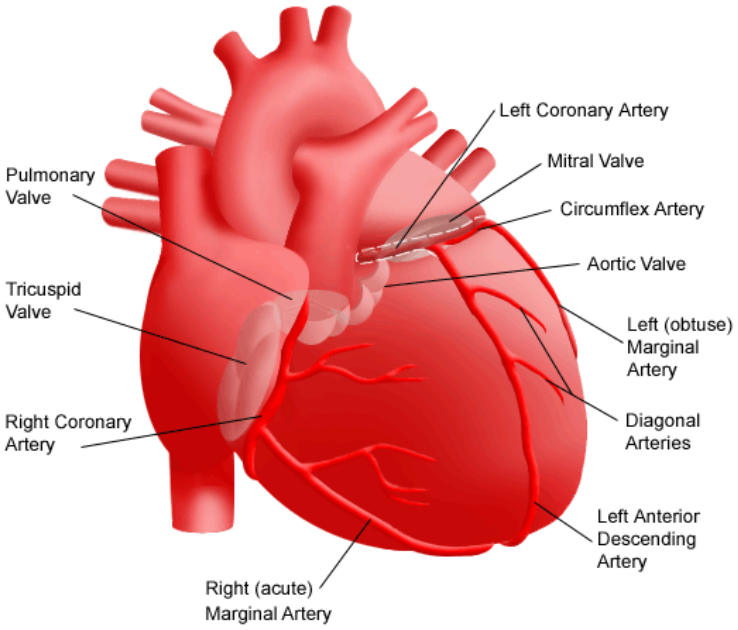

(b)

Figure 1.1: Heart Anatomy: four chambers, valves (a) and veins, arteries, vena cava (b) [6].

The heart wall

The myocardium is the middle layer of the cardiac muscle and contains myocytes. It surrounds the heart completely and is thickest around the ventricles and thinnest around the atria [32]. The endocardium is the inner lining of the heart wall, composed of endothelial cells (thin, flat cells that lie on internal cavities of the body [24]), and spreads through all cavities, atria and ventricles. These endothelial cells cover a section of subendothelial connective tissue, separated from the myocardium by a subendocardial layer of blood vessels, nerves and possibly branches of the Purkinje fibers (part of the electrical system that activates the heart's contraction). The epicardium is a layer of mesothelial cells located on the outer surface of the heart and covering a layer of connective tissue that separates it from the myocardium.

Contractile cells

Myocytes are the contractile cells of the heart, containing actin and myosin (contractions are possible because of the interaction between these two substances). They are short in length and are branching at their tips, creating a complex structure. Contractions propagate from cell to cell by means of gap junctions present in the intercalated disks that separate cells from their neighboring cells [19]. This structure is built in such a way that excitation propagates faster in a direction parallel to the long axis of the heart, which is the imaginary axis that traverses the left ventricle from apex (tip) to base (a region determined by the position of the center of the mitral valve) [34].

Heart Orientation

The American Heart Association (AHA) has proposed a standard concerning the orientation of the heart while under observation in order to have a stable reference frame [34]. This is particularly useful in medical imaging to present images of the heart to

clinicians. Two views are possible along the long axis: horizontal and vertical. In the first, it is possible to view the right and left ventricles, as seen in Figure 1.2 (b), whereas the right ventricle is not visible in the vertical long axis view, as shown in Figure 1.2 (a). The short axis view presents the heart as if it is sliced perpendicular to the long axis. Both the right and left ventricles are visible, as shown schematically in Figure 1.3.

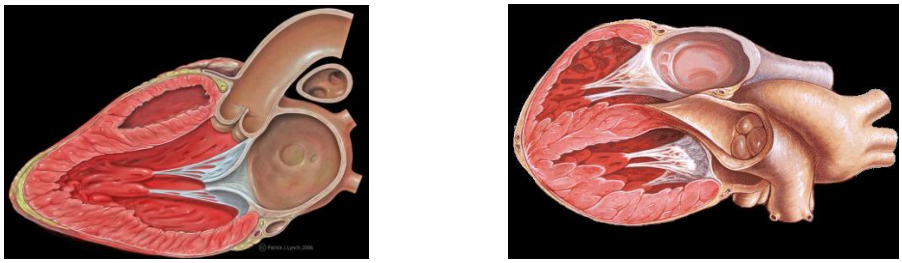

(a) (b)

Figure 1.2: vertical (a) and horizontal (b) long axis view of the heart [35].

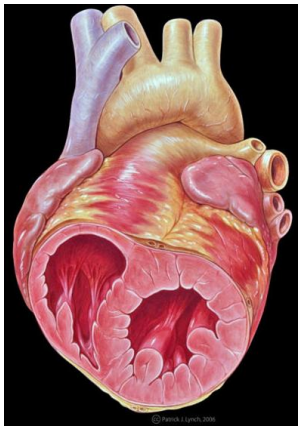

Figure 1.3 : View of the heart in the short axis plane [35].

The coronaries

Blood circulation in the cardiac muscle is ensured by the coronary arteries (see Figure 1.1, b), which bring blood to the muscle, and by the veins, into which blood flows away

from the myocardium. Coronaries emerge from the aorta and spread over the myocardium, even penetrating into it to supply the inner tissues. The right coronary artery (RCA) originates from the right aortic sinus; and from the left aortic sinus arises the left coronary artery (LCA, also called anterior interventricular artery) [8]. Branching off from the LCA is a major artery known as the left anterior descending (LAD) as well as the left circumflex (LCX). The term posterior descending artery (PDA) designates the artery supplying the diaphragmatic surface of the heart. The coronary supplying this region determines coronary tree dominance (see Figure 1.4), which is not to be confused with irrigating dominance which is always left. Left dominance is defined as having the LCX supply the PDA, and right dominance the RCA feeding the PDA. There are also known cases of non dominance in individuals, occurring when both right and left coronary arteries supply the posterior part of the interventricular septum with blood. Individual variability in terms of coronary dominance in the population is still under investigation in humans [8], [11], [12], [13], and has also been observed in cases of animal experimentation [25], [26]. The extent to which coronary length is related to coronary dominance is also currently under study [9].

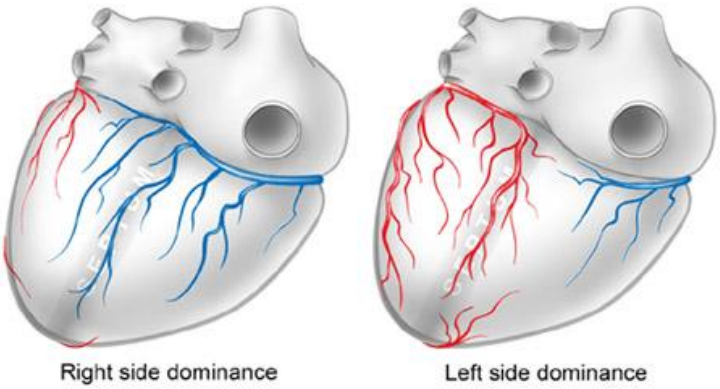

Figure 1.4: Coronary tree: right (a) and left (b) dominance [10].

Circulatory system

The human blood circulatory system can be divided in two sections: pulmonary and systemic [5]. The first describes the blood circulation from the heart to the lungs and back. In this system, the right ventricle (RV) ejects deoxygenated blood through the pulmonary valve and into the pulmonary artery. Blood then flows through the arteries, enters the lungs by the capillary vessels where it is oxygenated, and leaves the lungs into the pulmonary veins which guide it back to the left atrium of the heart. Blood then flows from the left atrium into the left ventricle (LV) through the mitral valve. Systemic circulation describes the blood flow from the heart towards the rest of the body and back. It may be though of starting when blood is ejected from the LV through the aortic valve and into the aorta. The blood flows through the aorta to the arteries and it then successively flows through the arterioles and capillaries where exchange is favorable between oxygenated blood and the cells of the body. The blood then exits through the veins and into the inferior or superior vena cava, which guides it back to the heart, into the right atrium.

Cardiac cycle

The circulatory system is maintained by successive relaxations (diastole) and contractions (systole) of the heart. This cycle is controlled by electrical activity initiated by the sinoatrial node (SA), which can be considered as the pacemaker of the heart. It is located inside the right atrium (RA), and induces a chain of depolarization that propagates through the heart [19]. The contraction signal propagates from the right to the left atrium by muscular cells and from the atrium to the ventricles by the atrioventricular (AV) node. The signal then reaches the bundle of His that separates into the right and left bundle. These conduct the signal from the base of the myocardium to the Purkinje fibers, subendocardial conducting fibers that have a rapid activation which synchronizes the right and left ventricle contractions. At a cellular level, excitation happens with

depolarization of a cell membrane. Normally, intracellular potential is about -90mV less than the surrounding potential. After depolarization, it rises to +20mV and lowers suddenly until it reaches a plateau for a fixed period of time. Repolarization happens slowly after the plateau when the potential reaches its initial level. Muscle contraction occurs after an abrupt polarization and continues even a moment after repolarization. The action potential in the heart can be fast, such as with fibers of the atrium or the ventricles, or slow, for fibers of the SA node or the AV node [19].

Electrocardiogram (ECG)

The electrocardiogram reflects the signal propagation through the conducting system of the heart. As illustrated in Figure 1.5, the spread of excitation that starts the atrial systole is known as the P wave. At that point the tricuspid and mitral valves are open and blood is ejected from the atria to the ventricles. The spread of excitation in the ventricles corresponds to the QRS wave. Once the ventricles are filled the atrial valves close and ventricular systole begins, this corresponds to the Q peak. The left ventricle ejects blood into the aorta during contractions that last until the ventricular repolarization, thus corresponding to the T wave. There is a delay between the end of atrial contraction and the start of ventricular contraction (P-R interval), allowing the maximum amount of blood to flow from atrium to ventricle, filling the ventricles prior to their contraction. This delay is due to propagation of the signal inside the AV node. The interval between Q and T signal is referred to as the “electrical systole” [19]. There is minimal movement of the heart at end of systole. The heart’s contractions vary in rate and force with respect to the metabolic demand. When coronary blood flow is increased, oxygen supply also increases, as well as washout of CO2 and metabolites. The reverse mechanism applies when blood flow is diminished.

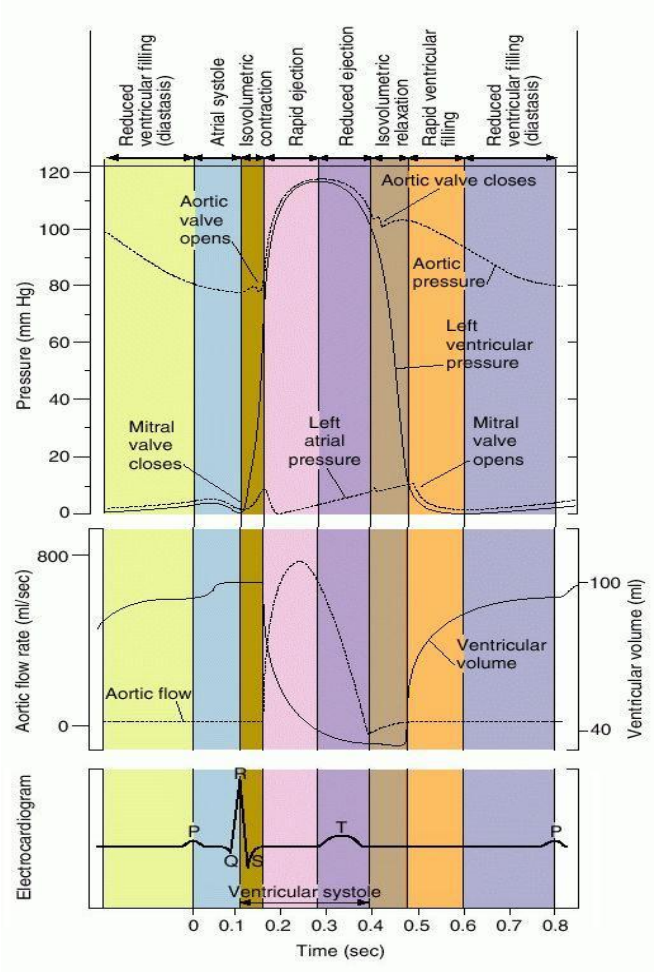

Figure 1.5: Cardiac cycle and electrocardiogram (ECG) [20].

1.2 Coronary Artery Disease

Atherosclerosis

CHD alters the shape and composition of coronaries, has a direct impact over myocardial perfusion and, depending on the severity of the disease affects contractions in the cardiac cycle. This ultimately threatens the life of the patient if blood can no longer be adequately propelled from the heart to the rest of the body. The exact causes of this disease are still

unclear but risk factors have been identified by the American Heart Association (AHA) [21]. Age, gender or heredity as well as smoking habits, high blood pressure related to cholesterol, a sedentary lifestyle, obesity and diabetes are all risk factors for CHD. Stress and alcoholism are also identified as an influence in the appearance of the disease for some individuals.

A healthy coronary is a tubular structure having an inner lining called intima composed of smooth muscle cells, a thicker layer called media containing muscle cells and an outer layer called adventitia. CHD may result in stenosis of coronary arteries which obstructs blood flow to the cardiac muscle (see Figure 1.6) and deprives it of its oxygenated blood, leading to different degrees of hibernating, stunning or scarring of the cardiac muscle. This blockage phenomenon is known as atherosclerosis and is classified as lesion types I to VI. This classification establishes the degree of the disease based on the different morphological characteristics observable in different lesions [27].

The first three types of atheroscleroses are generally not life threatening and are interesting to clinicians only as precursors of further complications [27]. All types of lesions are represented schematically in (Figure 1.7). The first type (I) consists of small deposits of lipids inside the intima layer, of microscopic dimensions, present mostly in infants and children and less frequently in adults. Type II lesions are often visible to the human eye and are seen as streaks or spots on the intima of coronaries. In type III lesions, extracellular lipid droplets are microscopically visible and group into regions inside the intima, between smooth muscle cells. This type is referred to as the preatheroma stage, before a more severe type IV.

The advanced stages (types IV to VI) are characterized by thickening and structural disorganization of the intima layer caused by accumulation of lipids, cells and matrix components that may lead to a deformation of the coronary, eventually leading to blockage by fissure, hematoma or thrombosis [28]. In the occurrence of these lesions there may be modification to the media and adventitia as well. Type IV lesions are called atheroma and are characterized by the presence of a lipid core (a dense extracellular lipid accumulation and possibly accumulation of calcium) creating a severe disorganization of the intima (displacement of smooth muscle cells and intercellular matrix). Although there may be thickening of the intima, there is not necessarily reduction of the lumen diameter since it has been observed that the outer layer of media and adventitia may extend. This type of lesion may lead to fissures, transforming to types VI lesions. Type V lesions are identified by an increase of new connective fibrous tissue observed in the intima region. It is characterized by a narrowing of the lumen and the possible appearance of fissures, hematoma or thrombus, leading to a complicated lesion (type VI). The last two types are related to the majority of the complications of atherosclerosis.

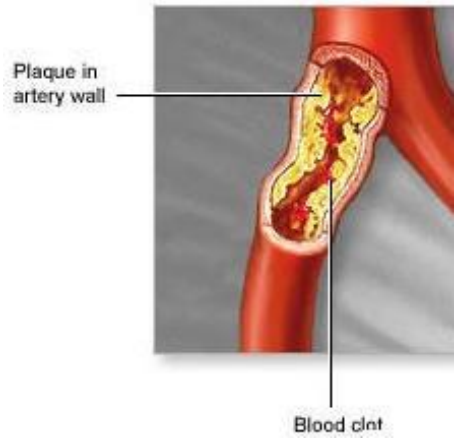

Figure 1.6: Atherosclerosis: accumulation of plaque inside a coronary [29].

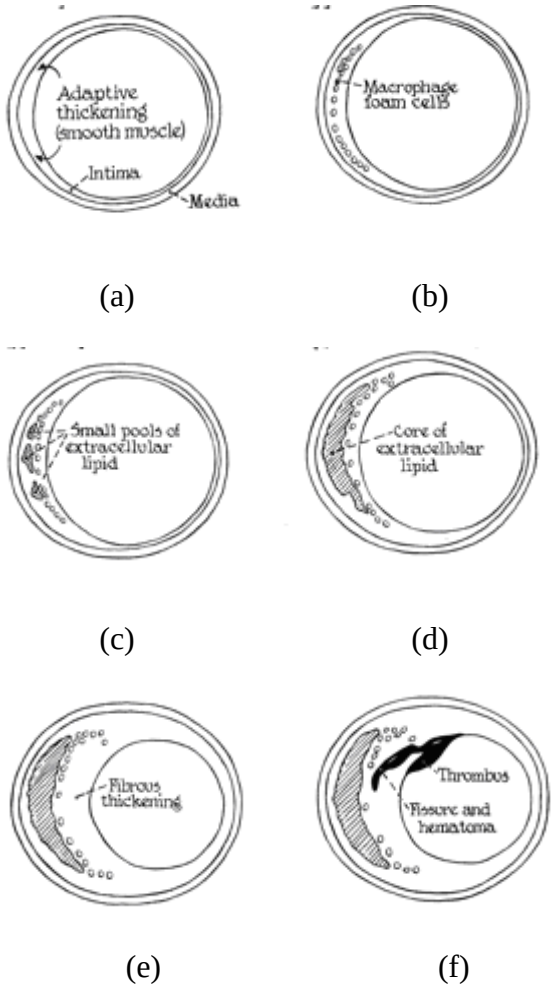

Figure 1.7 Atherosclerosis: schematic view of lesions types [27]. Coronary artery at lesion-prone location (a), type II lesion (b), type III or preatheroma (c), type IV or atheroma (d), type V or fibroatheroma (e) and type VI or complicated lesion (f).

Myocardial lesions

With CHD appears myocardial ischemia (deficiency of blood flow to the cardiac muscle) and eventually chest pain (angina pectoris), which is a symptom of heart attack. The diminished blood supply to the myocardium leads to an inbalance of K+ concentration

around the cell and transforms the action potential of ventricular cells from a fast to a slow response [19]. The worst outcome of this state is myocardial necrosis (death of contractile cells). If the period of ischemia is limited (in time and severity) the myocardium may remain viable and its cells could possibly recover. Myocardial stunning refers to a state into which the myocardium remains dysfunctional after a severe period of ischemia but may recover after a period (of days or weeks). Hibernating myocardium is described as a state of reduced contractile function of the cardiac muscle in response to myocardial ischemia [42], it is as though the cardiac muscle cells diminished their activity in order to minimize their energy consumption and survive upon a reduced supply of blood. Hibernating myocardium will fully recover after intervention. It is not clear what precedent state leads to hibernation: repetitive stunning or direct adaptation of the cardiac muscle cells to reduced blood flow [43]. Myocardial necrosis consists of appearance of scar (dead tissues) and is irreversible. As myocardial cells are affected by coronary occlusion, their polarization and depolarization are altered, leading to a variation of myocardial contractile function and with more impact upon stress or exercise when the output of blood needs to be increased.

1.3 Medical imaging in CHD

Medical imaging modalities render an internal picture of organs and allow analyzing structural as well as functional information of the patient. During a typical CHD diagnosis, the patient first undergoes a perfusion study that informs the clinician on the location and severity of ischemia. This allows him to evaluate chances of recovery and to decide if a patient is unfit for intervention, a possibility if necrosis is irreversible. Location of stenosis is established later on with a structural imaging modality. Any imaging modality presents a challenge in cardiology because the heart is in motion.

CT/MDCT

Computer tomography (CT) image formation results from the partial absorption of x-rays by the body and gives structural information on organs. Gamma rays bombard the body and are captured by receptor screens when they exit the patient after molecular interaction. Rays enter the body with a specific trajectory and energy potential which both vary after interaction with body tissues (depending on the absorption coefficient of the tissues). This explains the various shades of grey for different tissues in resulting images. This technology generally gives precise images and is favored for the study of structural information (organ morphology) at the price of exposure to a radioactive source. Employing this modality is justified by the severity of the illness and the risk of death of the patient. Multi detector computer tomography (MDCT) is accomplished by rotation of a series of x-ray emitters and receptors placed on opposite side of the body. The final image is created by computers following a reconstruction algorithm.

Computer Tomography Angiography

Computer tomography angiography (CTA) consists of a CT scan performed at a specific time after administration of a contrast agent that spreads through the coronaries of the heart. It is a single time point 3D image that allows visualization of the lumen of coronaries. Contrary to coronary angiography, there is no catheter inserted into the body, rather the contrast agent is inserted through a peripheral vessel and spreads through the circulatory system. The CT scan is then performed at the exact time the contrast agent has reached the coronaries, called peak contrast enhancement. A protocol should be followed for contrast injection and image acquisition to determine time, duration and to quantify variation of enhancement in coronaries. Circulation (influenced by the patient's physical condition such as weight) and the duration of injection of contrast agent are the main factor in determining time and duration of acquisition [61].

Angiography/Fluoroscopy

Angiography is a term that defines a technology that allows visualization of blood vessels after a contrast agent has been administered. It may target many areas of the body. In cardiology, coronary angiography allows visualization of the lumen of coronaries and is performed in order to establish the severity and location of stenosis. A guide wire is first introduced in the body through an incision (made in the groin area or underarm) and guided to the coronary arteries via the aorta. A catheter is then inserted and releases a contrast agent where the major coronaries originate. The dye spreads in the coronaries which appear brighter in images [39]. This allows identification of stenosis as the coronaries appear to narrow in those specific locations. A schematic representation of the procedure is given in Figure 1.8. With a fluorescent screen placed opposite the radioactive source and a recording device, a movie can be created where the clinician can see the contrast agent spread progressively in the coronaries. This imaging modality is termed fluoroscopy.

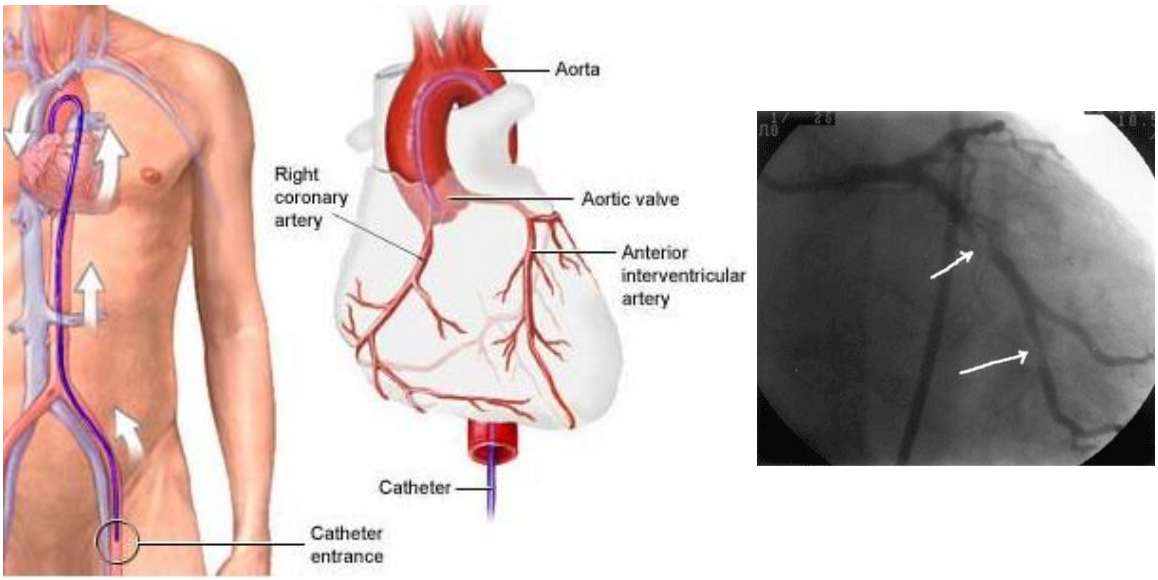

Figure 1.8 : Schematic representation of coronary angiography [40], [41].

SPECT

Single photon emission computer tomography (SPECT) consists of capturing gamma rays emitted by a radioactive agent administered to the patient and absorbed by targeted organs, each decay liberates only one photon. In CT the radioactive source is located outside the patient, whereas in SPECT it is inside the body. As the radioactive agents decay over time and liberate gamma rays, a camera captures them during a patient's scan. Images obtained from this modality are of low resolution due to heart motion and sparsity of signal and thus little structural information is available. Moreover the location of the camera influences image formation: when it is placed in the front or back of the patient, liberated rays traverse less body tissue (in particular bone) than when it is placed to the side of the patient (right or left). This situation is resolved using a correction algorithm which finds an attenuation coefficient for the signal [62], based on structural information from, for example, a CT scan [63], [64]. These attenuation maps have been used to correct the interpretation of nuclear of images [67], [68],], [69], [70]. SPECT is clinically used in many different medical contexts to visualize function of organs such as the lungs [65], brain [66] etc. In cardiology, a radioactive agent is absorbed by the cardiac muscle and SPECT depicts the absorption rate of the agent by the cells. Cells affected by ischemia have a slower absorption rate than healthy ones and therefore appear darker on resulting images. Bright areas indicate healthy tissues of the myocardium. A first acquisition is done at rest and a following one under stress in order to visualize perfusion as the cardiac muscle's work increases. A difference between healthy and affected cells is more easily perceived comparing both sets of images. Regions showing no perfusion deficit at rest may present it during the stress scan. This modality has proven reliable to study the ischemic heart's perfusion [71].

Positron Emission Tomography

Positron emission tomography (PET), like SPECT, requires the use of an emissive tracer, with the difference that PET uses a positron emissive substance that will liberate a pair of gamma rays upon interaction with electrons of collateral tissues. Since there are two rays coming from one location with different angles, the three dimensional information concerning the location of the emission is precise and PET therefore offers better resolution than SPECT images. PET is used in cardiology most commonly to image myocardial perfusion [72], [73], [74] but is applied to coronary plaque localization as well, although this method is still in preliminary study [75], [76]. FDG-PET (Fluorine(18) 2-fluoro-2-deoxy-D-glucose) is considered the "gold standard" for viability because of it's correlation with improvement of LV function following revascularization.

MR/DEMR/CineMR

Magnetic resonance is a promising technology since it can be used to effectively establish myocardial viability [85],

[86], .

[88], [89], , viii.

[90] within a structural context but moreover because of the absence of exposure to radioactive agents [91]. In the presence of CHD, DEMR best pictures non-viable regions of the LV but, unfortunately, cannot simultaneously render coronaries.

Magnetic resonance imaging is built on the principal of molecular response to magnetic excitation. Any nuclei formed of an odd number of neutrons and protons has the property of spin, which is regarded as a rotation around the polarization axis [96]. Hydrogen is a

molecule that has this property and is found in water and fat, the two main components of the body.

In a normal environment, the magnetic fields of the nuclei are randomly oriented and therefore their magnetic moments cancel (see Figure 1.9 a). When an initial constant magnetic field (B_0) is applied, alignment of the spin axis of the nuclei takes place with a specific orientation somewhere close to the polarization axis, parallel to B_0 (see Figure 1.9 b). The orientation of the spin is not exactly parallel to the B_0 direction and precesses at a certain angle around B_0 (see Figure 1.10) with a frequency described by the Larmor equation, with γ as the gyromagnetic constant and F as the frequency:

$$\gamma * B_0 = F.$$

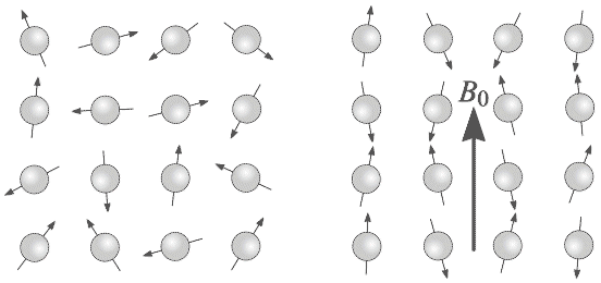

(a) (b)

Figure 1.9 : Orientation of nuclei in a normal environment (a) and in the presence of an external magnetic field B_0 (b) [97].

The spin axis of molecules can be represented by a vector described by two components: either parallel or perpendicular to B_0. The sum of all components perpendicular to B_0 cancel and only a small magnetic moment is left (named net magnetization and noted M) whose direction is parallel and related to the strength of B_0 (see Figure 1.10 a).

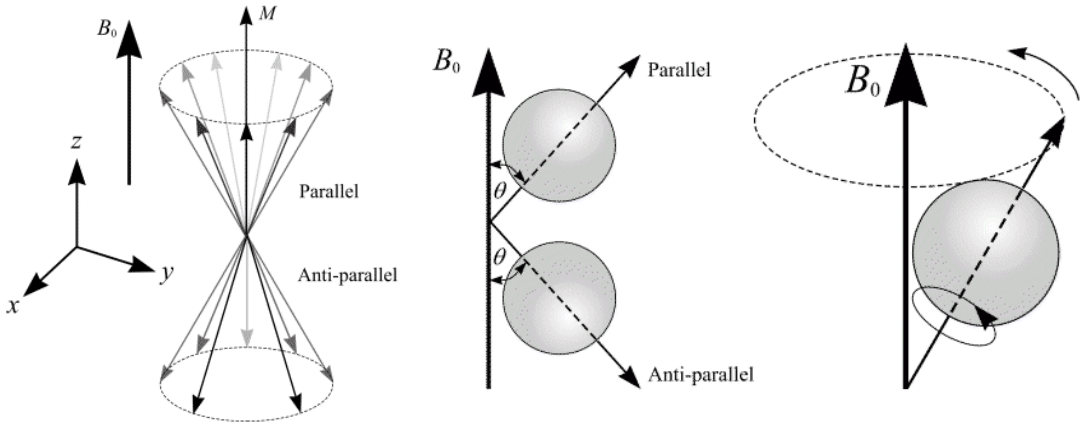

(a) (b) (c)

Figure 1.10: Magnetization in the presence of a constant magnetic field (a), with parallel or anti-parallel direction (b), and orientation of the spin direction (c) [97].

In the presence of B_0, hydrogen molecules are found in two different states: low and high energy. In the low energy state, into which fall most of the nuclei, the spin has an orientation close to that of the magnetic field orientation (termed parallel in Figure 1.10) whereas in a high energy state the orientation of the spin will be at an angle close to the opposite direction of B_0 (named anti-parallel in Figure 1.10). Protons can change energy state (low to high and vice versa) only if they acquire or release the exact amount of energy that differentiates both states, which happens with the absorption or release of a photon. The higher B_0, the higher energy it takes to change the orientation of hydrogen molecules (see Figure 1.11).

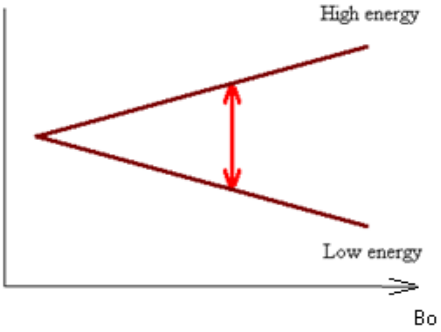

Figure 1.11: Difference in energy level of nucleus with application of an external magnetic field B0.

In order to make a nucleus change energy state, a radio frequency pulse is applied (RF signal) at the Larmor Frequency. Applying an RF signal results in a tilt of the net magnetization *M* proportional to the strength and duration of the signal applied. Such as indicated in Figure 1.10 (a), let us use a coordinate axis whose *z* direction is aligned with the direction of B_0. The tilt is known as a flip angle from the *z*-axis and *M* now has an *x*-*y* component. Applying a 90^o (or 270^o) signal results in the net magnetization being stripped of any z components and therefore lying completely in the perpendicular plane to B_0. Once the RF signal is removed the tilted *M* oscillates around the *z*-axis until it returns to its equilibrium, the B_0 direction (see Figure 1.12 b), creating an electromotive force that is detected by an RF coil. The return to equilibrium is called the relaxation process. This detected signal is the basis of MR image formation, the capture of the signal generated upon liberation of the previously absorbed energy.

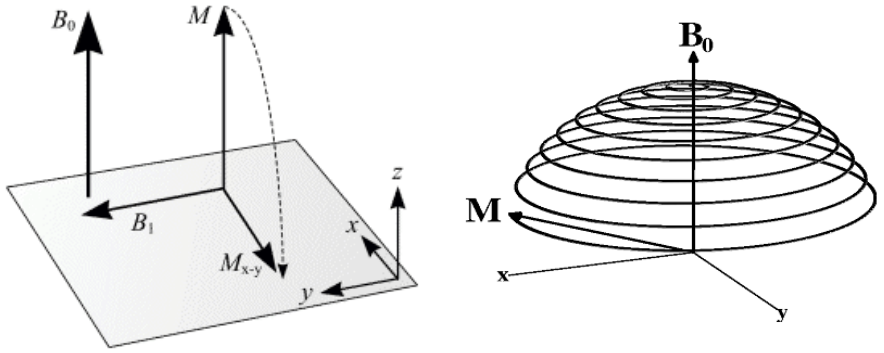

(a) (b)

Figure 1.12: Components of the net magnetization *M* after applying an RF signal of 90^0 and the oscillatory effect on the vector after its removal [97].

In the absence of any other magnetic gradients, the captured signal has the form presented in Figure 1.13 and is termed Free Induction Decay (FID). The amplitude of the signal depends on the sine of the flip angle of *M*, the *x-y* component (transverse) of the vector which is maximal after a 90^0 or 270^0 RF signal, and is determined by the number of nuclei that changed energy states as well as by the relaxation time. The amount of time *M* takes to realign with B_0 is called spin-lattice relaxation time and is guided by a *T1* constant. It describes the longitudinal return to equilibrium (recovery). The magnitude of the captured signal following a 90^0 RF pulse is guided by the formula: $M_{long}(1 - e^{-t/T1})$ and *T1* corresponds to the amount of time needed for *M* to restore about 63% of the longitudinal magnetization. The signal envelope of Figure 1.13 is guided by *T2* which is the time constant that weights the rate of decay: the decrease of the *x-y* component of *M*. *T2* is also named transverse relaxation or spin-spin relaxation and it corresponds to the amount of time to diminish the transverse magnetization of about 37%. The magnitude of *M* following a 90^0 RF pulse is guided by the formula: $M_{trans} * e^{-t/T2^*}$ where α is the flip angle, *t* is time. *T2** value is used rather than *T2*

since the magnetic field inhomogeneity causes the actual decay time to be smaller than *T2*.

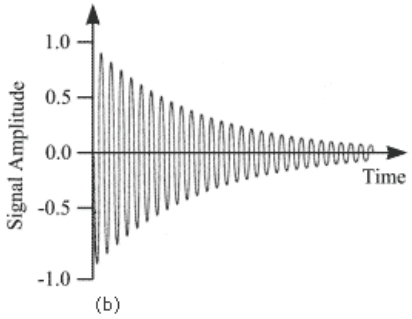

Figure 1.13: Free induction decay, the signal captured upon return of the net magnetization *M* towards a B_0 direction after removal of an RF signal [97].

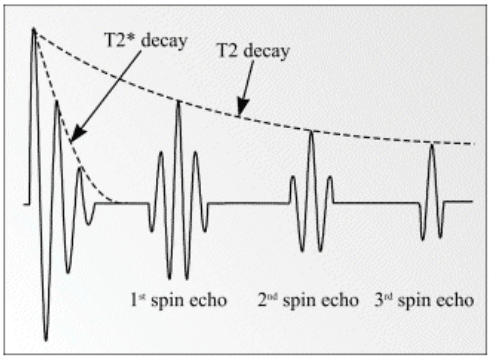

(a)

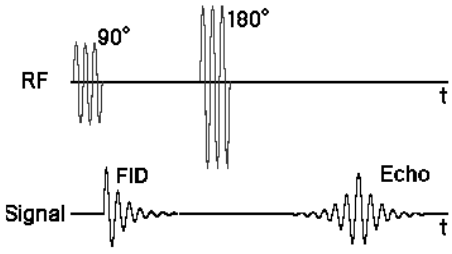

(b)

Figure 1.14: Captured signal after a spin-echo sequence [97].

A sequence of pulses is used in order to obtain a signal closer to *T2* by reducing magnetization inhomogeneity. After a 90^0 pulse has been applied, another pulse is applied of 180^0 that will cause a rephrasing of the spins and a signal known as spin-echo to be released (see Figure 1.14 b). The amplitude of the spin-echo signal is initially related to *T2*, and not *T2** (see Figure 1.14 a). By applying a gradient magnetic field, the magnetic field will vary in function of the position and with it the Larmor frequency will also vary with the position of the nuclei along the z axis (along the body and in the B_0 direction). To excite nuclei that lie at a certain position, an RF pulse with the corresponding frequency is applied. Therefore, to excite a slice, an RF pulse with a range of frequencies is applied such as sketched in Figure 1.15. The strength of the magnetic field B_0 influences the slice thickness, as the gradient field slope increases, only a small slice will be selected with a certain frequency interval whereas the slice will enlarge if the slope is smaller (see Figure 1.16). Organs molecules react differently to exposure to magnetic resonance, which is why different tissues can be identified in the resulting images.

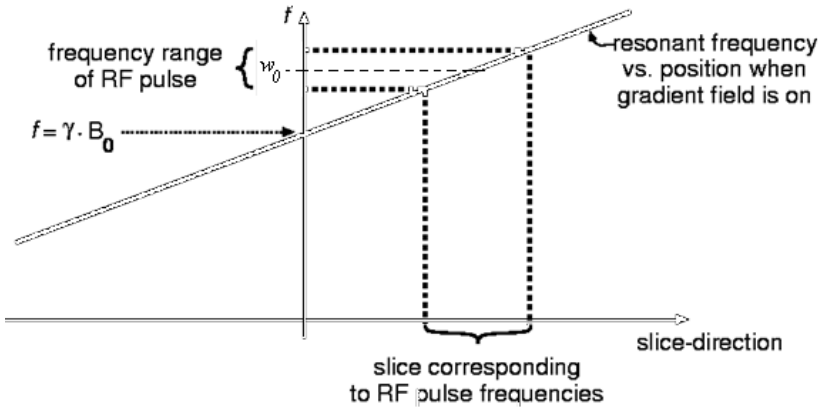

Figure 1.15: Selecting a slice to image with MRI.

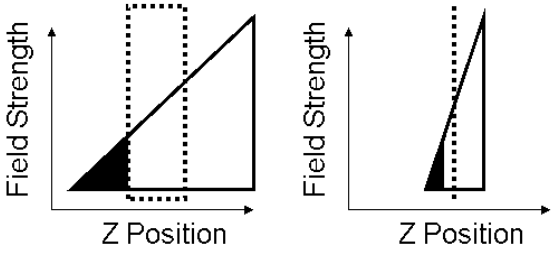

Figure 1.16: Slice thickness with different magnetic field strength.

MR allows study of cardiac function. Since the heart is an organ in constant movement, images are ECG gated. Cinematic magnetic resonance is a sequence of image acquisition that form a movie created with MR technology.

Myocytes affected by CHD have variable wash-in and wash-out rates, a phenomenon visible in MR with the administration of a contrast agent. Delayed Enhancement Magnetic Resonance (DEMR) refers to an acquisition protocol that captures images after a certain delay rather than right after the peak of absorption of contrast agent by the cardiac cells [87]. DEMR therefore depicts washout rate of contrast agent and bright areas indicate the location of non-viable, therefore dead, tissue [88]. It is furthermore possible to study the transmural extent of non-viable myocardium [88] and attempt to predict the probability of improvement of contractility.

1.4 The 17-segment model

During most coronary artery disease diagnoses, a functional exam (for example by nuclear imaging) is first performed to try to identify the presence of damaged myocardium. However, the clinician does not identify lesions in coronary arteries right

away and will only study anatomy later on with a coronary angiography. Under these circumstances, a segment model of the LV may be used after the functional exam, and before the angiographic exam, to infer the most likely obstructed coronary artery responsible for myocardium damage. These models divide the myocardium into different segments and associate each one with a coronary most likely to perfuse it. Different models have been developed: the 16-segment, 17-segment and the 20-segment model [104], [105].

These models take the shape of a bull's eye plot where thick slices of the LV at different long axis levels are projected onto different concentric rings. In the case of the 17-segment model, the heart is divided perpendicularly to the long axis of the heart into three thick slices determined by anatomical landmarks [34]. The outmost ring of the model, the basal slice, represents the thick slice closest to the LV base (mitral valve). The ring adjacent to the basal one, mid-cavity, covers approximately all of the papillary muscles. The apical slice starts where the mid-cavity ends and covers the area until the start of the apex, which is the last anatomical landmark and is projected onto the center of the model. Orientation of the model is determined by the interventricular septum location and should be projected onto the left side of the model (see Figure 1.17). The basal and mid-cavity slices are divided into 6 segments. Referring to Figure 1.18 and to Figure 1.17, segments 1 and 7 are oriented towards the anterior of the LV and segments 4 and 10 towards the inferior region. Segments 2 and 8 as well as 3 and 9 represent area oriented towards the septum (anteroseptal and inferoseptal respectively). Segments 5 and 11 refer to the inferolateral region, and segments 6 and 12 to the anterolateral area.

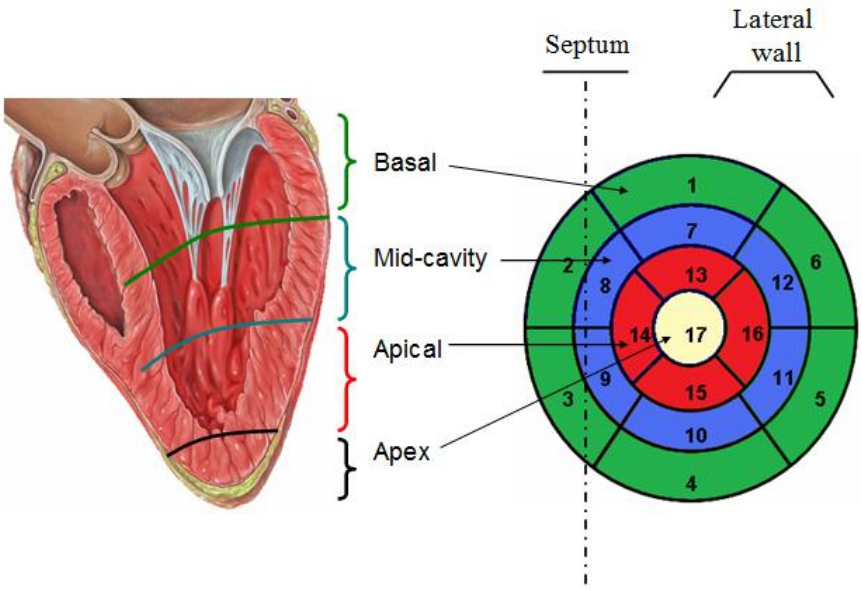

Figure 1.17: The 17-segment model to identify anatomical structures of the heart. The colors of the original model have been modified in order to associate each concentric ring to a specific area of the LV: apex (white), apical (red), mid-cavity (blue) and basal (green).

Each segment is associated with a coronary based on the average distribution of the coronary tree over the myocardium. The blue area presented in Figure 1.18 is associated with the LAD, the brown with the RCA and the green with the LCX. After analysis of the myocardium of a patient who has had a functional imaging exam, the clinician can report the affected area on the model and can deduce the probable coronary artery responsible for myocardium damage by relying on the color code of the model. Any knowledge of the exact location of stenosis will be discovered later during a coronary angiography.

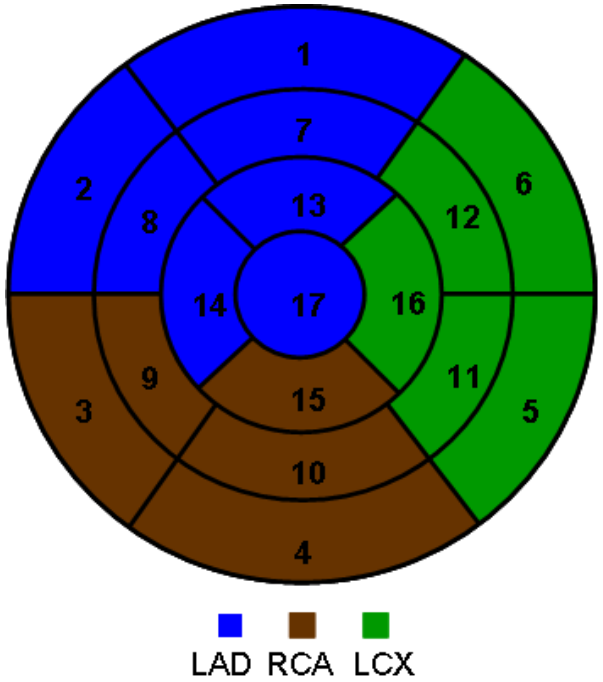

Segments	Region
1, 7, 13	Anterior
2, 8	Anteroseptal
14	Septal
3, 9	Inferoseptal
4, 10, 15	Inferior
5, 11	Inferolateral
6, 12	Anterolateral
16	Lateral

Figure 1.18: The 17-segment model with color coded areas relating to typical coronary distribution, and the legend associating segments of the model to anatomical LV location.

Limitations

It has been shown that the empirical 17-segment model does not account for the possible variation in coronary tree structure in an individual. For instance, one recent study found the 17-segment LV model accurate on average after examining the correspondence between coronary anatomy and regions of myocardium in 135 patients using monoplane coronary angiography [37]. However, 27 patients (20%) showed discordance between the model and the patient's anatomy in more than 4 segments. In 13 patients (10%) there was discordance in more than 5 segments. Moreover, 8 of these patients had left dominant coronary distributions while the model assumes right dominance. The study did not address clinical impact of interpretation errors. Another study compared co-registration

of MRI and multi-slice computer tomography (MSCT) images used to assess the correspondence of individual patient's coronary anatomy (in 26 patients) to a 17-segment coronary distribution model [38]. At least 1 segment was discordant in 22 patients (85%). Overall, 17% (76/442) of myocardial segments differed from their assignment by the 17-segment model. Another study by Partridge and Anderson recently underlined incorrect anatomical representation of the heart in the 17-segment model and requested adaptation or development of a new model [55].

Creation of a patient-specific 17-segment model is desirable to account for the possible variation of coronary tree structure in an individual. This would allow more accurate correspondence of altered function with diseased coronary. Moreover, presentation of fused functional images with structural images required to create such a model would simplify the physician's task at mentally integrating information from various sources.

1.5 Interventions in presence of CHD

Intervention in the presence of CHD aims to reestablish blood flow to the cardiac muscle and allow the heart to regain normal activity, if possible. Many types of interventions exist, all of them involving a risk for the life of the patient. The physician performs the revascularization method he judges appropriate based on the diagnosis.

Coronary artery bypass graft (CABG)

The coronary artery bypass graft (CABG) procedure accomplishes myocardial reperfusion through bypassing a lesion by a detoured path (a grafted artery that will be sewn below the blockage). On-pump surgery (ONCAB) uses a cardiopulmonary bypass (heart-lung pump) to allow blood to circulate in the body while the heart is immobilized.

Off-pump intervention (OPCAB) is also possible with the use of immobilizing devices that affect only sections of the heart and allow for the rest of the heart to beat and propel blood during surgery. Originally, OPCAB surgery was introduced after there were doubts concerning negative effects on the patients with the on-pomp procedure such as loss of memory, concentration problems and unclear thoughts [50]. OPCAB surgery can only be done on selected patients based on the state of the patient's arterial system. Several studies compared both types of interventions, and in general OPCAB seems to generate higher risk of occlusion or incomplete revascularization. Although compared to ONCAB it lowers mortality rate as well as lower the need for blood transfusion, lower the negative neurological impacts that were seen with ONCAB and lessen complications for patient that have problem with their renal system [49].

The graft vein generally comes from the patient (Figure 1.19) [52]. The internal mammary artery (the artery that supplies the anterior thoracic region, the intercostal region as well as the mammary glands and the diaphragm [48]) can be used to this end [53]. The connection to the aorta is left intact. The other end is cut from the anterior thoracic region to be oriented towards the blocked coronary and grafted onto it, distal to the stenosis. Grafts that use this artery tend to offer high chances of fast recovery and longer lasting revascularization with low chances of needing interventions in the following years. The gastro-epiploic artery can also be used for grafts. Because it is more difficult to accomplish, it is only used in particular situations, as decided by the physician. Radial artery grafts are easier to accomplish but less common because of known cases of reocclusion and unknown long term effects. Overall, CABG is still a procedure with high risk for the patient and a precise diagnostic could lead the physician in deciding whether or not to attempt this type of intervention.

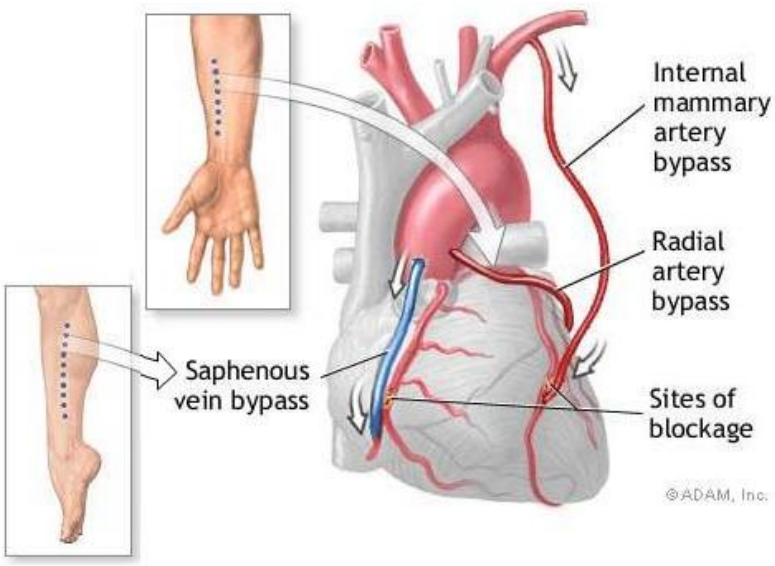

Figure 1.19: Coronary artery bypass graft: saphenous vein, radial artery and internal mammary artery bypass example [51].

Coronary catheterization

Catheterization is performed by first inserting a guide wire into the patient, generally into a vein in the groin area. The wire is moved along the aorta until it reaches the heart. Once it is in place, instruments are introduced in the patient by following the guide wire (Figure 1.20).

The first human heart catheterization was most probably performed by researchers Bleichroder, Unger and Loeb [44] in 1905, but was officially attributed to Forssmann in 1956 when he was given a Nobel prize for his self catheterization work published in 1929 [44]. A catheter with a balloon placed at its tip was first created by Dotter in 1951 [44]. He created the device to cause an occlusion of the pulmonary artery for his studies. Seldinger first used a guide wire to place catheters and Sones is known for his accidental

right coronary catheterization in 1958, after which he developed specific coronary angiography [44] which consists in introducing a contrast agent in the coronaries to better visualize them in resulting acquired images. In 1978, Rentrop et al. published a study showing that coronary thrombi could be removed with guide wires to treat patients with myocardial ischemia [44]. The first human balloon angioplasty was performed by Gruentzig and Myler in 1977 [44].

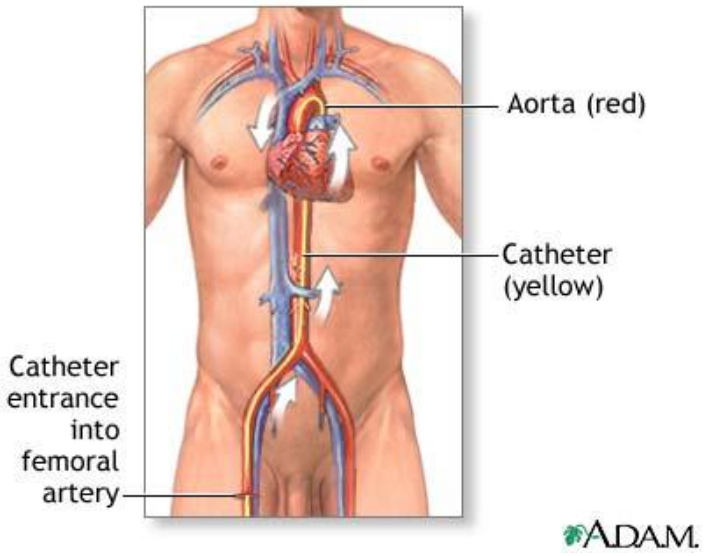

Figure 1.20: Cardiac catheterization [45].

Balloon angioplasty

Following the identification of a lesion location by angiography, the physician can choose to unclog the artery by using balloon angioplasty, also called percutaneous transluminal coronary angioplasty (PTCA) or balloon dilation. An inflatable balloon is placed at the tip of a catheter and inflated to compress coronary plaque and reestablish blood flow (Figure 1.21a). This treatment is possible during angiography and is commonly followed by placement of a stent to keep the coronaries open.

Stents, Bare metal stents (BMS) and Drug eluding stents (DES)

Stents are metallic meshes that are permanently placed inside the coronary and serve as a scaffold structure to hold the coronary open (Figure 1.21b). The first coronary stent placed in a human was stainless steel and was accomplished by Sigwart et al. in 1987 [44]. Stents were then placed over the balloon in catheters, expanded and fixed to the coronary following balloon inflation [44]. However, proliferation of tissues over the stents may lead to restenosis and require further interventions to revascularize [47]. One solution that has been proposed is drug eluding stents (DES) that contain medication slowly released and therefore prevents growth of tissues.

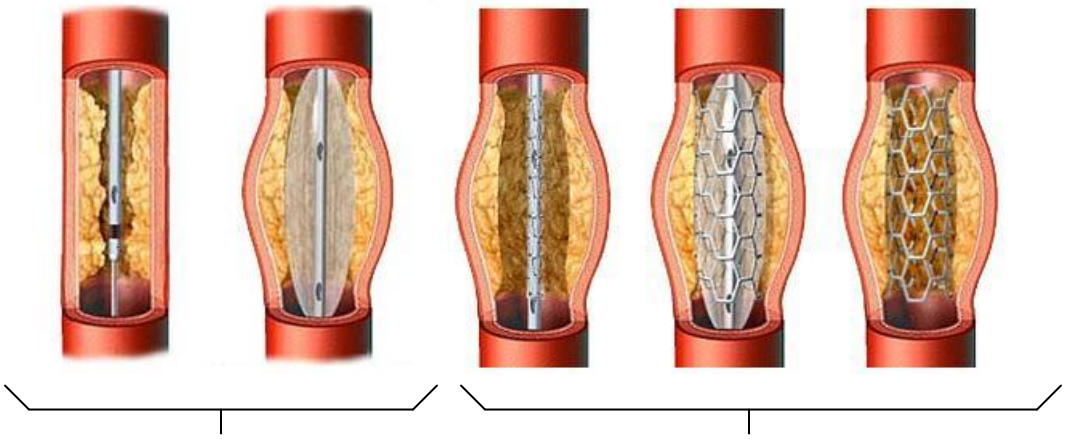

(a) (b)

Figure 1.21: Balloon angioplasty (a) and stent placement (b) [46].

Atherectomy

Atherectomy attempts to remove plaque rather than apply a radial force such as with balloon angioplasty. Simpson et al. was the first to try this approach on peripheral arteries in 1985 and went on to develop an instrument capable of collecting the pieces as it shreds the coronary plaque [44]. Lasers were introduced to remove plaque using heat, however

there were too many cases of vessel injuries. Other tools were developed, for example "eximers" that use "photochemical mechanisms" [44]. Other atherectomy devices include using high energy ultrasound, and a combination of a balloon and a thermal laser.

Transmyocardial laser revascularization (TMR)

In some cases, surgical interventions are not enough to remove angina pectoris. Transmyocardial laser revascularization creates small incisions over the myocardium. Those openings create blood channels through the myocardium and allow blood to reach inaccessible regions [49].

Minimally invasive surgery

Traditionally, cardiac surgery was accomplished with access to the heart through an incision in the chest, along the sternum (Figure 1.22a). Alternatively, the surgeon can access the heart with an incision between the ribs of the patient. Known as minimally invasive surgery, the heart is accessed (Figure 1.22b) frontally or sideways using endoscopic instruments. This procedure minimizes time of recovery for the patient.

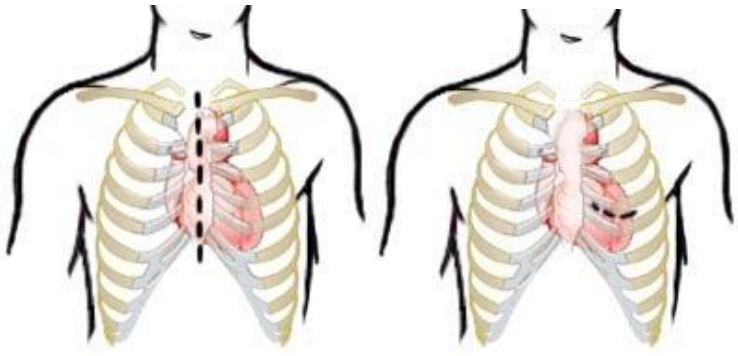

(a) (b)

Figure 1.22: Chest incision through the sternum (a), or between the ribs (b) [50].

1.6 Multimodal registration of medical images

Fusion of multimodal images for visualization requires registration: to establish a correspondence between items of a scene through the deformation of one image to fit the other. A great number of publications deal with this field [135], [136], [138], and a few aim specifically at cardiac image registration [119], [153]. In general one image is fixed and named *target* and the other is deformed to resemble it, called *source*. Registration is accomplished by overlaying involved images and finding a transformation of various natures: rigid, affine, curved, elastic or free form.

Registration techniques are generally classified into two major groups: feature-based and intensity-based methods [119], [123]. Feature-based methods align both images by matching characteristics, such as points, surfaces, or markers identified in both modalities. Such techniques sometimes require a previous segmentation of structures. Transformation of one image to fit the other is calculated from these matching features. Intensity-based methods rely on a statistical method of correspondence of intensities in both modalities.

Challenges

Multimodal registration proves challenging due to the nature of the task since image formation exploits different physical interactions and the same organ is therefore rendered with different intensities in the resulting images. For example while some organs such as bones are clearly visible in CT they are difficult to identify in DEMR images. This problem prevents usual intensity-based registration techniques from being effective. For this reason, linear correspondence of intensities or simple correlation cannot be applied since there is no direct relation in intensities in the same organ in images from different modalities. There are multiple approaches to this problem in

multimodal registration. Mutual information, for example, is an intensity-based method that has proven reliable in many cases.

Structural and functional information are not analyzed in the same set of images and multimodal images are involved. For example in the presence of CHD the location of damage to the myocardial cells should be associated with the responsible blocked coronary. Correspondence of information found in both modalities is required. Multimodal registration methods are described with emphasis on imaging methods related to the cardiac field.

1.6.1 Principal Component Analysis

Lu and Chen [126] applied an initial rigid registration using PCA. This feature based method identifies the orthogonal directions of maximal dispersion in a cloud of points. Given a cloud of points *P* in 3D space, a (3 x *n*) position matrix *X* is built where all columns contain the position (*x*,*y*,*z*) of a point. A correlation matrix *C* measures the correlation between random variables (between all 3D point positions), and is calculated by [126]:

$$C = \frac{1}{n}\sum_{i=1}^{n} X_i X_i^T - uu^T \qquad 1\text{-}1$$

with *u* the mean position calculated by the average position found in *X*. The three orthogonal directions of dispersion of points are identified by eigenvectors *e1*, *e2* and *e3* extracted from *C*. Each eigenvector is associated with an eigenvalue λ such that $EX = \lambda X$, where *E* is a row matrix of eigenvectors, ordered by decreasing value of eigenvalues. The

eigenvector associated to the highest eigenvalue indicates the direction of maximal distribution of the cloud of points. Once normalized, the three orthogonal eigenvectors form a coordinate system (*e1, e2, e3*) that can also be used as a rotation matrix for registration purposes [125].

Given two clouds of points in images from distinct modalities, registration and therefore transformation (rotation/translation) from this new coordinate system to the world coordinate system, and vice versa, is calculated with the rotation matrix *E*. Registration between two distinct populations of points is therefore accomplished by a series of translations and rotations from *E* [126]:

$$X_B = (E_B E_A^T (X_A - u_A)) + u_B \qquad 1\text{-}2$$

where *A* identifies the moving image, *B* the fixed image, and the mean position *u* is calculated from both points sets and used as translation vectors.

The moving volume is first translated to the center of the world by subtracting u_A from all point position belonging to that image, it then undergoes a rotation E_A^T in order to have the principal axis correspond with the world coordinate axis *x*. A rotation E_B is then applied to align the direction of highest distribution from the point set of *A* to that of *B*. The last step is a translation from the center of the world to the center of the cloud of points of *B* by a value equivalent to the average position of points (u_B). After these transformations, the two volumes are rigidly registered along the approximated long axis direction (principal component) of the cloud of points. A possible scaling is necessary with regards to both sets of points to complete the rigid transformation.

1.6.2 Mutual Information

Entropy is introduced by Hartley in 1928 [110] to address the problem of message transmission in telecommunications. His definition is based on the length of a message, *n*, and the number of possible symbols, *s*, in a message as calculated by:

$$H = n \log s \tag{1-3}$$

This is evaluated for *s* having the same probability of occurrence for all possible components of a signal. Shannon introduced this probability in entropy calculation as follows:

$$H = -\sum_i p_i \log p_i \tag{1-4}$$

where p is the probability of occurrence. This last equation is used in mutual information [138], presented by Collignon and col. [112] as well as Viola and Wells [111] in 1995. This method relies on intensities, through a statistical model of correspondence, for multimodal registration. Normalized mutual information was introduced to diminish the impact of area of overlap during registration [113].

Histograms

Entropy calculation requires probability values that can be approximated through histograms. Two marginal histograms are created for each of the images involved and one joint histogram is built for the overlaid images. Marginal histograms are commonly

used and consist in simply adding up the number of occurrence of intensities in a single image. The result is placed in a predefined bin interval, whose number varies depending on the application. In multimodal image registration, a number of bins equal to 256 has been sufficient to obtain reasonably good registration results [107].

Each entry of the joint histogram represents the quantification of occurrence of intensity pairs from both images to be registered. More precisely, if we define $I_A(x)$ as the intensity found at position x in image A, and $I_B(x)$ as the intensity found at the same position x in image B, the two dimensional histogram bins are incremented by one at positions corresponding to ($I_A(x)$, $I_B(x)$). The joint histogram can be represented by a 2D image where bright areas indicate a high frequency of occurrence of intensity pairs. In the case of two perfectly aligned identical images, the histogram will show a diagonal (Figure 1.23), for each intensity found in image A, its exact match is found at the same position in image B. Misregistered images results in a spread of bright values over the histogram. After normalizing all entries of marginal and joint histograms, these values can be used as probabilities for entropy calculation.

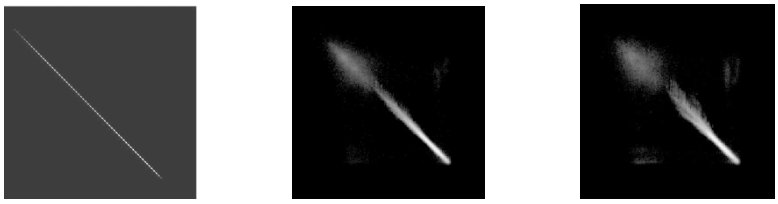

(a) (b) (c)

Figure 1.23 : Joint histogram images where values found in the reference image are placed over the abscissa axis and those from the moving image are placed on the ordinate axis. The joint histograms were created from identical CT images, perfectly aligned in (a) and with a rotation R applied to one of the images, R = 5 (b) and R = 10 (c).

When calculating joint histograms, voxel correspondence is not guaranteed over the overlapping parts of source and target since resolution varies, without grid correspondence: thus interpolation has to be performed. While updating the joint histogram new intensities are introduced using classical interpolation methods such as nearest neighbor (NN) or trilinear interpolation. A comparative study of interpolation methods has been published and gives a number of recommendations to diminish interpolation artifacts in mutual information [31]. Interpolation methods were studied by Maes et al. in 1997 [114] who worked with partial volume interpolation (PVI) in order to obtain subvoxel accuracy. Instead of interpolating new intensity values and updating the joint histogram bin of the new value by one, this method increments, by a fractional weight, several joint histogram bins corresponding to a group of nearest neighbor voxels. A generalization of this method (GPVI) was later developed by Chen and Varshney [116]. They introduce the concept of a kernel function to increment the joint histograms bins and use B-splines to determine update of joint histogram bins corresponding to the nearest voxels. Another kernel function was suggested by Lu et al. [117] using a Hanning windowed sinc to update the joint histogram. Seppa [118] suggests applying continuous sampling in mutual information calculations. Distribution of intensities over histogram bins have also been determined by k-means clustering [147].

Properties of mutual information

In theory, MI is symmetric ($MI(A,B) = MI(B,A)$) and the amount of information of each image on the other is the same. However this property doesn't hold in imaging since point matching cannot be guaranteed, due to the multiresolution of multimodal images and involving the interpolation of intensities involved. The entropy of an image is equal to the mutual information calculated over both identical images ($MI(A,A) = H(A)$).The amount of information an image contains of itself is equal to its entropy. Mutual information value from two overlaid images can never be of greater value than the

entropy of each single image ($MI(A,B) \leq H(A) or H(B)$). Mutual information will always be positive and will only equal zero (0) when both variables involved are independent (there is no information in one of the image concerning the other).

Initialization methods

Initialization methods can be used to roughly align volumes prior to calculations and can be accomplished by establishing the patient position and orientation in both acquisition machines by reading the information present in the DICOM header files [123] or based on principal component analysis when models are available in the volume [30]. Principal Component Analysis (PCA) has previously been used alone as a rigid registration and proved to be useful in initialization of mutual information, diminishing the search in the transformation domain, therefore reducing the number of iterations.

Optimization methods

When using mutual information, calculations have to be done in the entire transformation domain to find the optimal value, unless an optimization method is used to accelerate the search. Optimization methods aim at reducing the execution time. Comparative studies of optimization methods have been published [122] but the Powell-Brent method has been mentioned several times as the best option for MI [123], [114], [117].

Minimization of execution time

Some have opted to modify the hardware structures of computers to accelerate calculations [164], [181], while others have turned to GPU programming, consisting in using the graphical unit interface in order to parallelize calculations [165], [166], [167].

Improvement

A great number of publications have followed the first papers concerning MI as a registration metric. They deal with different factors involved in the registration calculation or bring new ideas to the method in order to augment its robustness or apply it in more challenging situations. Calculations are based on entropy and measure the amount of dependence between two images, calculated with joint and marginal histograms or approximations such as with Parzen windows [138]. Even if the molecular response of one organ varies depending on the imaging device, there is uniformity of intensity in a specific organ in one modality [138] that allows for a statistical correspondence between multimodal images. This also implies that organs have the same size in all images to register so that a spatial correspondence can be accounted for within the entropy calculation. In some cases, information on spatial correspondence is introduced in the calculations [139], using gradients: measuring a distance gradient factor [141], [142], [143] or introducing a gradient code map [144], [145].

Application

SPECT is registered with ultrasound images in order to establish correspondence of structural information using mutual information [79]. SPECT images are also registered to cine MR using the movement of the heart for segmentation of the LV in MR, subsequently using a mutual information algorithm to register the segmented LV to SPECT images [81]. CT and MR volumes enclosing the heart have previously been registered by Klein et al.[93], using mutual information.

1.6.3 Thin Plate Spline

An elastic registration can be accomplished by a landmark matching method such as thin plate spline (TPS). It defines a deformation field based on the minimal energy needed to deform a thin and flat plate by bending it from a source to a target position as described by a set of source and target landmarks [168]. This method was described by Rohr in 2001 [169] who introduced localization errors for landmarks. In the example case of 2D images, displacement in the image plane is done by an interpolant, calculating over the image a minimizing function that quantifies the amount of energy needed to deform a flat thin plate in a direction perpendicular to its plane (in 3D). The energy at a position (*x*,*y*) on the steel plate is proportional to the second derivative at the out of plane position:

$$\left(\frac{\partial^2 z}{\partial x^2}\right)^2 + 2*\left(\frac{\partial^2 z}{\partial x \partial y}\right)^2 + \left(\frac{\partial^2 z}{\partial y^2}\right)^2 \qquad 1\text{-}5$$

where *z* is a function of x and y, that depends on source and target landmarks, and defined by a basis function *U* and that minimizes:

$$\iint_{\Re^2}\left(\left(\frac{\partial^2 z}{\partial x^2}\right)^2 + 2*\left(\frac{\partial^2 z}{\partial x \partial y}\right)^2 + \left(\frac{\partial^2 z}{\partial y^2}\right)^2\right)dxdy \qquad 1\text{-}6$$

Displacement found in the z direction is mapped onto the image to find the deformation field. To generalize to a *d* dimension space, transformation is described in each dimension *k=1...d* by a transformation component u_k with source p_i and target q_i landmarks, *i=1..n* where *n* is the number of landmarks. The functional to minimize is therefore a sum of individual components that depend on one transformation component

(equation 1-7 and 1-8 where m is the derivative order and α is related to the partial derivative order).

$$J_m^d(u) = \sum_{k=1}^{d} J_m^d(u_k) \tag{1-7}$$

$$J_m^d(u_k) = \sum_{\alpha_1+\ldots+\alpha_d=m} \frac{m!}{\alpha_1!\ldots\alpha_d!} \int_{\Re^4} \left(\frac{\partial^m u_k}{\partial x_1^{\alpha_1} \ldots \partial x_d^{\alpha_d}} \right)^2 dx \tag{1-8}$$

The functional can be stated in analytical form as:

$$u(x) = \sum_{v=1}^{M} a_v \phi_v(x) + \sum_{i=1}^{n} w_i U(x, p_i) \tag{1-9}$$

where $U(x, p_i)$ is the basis function and ϕ is a polynomial. The solution is reached by finding parameters a_i and w_i using a linear system of equations:

$$Kw + Pa = v \tag{1-10}$$

$$P^T w = 0 .$$

Parameter K is the set of basis function $U(p_i, q_i)$, P is the set of polynomials $\phi(p_i)$, v is a component of the coordinate of target landmarks in vector form, $a = (a_1, a_2, \ldots, a_M)^T$ and w = $(w_1, w_2, \ldots, w_n)^T$. Solving this system implies that correspondence between the two sets of landmarks is done by exact matching of landmarks.

1.6.4 Multimodal registration of cardiac images

Registration presents added challenge in cardiology, mainly due to the constant movement of the heart but also due to breathing, both necessary to sustain life and impossible to stop completely. Cardiac image registration is therefore ideally non-rigid because the heart is a flexible organ and because of movement involved during the imaging process [119]. To diminish the effect of heart beat, acquisitions gated at end systole (determined by ECG) when there is minimal motion, but timing cannot be guaranteed and any registration method has to account for this possible inaccuracy. It is therefore clear that using external landmarks as matching features is ill-suited in cardiology since the markers do not follow the motion of internal organs [119]. Moreover, there are few identifiable features of the heart and in particular in the presence of pathologies, for example myocardial ischemia can alter the physical aspect of the LV. Internal landmarks are therefore difficult to identify in the images and moreover to match in between modalities [119].

Bias field

The uniformity of an organs' intensity within an image is important but can sometimes be altered during image formation. This is the case in MR images where intensities will be brighter in parts of organs closer to the skin within proximity to the RF coil [146], [147]. This phenomenon is referred to as the bias field, bias artifact or RF-inhomogeneity. One method of correction consists of calculating the exact effect of intensity variation, as found in MR images taken free of scanned subjects, and to subtract the resulting image from a patient's MR scan in order to obtain an image without bias field [148]. Methods exist that don't necessitate an additional image acquisition. Homomorphic filters have been applied to smooth intensity variation inside a same organ [149]. This filter affects

edges and later methods aim at diminishing this artifact [150]. Recent methods introduce Gabor filters for bias field correction [151].

Contrast Agent

Still on the matter of uniform intensity inside an organ comes an even bigger problem: the use of contrast agents during CHD diagnosis. The use of these agents make parts of the myocardium appear brighter, a desirable effect to emphasize ischemia localization but a challenge in the registration field.

Orientation of volumes in space

Acquisition of multimodal images is not simultaneous in time, implying movement of the patient between acquisitions. While it would be possible to use the patient orientation as available in the DICOM files, it does not guarantee internal correspondence of organs, specifically of the heart in constant movement. The different acquisition systems used result in completely different slice orientation as well as different reference frames to establish patient position.

Transformation

Since the heart is a flexible organ, the transformation applied to the images needs to follow its border and therefore allow for a non-rigid deformation. An interesting approach in generic registration is to use a combination of methods such as described by Lu and Chen's [30]. They present a combination of rigid registration methods: feature-based to consider the spatial distribution of the heart with the use of principal component analysis (PCA) method and intensity-based applied with mutual information when no

features can be identified to guide the registration. For cardiac applications, a further elastic registration is necessary to complete the process.

Klein et al. [127] have used a B-spline deformation, along with mutual information registration, in order to register CT and MR medical volumes enclosing the heart. The feature based iterative closest point method [120] was used by Sturm et al. [127] in 2005 to register MR and CT images of the heart. This successful method does not accomplish registration automatically in the short axis plane where no LV characteristic features can be matched between images and requires manual identification of matching points (the meeting location of LV and RV walls). More recently Chenoune et al. [123] have registered (2D+*t*) MR and (3D+*t*) CT images using the intensity based method mutual information (MI) and Powel's direction set method for optimization, they also use a Gaussian pyramid approach. Their study aimed at identifying the myocardium's motion through the cardiac cycle and during the acquisition they used no contrast agent and as such had no intensity variation within tissues.

1.7 Myocardium segment model

In the presence of CHD and in clinical practice, physicians want to establish the extent of damage to the tissue of the left ventricle. Once this is known, the source of the damage (the responsible coronary) should be identified and eventually revascularization preformed if it is judged as an appropriate therapy for the patient. In some cases a patient might have various locations of coronary stenosis. However intervention could be needed only in the location responsible for the ischemia. If coronary territories are determined over the cardiac muscle surface, association of a specific coronary to the myocardial lesion could be established. Ideally, specific regions of myocardium would be tagged to a specific coronary and knowing where the damage is would lead us to know the exact

location of a stenosis. For the moment, clinicians rely on an empirical population-based model as described in section 1.4.

An algorithm should be chosen that would best describe the blood irrigation of the coronaries to the myocardium. Intuitively we can start by saying that the closest coronary to any point on the epicardial would determine the association. This translates into a shortest path problem over the segmented model of the LV. In computer vision, this problem is stated as the calculation of a path over a graph that would yield the lowest cost as calculated between two specific vertices [173]. There are two ways of addressing this task: calculating paths for a *single source* (between a point and every other point of the surface), and for *all pairs* (between all pairs of points over the surface) [174]. This problem has previously been addressed using a marching cube algorithm [175]. Methods such as region growing can be used to solve this problem by establishing regions over a surface and respecting the constraint of encapsulating one point in one region. Dijkstra's algorithm was published in 1959 [177]. All edges are given a specific and positive weight and a total distance between two points is given by the sum of all the edge weights lying between them.

Validation methods

Validation of coronary territories over the myocardium has previously been done using a technique known as the Green Lane method [179] that was recently applied to CT images [180]. Each patient's coronary arteries, and branch vessels, are transcribed onto a standard diagram by an expert cardiovascular imager. The relative size and distribution of each vessel is preserved with this method, as well as the individual variation in coronary anatomy. Figure 1.24 shows an example result of coronary territories as drawn by an expert.

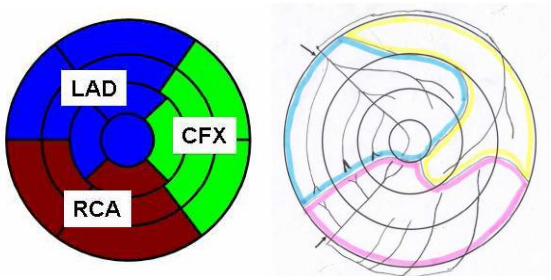

(a) (b)

Figure 1.24 (a) The 17-Segment Model: cross sections of the LV perpendicular to long axis (apex, apical, mid and basal portions). The septum is to the left. Three regions are found to be typically irrigated by the Left Anterior Descending (LAD), the Left Circumflex (CFX) and the Right Coronary Artery (RCA). (b) Green Lane Method: an experienced cardiac radiologist manually transcribes the coronary tree, with branch vessels, from a coronary angiogram onto a bull's eye plot. The plot is then divided into coronary distribution regions based on these projections (LAD blue, CFX yellow, RCA pink).

1.8 Research objectives

The empirical population-based 17-segment model is currently used in clinical practice and has proven reliable in predicting the location of coronary obstruction relying only on location of damaged myocardial tissues. After a viability study (by MR or nuclear imaging) the clinician uses the viability map to infer the location of coronary obstruction. After this process the clinician performs an angiogram to precisely know the coronary structure and locate coronary occlusion. However the physician could only benefit from an enhanced model where coronary structure would be combined to myocardial viability and moreover adapted to each individual patient's structural anatomy.

Our main objective is to accomplish a patient-specific map combining coronary territories computed from CTA volumes (that offer only structural information) and myocardial viability extracted from DEMR images (where myocardial function is visible). Fusion of both images is needed in order to guarantee correspondence of structure over function in the final map. A global view of the project work is shown in Figure 1.25.

The first objective consists in computing the 3D territories of coronary arteries over the epicardial surface in the CTA volume. We are interested in knowing the area of myocardial perfusion for each coronary for an individual patient. Once the coronary territories are known, borders can be established over a map by polar projection of points from 3D to 2D. This map only contains morphological information and functional imaging is exploited to complete the map with viability information.

The second objective therefore consists in the projection of myocardial viability information over a 2D map. The location, transmural extent and area of diseased tissue interest the clinician in order for him to evaluate chances of recovery for the patient after a possible intervention. This viability model does not relate any structural information and the clinician relates to a population based model that indicates the most probable diseased coronary. A viability model augmented with structural information concerning a patient's coronary tree structure could help to associate the identification of dead tissues to a specific coronary without the use of angiograms.

The third objective of this project is therefore to accomplish an automatic 3D registration of myocardial surfaces found in both modalities, CTA and DEMR. The segmentation

models of the myocardial surfaces are available in both sets of images and can be exploited in a feature based registration approach wich results in the alignement of myocardial models from both modalities. However motion of the patient between acquisitions (due to breathing as well as the heart beat but moreover to the shape of the heart that is altered by the presence of pathology) limits registration results. The method should therefore be coupled to an intensity based approach that should complete the registration. Only after having found the correspondence of myocardium surfaces can both structural and functional information be projected onto a coherent viability map.

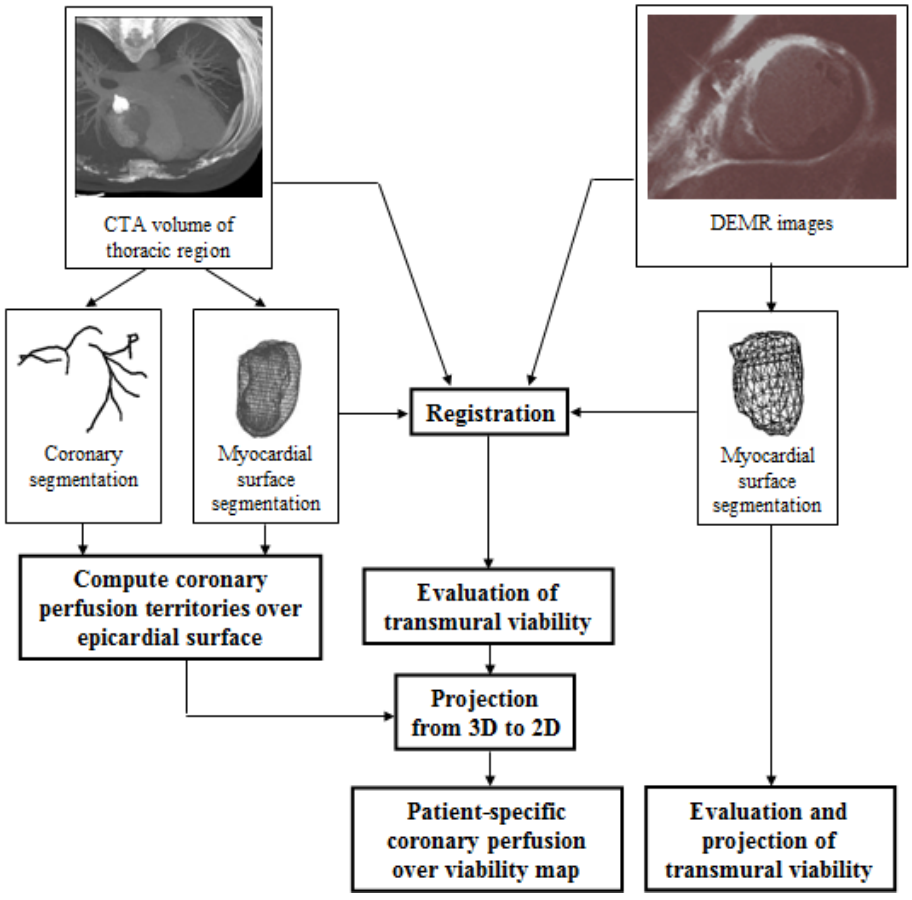

Figure 1.25 : Creation of a patient-specific diagnosis tool in the presence of coronary artery disease. Each step of the current project is written in bold.

CHAPITRE 2 METHODOLOGY

A personalized viability map is created in an attempt to evaluate myocardial function and to associate regions of the heart's surface to a specific coronary. This map should allow the clinician to identify areas of damage to the cardiac tissue and simultaneously present the coronary tree structure of the same patient. This task requires two sets of images: a structural and another functional imaging modality. CTA volume and a series of DEMR slices of the heart are chosen. DEMR offers the advantage of being non invasive as well as remove the risk of exposure of the patient to radioactive agents such as in nuclear studies. Both sets are obtained from the Cleveland Clinic in the United States. Patients first went through CTA acquisition. Coronary territories are computed over the myocardial surface in this volume with the use of an available coronary segmentation given by an experienced clinician. The same patients also underwent a DEMR acquisition. Viability is evaluated from this functional imaging modality and based on the the available myocardium segmentation in the image sequence. The final viability map shows both functional and structural information, fusion over the final map being guaranteed by a 3D registration of both volumes. The first step of registration is fulfilled by a feature based registration method, principal component analysis, exploiting the available geodesic models in both volumes. A deformation of surface models is done with the use of a thin plate spline algorithm to exaclty fit both surfaces to one another. Final registration is only reached after an intensity-based method, mutual information, completes the registration step.

2.1 Coronary territories from CTA images

Available data

The available CTA volume is obtained using either a 16 slice (n=2) or 64 slice (n=5) scanner (Sensation 16/64, Siemens Medical Solutions, Forcheim, Germany), and volumes were reconstructed at 55-70% of the cardiac cycle. Contrast agent transit time was determined using a 10-20 milliliter (mL) timing bolus (Ultravist 300, Berlex, Wayne, NJ). For each patient, a 3D delineation of the LV was available in CTA as a geodesic model of the endocardium and the epicardium. This information served to establish coronary territories over the myocardium in CTA. The models were defined by a series of points and their connections.

Coronary arteries' paths were given by a series of points located in the CTA volume. This modality offers structural information of the coronary tree. A qualified clinician manually selects the coronary paths by examining the CTA slice by slice. The result is an interpolated series of points classified under three main groups:

1) The left anterior descending artery (LAD) group is composed of the left main coronary and possibly any diagonal branches.
2) The right coronary artery (RCA) group which includes the RCA, the PDA and associated branches.
3) The left circumflex artery (LCX) and any of its branches.

In the occurrence of CHD, an occlusion may occur in any portion of the coronary tree, including diagonal branches of any of the main three coronaries. Any diagonal branch can therefore form its own category as decided by the expert. This is particularly helpful to the clinician in the case of scar or ischemia in a region irrigated by a branch belonging

to a coronary other than the typical main coronary over this region. There may therefore be more than three coronary groups in the coronary classification, as decided by the expert.

Coronary territories computation

Coronary territories are established in 3D over the LV surface, assuming the existence of a 3D polygonal model of the myocardium. Each point of the given model is assigned to a specific coronary. Territories are formed by grouping model points that are hypothesized to belong to a same coronary group.

We first used a region growing algorithm using coronary points as seeds of regions [176]. These seeds are chosen from all the surface points as the closest one to the ground truth coronary paths. Regions progressively grew from these seeds, expanding over the surface following interconnections of points and assigning conquered points to the region that reached it first. This method was considered biased by the way in which regions expanded over the surface. Since each region expands one after the other, a region could reach a surface point first, however this did not guarantee that this point wasn't closer to another coronary group. The result could be sublte but change the final coronary territories drawn over the surface when changing the order of expantion of each region.

In this work, Dijkstra's shortest path algorithm is the method chosen to determine territories, because of its efficiency and since it eliminates the bias involved in the region growing algorithm. This algorithm is calculated over positive weighted edges. The LV external surface (the epicardium) is available as a polygonal model Q, and may be described in terms of nodes, v, which are connected by weighted edges. Weights, W, are therefore distance values between two nodes, as calculated in Euclidean space and with

respect to voxel spacing as found in the DICOM files of the available volumes. The shortest path problem reduces to finding the shortest path from a source point, the coronary point projected onto the LV surface, to a destination point (all other point of the surface). Dijkstra's algorithm (well described by Waldura [137]), determines the shortest paths from the source point on the LV surface by progressively adding the traversed edges to a list of current paths and selecting the minimal total distance path reaching the surface points. Algorithm 1 defines each step of Dijkstra's algorithm and how it has been exploited to assign a surface point to a specific coronary group. The algorithm has a performance of $O(n^2)$.

Algorithm 1: Shortest path calculation from LV correspondent coronary points to all other surface points and assignement of points to coronary perfusion regions.

Definition:

- → ***b*** => set of best estimates of shortest distance over the surface between two points
- → $\boldsymbol{P_{LV}}$ => set of all surface points
- → ***s*** => set of coronary surface points
- → ***P*** => set of precedent LV points of each shortest paths from the LV coronary surface point, ***s***
- → ***F*** => set of surface points whose shortest paths have been found
- → ***Q*** => set of unvisited vertices

Initialization:

→ $\boldsymbol{b}(\boldsymbol{v}) = \infty$;

→ $\boldsymbol{P}$, $\boldsymbol{F}$ and $\boldsymbol{Q}$ = empty;

→ $\boldsymbol{Q} = \boldsymbol{Q} \cup \{s\}$;

→ $\boldsymbol{D}(\boldsymbol{s}) = 0$;

Dijkstra:

Loop as long as $\boldsymbol{Q}$ is not empty:

1. find $\boldsymbol{u}$ such that $\boldsymbol{b}(\boldsymbol{u}) = \min \{ \boldsymbol{b}(\boldsymbol{v}) \mid \boldsymbol{v} \in \boldsymbol{Q} \}$

   remove $\boldsymbol{u}$ from $\boldsymbol{Q}$,

2. $\boldsymbol{F} = \boldsymbol{F} \cup \{ \boldsymbol{u} \}$

3. For each $\boldsymbol{v}$ adjacent to $\boldsymbol{u}$ and with $\boldsymbol{v} \notin \boldsymbol{F}$

4. If $\boldsymbol{d}(\boldsymbol{v}) > \boldsymbol{b}(\boldsymbol{u}) + \boldsymbol{W}(\boldsymbol{u},\boldsymbol{v})$

5. set : $\boldsymbol{b}(\boldsymbol{v}) = \boldsymbol{b}(\boldsymbol{u}) + \boldsymbol{W}(\boldsymbol{u},\boldsymbol{v})$

   $\boldsymbol{P}(\boldsymbol{v}) = \boldsymbol{u}$,

   $\boldsymbol{Q} = \boldsymbol{Q} \cup \{ \boldsymbol{v} \}$

6. Return to 1.

Find coronary territories:

1. Loop over $\boldsymbol{s}$

2. Execute *Dijkstra* from $\boldsymbol{s_i}$ to every other $\boldsymbol{P_{LV}}$.

3. Loop over $\boldsymbol{P_{LV}}$
4. Assign coronary group based on shortest path found.

For visual purposes, each coronary set is assigned a color. The result is a 3D colored model of coronary territories. The coronary points given by the clinician are classified into three major groups (LAD, RCA, LCX). Alternatively, the physician could submit a third group of coronary points such as a branch of the LAD. The specific color code is described in Table 2-1. The border of a coronary region is determined as a path along which points and at least one of their closest neighbors have been associated with different coronaries. These coronary regions are considered the area of perfusion of a coronary group. This information can benefit the clinician in the diagnosis process if he could deduce wich coronary is responsible for the perfusion of an area where dead tissues was located. This is possible if viability information was available along with the coronary territories identified.

Table 2-1: Coronary color code.

Coronary	**Color**
LAD	Blue
RCA	Red/brown
LCX	Green
Branch	yellow

2.2 Fusion of structural and functional information

Upon analyzing viability maps, the clinician should be able to associate an area of dead tissue to a corresponding coronary group and therefore identify the most likely diseased coronary. Once coronary territories and myocardial function have been interpreted they need to be fused to have correspondence in the projection of anatomy. Viability is extracted from the DEMR sequence of images.

Available data

Function is inferred from DEMR images by analyzing the signal intensity of the image. Bright areas of the myocardium indicate a possible site of scar. A contrast agent is administered to the patient and image acquisition is done after a known delay corresponding to a certain wash out rate of healthy myocardial cells. After that delay, any cells that still retain the contrast agent is considered dead, this phenomena hypothesized to be caused by the slow wash out rate of dead cells. The acquisition of DEMR images was done using a 1.5 Tesla imager (Sonata; Siemens Medical Solutions, Erlangen, Germany). Approximately 20 minutes after intravenous injection of 0.2 mmol/kg gadopentetate dimeglumine (from Magnevist; Berlex Laboratories, Wayne, in New Jersey), short axis delayed enhancement MR imaging was performed by using an inversion-recovery T1-weighted segmented gradient echo pulse sequence (repetition time of 8msec.; echo time of 4msec.; inverse time between 175msec. and 275msec). Flip angle, 30°; and 23 lines acquired every other R-R interval, with field of view and matrix values matching those of the cine acquisition) (3,5). The optimal inversion time to null the signal from viable myocardium was determined individually for each patient. In addition, long-axis cine and delayed enhancement MR images were acquired in vertical (two chamber), LV outflow tract (three chamber), and horizontal (four chamber) orientations.

We chose to proceed to a 3D registration of available volumes based on a hybrid approach since segmentation of the myocardium is available in CTA as well as DEMR. The available epicardium as well as the endocardium surfaces are therefore used in a feature based registration. Principal component analysis is applied to roughly align surfaces from both sets of images (CTA and DEMR). However this process can only serve as an initialization since the myocardium surface does not suffice to correctly align the surrounding organs. An intensity-based registration method is applied by employing mutual information (which has proven reliable in multimodal image registration) as a means of evaluating registration from the information (intensities) contained in the volume and thin plate spline is used to deform the polygonal model so that they fit over one another. The search for the best transformation stops once the optimal value of mutual information has been found. The pseudo code for this sequence of operation is described in Algorithm 2.

Algorithm 2: Combined registration method.

Definitions:

→ let S_D be the set of DEMR geodesic models of the endocardium and the epicardium surfaces

→ let S_C be the set of CTA geodesic models of the endocardium and the epicardium surfaces

→ let T be a set of transformation (translation and rotation) inside a limited interval around the long axis of the heart and with a set of delta increments for each transformation.

Initialization:

→ accomplish feature-based registration to align S_D and S_C along their long axis using principal component analysis.

Execution:

Loop over T:

→ Apply T to the CTA volume.

→ Deform S_C to fit exactly over S_D by using a thin plate spline deformation.

→ Apply an intensity-based method (mutual information) to complete registration.

→ Store mutual information value found.

Select the best set of transformation based on the highest value of mutual information stored.

2.2.1 Feature-based Initialization of registration

The inherent orientation of images to be registered is with respect to the imaging devices involved. Initialization of registration is accomplished by Principal Component Analysis (PCA). This step rigidly aligns polygonal models by superimposing regions of interest (the LV). As a result the LV in both DEMR and CTA images are roughly overlaid in 3D. To apply the PCA method, a cloud of points needs to be identified. Points from the respective DEMR and CTA geodesic models are used. The correlation matrix is built from these sets of points and the eigenvalue decomposition results in a set of three orthogonal vectors used to form a rotation matrix for the alignment of the models. Since the long axis traverses the heart in the direction where it is the longest [34], it is therefore

approximated as the direction of maximal dispersion found by PCA. We rigidly register MR and CT images by aligning the principal direction found in both models.

This rough initial estimation of the registration suffers from the lack of features available in the other (orthogonal) directions. The second and third direction vectors (*e2* and *e3*) given by PCA lie in the short axis plane, where the LV myocardium has a shape similar to a circle, as seen in Figure 2.1. Although these vectors were usefull in the creation of the 3x3 rotation matrix, their proper alignment is underdetermined. The slight variation in curvature along the LV border cannot be used for registration due to the motion between acquisitions but moreover because ischemia transforms the physical aspect of the LV, thinning the myocardial wall. Further analysis is needed to complete the registration since the characteristics of the geodesic model are fully exploited by the long axis alignment.

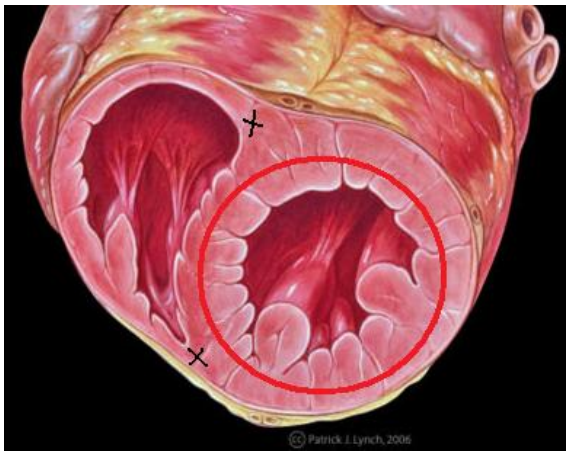

Figure 2.1: schematic representation of the LV in the short axis plane.

Emphasized by the red line is the circular shape of the LV in this view.

Junction of the RV and LV are highlighted with two black X.

2.2.2 Free form deformation of surfaces with Thin Plate Spline

Landmark identification

Thin plate spline fitting consists of finding a deformation according to given source and target landmarks and possibly including localization errors. Since the CT volume has a higher resolution, it will be deformed towards the MR volume, therefore the points form the 3D geodesic model found in the CT volume are tagged “the source landmarks” and the ones from the MR model found are tagged as “the target landmarks.” However both models do not contain the same amount of points since the MR images are of lower resolution. Since the thin plate spline algorithm accomplishes a one to one matching, a selection is done to keep only points from the CTA model that have a match in the DEMR model. After applying the PCA algorithm, both models are aligned in a satisfying way and landmark matching can be accomplished. For every point of the MR model, a match is found in the CTA model in the following manner: trace several lines each passing through an MR point and the LV center, then trace several lines each passing through a CTA point and the LV center and match CT points that have the minimal distance to MR points as well as the smallest distance angle between the lines created, schematically represented in Figure 2.2.

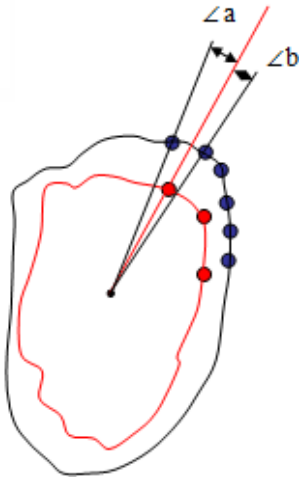

Figure 2.2 : Points from the LV surface from CTA (in black) are matched to DEMR surface points (in red) by selecting those that have the smallest distance angle to MR points, in this case *b* since ($\angle b < \angle a$).

Validation method

Exactness of medical image registration should be evaluated to quantify the precision of the method. However, without landmarks there is a lack of methods to quantify the performance of an algorithm. Although the segmented model is composed of points depicting the LV surface, these cannot be used since the TPS algorithm matches these points and any distance between the sets of landmarks would be intentionally created to counter localization errors introduced during the segmentation step. The current evaluation is by visual assessment [136].

2.2.3 Multimodal Registration Based on Intensities

Once the DEMR and CTA images have been roughly aligned by PCA, we can proceed to a more precise registration and exploit the intensity information contained in each available volume. Mutual information is a known method that has proven reliable in the registration of images based solely on the information contained in images. In the short axis slices the LV insertion points (the junction of the RV onto the LV wall, see Figure 2.1) is a reliable feature previously used for manual registration of MR and CT images of the heart [127]. Our hope is that mutual information (MI) will accomplish this step automatically by statistical measure of correspondence from intensities found in images of both modalities. However, MI is known to have a long execution time, an aspect we hope to lessen since PCA brings models from both modalities into a rough alignment and should limit the search in the transformation domain. Mutual information is applied in conjunction with a deformation method, TPS, that affects the model before each MI calculation.

Preprocessing filter

Intensity-based methods have proven to be reliable during multimodal image registration. However any physical phenomena of image creation that alters the intensity composition of an organ might impact the result of registration. The noise present in images as well as the indistictive borders of the image might impact the registration. We choose to apply an adaptive shock-diffusion (SD) filter to DEMR that is meant to enhance quality of the image by enhancing borders while preserving homogeneous intensity structures. Elements of the SD filter are presented by Weickert [130], Alvarez et al. [132] and Remaki et al. [133]. This filter joins two partial differential based filters, a shock and diffusion filter, where *u* is the image:

$$\partial_t u = \alpha_d \cdot div[D\nabla u] - \alpha_c \cdot a(\Delta) F\left(\partial_{\vec{\eta}\vec{\eta}} u, \partial_{\vec{\eta}} u\right) u_{\vec{\eta}} \qquad 2\text{-}1$$

In equation 2-1 the weight given to each filter for a more or less pronounced effect is controlled by two factors α_d (which controls the diffusion) and α_c (which controls the shock).

The non-linear diffusion filter controlled by α_d in equation 2.1 tends to smooth along edges, therefore preserving them. It employs a diffusion tensor, *D*, which is defined by a structure tensor matrix, $J_\rho(\nabla u_\sigma)$. This method is described by Weickert [130]. He makes the gradient of a Gaussian invariant to sign by using a tensor product and applying a component-wise convolution with a Gaussian:

$$J_\rho(\nabla u_\sigma) = G * \left(\nabla u_\sigma \otimes \nabla u_\sigma\right) \qquad 2\text{-}2$$

where *G* is the Gaussian

$$G = \frac{1}{2\pi\sigma^2} \cdot \exp\left(\frac{\left|x^2 + y^2\right|}{2\sigma^2}\right). \qquad 2\text{-}3$$

The matrix *J* is symmetric, positive, and semi-definite and eigenvalue decomposition gives eigenvectors that indicate directions of fluctuation in texture. The eigenvector related to the smallest eigenvalue corresponds to the orientation of smallest fluctuation.

The shock filter is employed to enhance borders and correct the effect of the diffusion filter at edges. Osher and Rudin [131] had proposed a method that used the zero-crossing of a laplacian position. However this model was sensitive to noise and Alvarez and Mazorra [132] later developed a hyperbolic partial differential model that adjusted the position of applied shock but without considering signal features, something that was

included in Remaki and Cheriet's model [133]. The result is the following partial differential equation:

$$\partial_t u = -a(\Delta)F\left(\partial_{\eta\eta}u, \partial_\eta u\right)u_\eta \qquad 2\text{-}4$$

where *F(a,b)=sign(a) * sign(b)* and:

$$a = \begin{cases} 1-\exp(-(\Delta^2 - s^2)) & if : \Delta^2 \geq s^2 \\ 0 & else \end{cases}. \qquad 2\text{-}5$$

The filter used needs to be adapted to the image treated. Therefore the filter will have specific parameters for each DEMR image. In our implementation, a parameter specifies the proportion of shock versus diffusion. If this parameter is 0 then only a shock filter is applied, and a value of 1 indicates only a diffusion filter is applied. An alpha parameter takes the value of the diffusion factor and a third parameter is the step that guides the evolution through time of the algorithm. All these parameters were empirically chosen.

Entropy

Mutual information in the context of registration is an entropy-based method which measures correspondence of two overlaid images. Shannon's entropy is used [138]:

$$H(A) = -\sum P_A(a)\log(P_A(a)), \qquad 2\text{-}6$$

where *P* is the probability of having intensity *a* in image *A*. This quantifies the probabilistic distribution of image intensities, which give the amount of information in an image [138]. Shannon's entropy is calculated for joint images as follows:

$$H(A,B) = -\sum P_{A,B}(a,b)\log(P_{A,B}(a,b)), \quad 2\text{-}7$$

where $P_{A,B}(a,b)$ is the probability of having intensity a in image A and intensity b in image B in a corresponding position. P is evaluated by means of normalized histogram. Joint entropy measures the dependence of information, therefore the knowledge of one variable (namely an image) knowing another. When two images are independent, their joint entropy is equal to the sum of marginal entropies $H(A,B) = H(A) + H(B)$.

Correspondence of DEMR and CTA volumes using MI

There are two common ways of evaluating registration using mutual information: standard and normalized MI. Standard MI is presented in equation 2-8 where joint entropy is subtracted from the added marginal entropy of the fixed and moving image.

$$MI_{standard}(A,B) = H(A) + H(B) - H(A,B) \quad 2\text{-}8$$

We chose normalized MI [134], the sum of marginal entropies divided by the joint entropy (equation 2-9). This equation of MI diminishes the influence of background alignment on registration results.

$$MI_{normalized}(A,B) = \frac{H(A)+H(B)}{H(A,B)}. \quad 2\text{-}9$$

Mutual information is maximal when both CTA and DEMR imags are aligned and contain as much information on each other as possible, which is equivalent to the maximal correspondence of structures in the image. When looking at both MI equations it is straightforward to conclude that for a maximal value of MI, joint entropy is minimal.

While performing registration, the alignment resulting in the highest value of MI will be kept as the best result.

For a specific position given in world coordinates, there will be two specific positions relative to each coordinate system of both DEMR and CTA images. Moreover, the multiresolution of images does not guarantee grid alignment at any point in time (Figure 2.3). Interpolation is necessary to find corresponding intensities in both images at the same position in space in order to build the joint histogram. Linear interpolation, a weighed average of surrounding neighbor voxels, isn't favored since it might introduce intensity values in the histograms that weren't present in the original images. Partial volume interpolation is chosen since it increments histogram bins of a fractional value proportional to the weighted distance value from the fixed world position to the nearest neighbor grid position in an image (Figure 2.3). Different methods exist to calculate the weighted distance value, such as directly with normalized distance value or with a smoothing function.

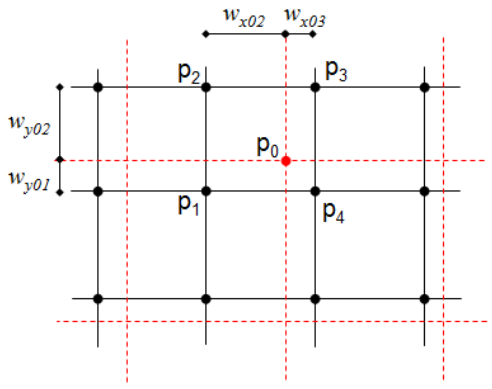

Figure 2.3: Grid correspondence during registration and distance weights for histogram calculation.

Transformation domain during mutual information calculation

The intuitive method to accomplish MI multimodal image registration is to calculate an MI value for each possible transformation T of the CTA image moving over the DEMR image sequence. The highest value of MI over the set of results indicates the best transformation found. Since we deal with 3D images, there are six degrees of freedom: three rotations (r_x, r_y, r_z) and three translation (t_x, t_y, t_z), and an infinite interval dimension in both cases. Boundaries and search intervals have to be set, especially since an initial alignment has been performed, an unbounded search would undo all previous steps. After applying PCA to DEMR and CTA, available geodesic models of the heart are rigidly registered in a direction approximately equivalent to that of the LV long axis $\vec{L}$. The search domain is therefore reduced to the vicinity of this axis. The center of both geodesic models was approximated to the average position of all points of the model (μ_{CT} and μ_{MR}), however this might not register the myocardium in a correct manner. Translations in proximity to this position will therefore be included in the search domain as well.

The limits of transformation applied to CTA are found empirically. Using the three principal component axes found previously as a reference frame for rotation angle, we limit the search to a maximal tilt angle ϕ of 20^o with regards to $\vec{L}$ (Figure 2.4). Translation is constrained to a maximal distance d_L of 1/8 of the maximal length of the LV in $\vec{L}$ direction and to a maximal distance d_S of 1/4 of the maximal length in a direction perpendicular to $\vec{L}$.

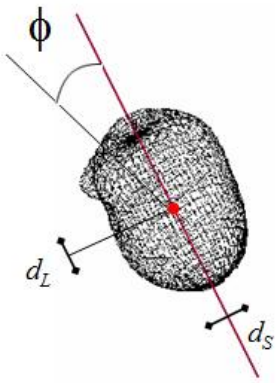

Figure 2.4: Maximal tilt and translation for transformation of moving image while searching for maximal value of mutual information.

2.3 Myocardial viability from DEMR

Viability quantification

The functional information extracted from DEMR should include the entire myocardium (both endo- and epi-cardia). Since relying on transmural intensities is considered sufficient to present myocardial function to the clinician, viability is quantified by the average of intensities along a segment between a point belonging to the epicardium and its corresponding point belonging to the endocardium (see Figure 2.5). The segment is oriented towards the center of the left ventricle and should traverse transmural scar. Dead myocardial cells are observed with DEMR images as bright areas of the myocardium, a simple projection of intensities over the 2D map is considered to be sufficient.

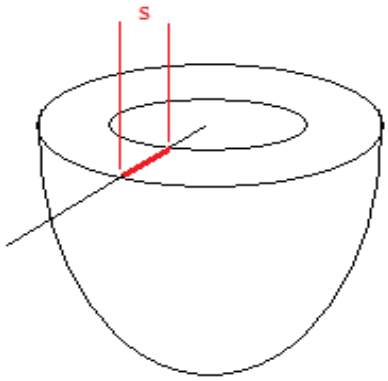

Figure 2.5: Schematic representation of viability estimation. Intensities are averaged along a segment *s* between a point belonging to the epicardium and another belonging to the endocardium

The map that we wish to create combines the viability information extracted from DEMR images to the coronary perfusion territories computed over the LV myocardial surface as described in section 2.1. However simple projection of both functional and structural information could lead to misalignement of the projected model and misguide the clinician in his diagnosis. Fusion of the multimodal images is therefore required to avoid this situation and establish correspondence between myocardial viability and its associated coronary group.

2.4 Creation of Viability Maps from 3D to 2D projection

Registration of DEMR and CTA volumes is done to guarantee correspondence of anatomy in the final viability map where non-viable myocardial tissues could be associated to a suspected diseased coronary based on the area of perfusion of a coronary over the myocardium. Once registration is done for MR and CT images, the accepted correspondence of models in 3D maintains correspondence of structure in the 2D

projected map. While picturing the left ventricle as a spheroid, unwrapping of the heart onto a polar map can be done by spherical projection. Such an unwrapping of the myocardium has previously been done using SPECT data by holistic polar map of the LV [105]. Projection from 3D onto a plane introduces distortion in the projected data. Projection using polar coordinates offers a means of projection while preserving continuity.

Viability maps are built by a simple mapping of intensities in the DEMR sequence of images, as explained in section **Erreur ! Source du renvoi introuvable.**. These intensities are unaltered by any filtering such as the shock-diffusion filter applied for registration purposes. In the case of coronary perfusion territories, the epicardial surface points were assigned a color based on the color code previously decided in Table 2-1. The points and their associated color are directly projected onto the map. The surface models used are the ones deformed by the optimal transformation found with the registration procedure previously described. Texture mapping from 3D to 2D is done by projecting the geodesic model of the LV, *S*, whose shape resembles roughly a spheroid, onto a 2D disk *D* (see Figure 2.6). Coordinates of the model are expressed as spherical coordinates $S(\phi, \theta)$, where ϕ indicates the elevation of the point in the LV and θ is the angle in the short axis slice such as schematically presented in Figure 2.6 (a). The coordinates of the disk are described with polar coordinates $D(r, \theta)$, where r is the length of the ray from the center of the disk and θ is the angle. Those angles are calculated over a reference frame found with the PCA algorithm as applied to the model points with the principal axis aligned with the long axis of the LV. Transformation is found by:

$$\phi : \left[-\frac{\pi}{2}, \frac{\pi}{2} \right] \rightarrow r : [0,1] \qquad 2\text{-}10$$

Each concentric ring of the disk therefore corresponds to a level of the LV from apex (center of the disk) to base (outermost ring of the disk) (see Figure 2.7). The mitral valve is omitted in the viability map by projecting nodes of the LV geodesic model that have an angle ϕ smaller than $\frac{3\pi}{8}$ such as represented in Figure 2.6 (b).

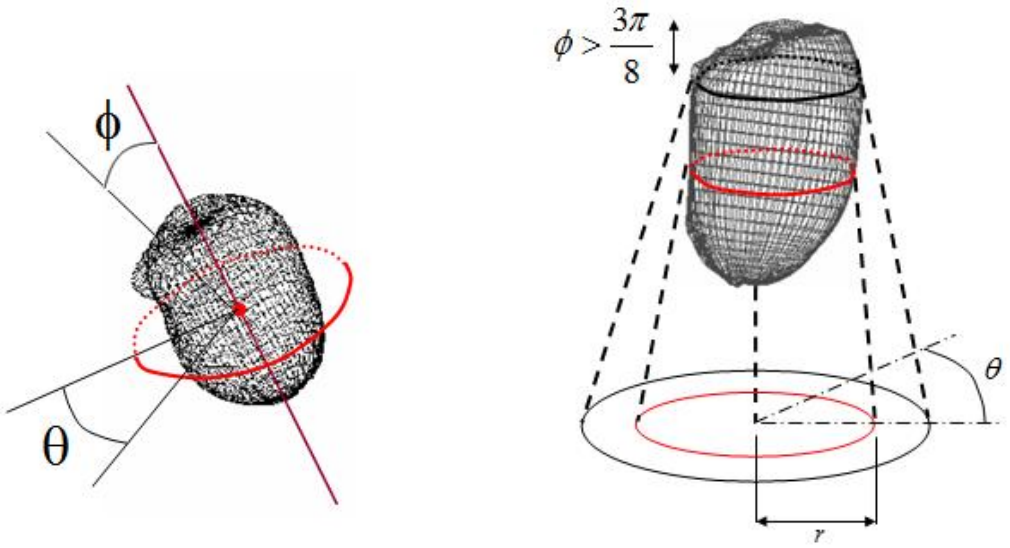

(a) (b)

Figure 2.6 : LV surface model and schematic representation of spherical coordinates calculated for each of the surface points (a) and polar projection from 3D to the 2D map.

This type projection does not maintain area on the projected plane and distortion increases as projection evolves away from the central point of projection. Overwriting of projected values is therefore possible. This does not cause problems in the case of coronary territories projection. However overwriting of projected values is problematic for viability information since it is directly related to the intensity found in the DEMR

sequence of images. Bright areas are considered to be dead tissues since dead cells are hypothesized to have a slower wash out rate than healthier ones. It is possible that a 3D bright intensity value might be overwritten by projection of a darker 3D position in DEMR and this could prevent the clinician from identifying dead cardiac cells on the resulting map. In this context, bright intensities have priority over darker ones and were kept in case overwriting of intensities occurred.

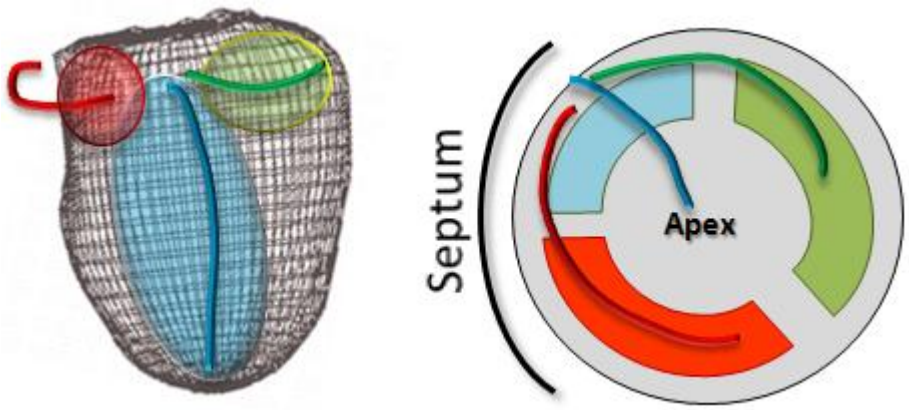

Figure 2.7: Projection of the 3D geodesic model of the LV onto a 2D disk in order to create the viability map. The outer ring of the map to the right corresponds to the basal area of the LV, projection of the LCX territory (in green) is expected to lie to the upper right side of the model, and the RCA (in red) is expected to occupy the lower left area of the map.

Structural and functional information are projected over the circular map. Following the registration of DEMR and CTA images orientation of the model is kept consistent with the same mapping procedure. Both surface models have different resolution directly related to the quality of the imaging modality. Therefore projection of territories

computer in CTA are presented on the circular map with a higher resolution than the projection of viability found in DEMR.

The combined map has approximately the same orientation with respect to the 17-segment model. The septum is projected onto the left hand side of the map. The birth place of coronary arteries, although out of the limit of the viability map, lies approximately to the upper left side of the disk. The LAD starts from that point and generally spreads to the center of the map which represents the apex and might spread slightly beyond that point, since this coronary does loop around the tip of the heart in some cases. The RCA wraps around the right ventricle and should appear in the same side as the septum on the map. The LCX, that wraps around the base of the heart and possibly descends towards the apex at its tip, should be positioned to the right of the map, close to the outermost ring (see Figure 2.7).

Validation

For patients with an available X-ray angiograms, ground truth may be obtained via the Green Lane method. Available coronary angiograms were performed clinically in each patient and always within one month of the CTA acquisition, with no interval surgical intervention such as coronary bypass. In this method, an experienced cardiac radiologist manually transcribes the coronary tree, with branch vessels, from a coronary angiogram onto a bull's eye plot. This plot is then manually divided into coronary distribution regions based on these projections (see Figure 2.8). A percent correlation is used to quantify correspondence of area of a coronary territory. Two models are aligned and, for a given coronary, the area of overlap is divided by the total area and multiplied by 100%.

Any deviation that results from our method and from the population based 17-segment model can be evaluated when both models are compared to The Green Lane map.

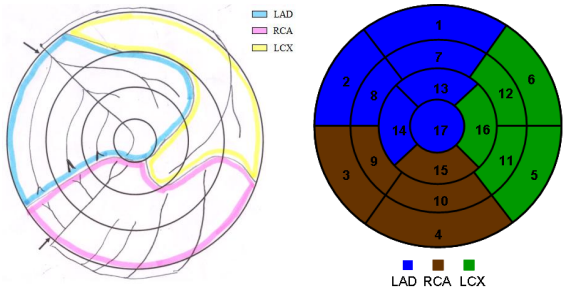

Figure 2.8: An example of result for the Green Lane method (LAD blue, LCX yellow and RCA pink) (to the left) compared to the 17-segment model (LAD blue, LCX green, RCA brown) (to the right).

CHAPITRE 3 RESULTS

Creating augmented viability maps with coronary structure requires the extraction, combination and projection of information from medical heart images onto the desired final diagnostic tool: a patient specific 2D map encapsulating functional and structural information. This section presents the results obtained through the various steps of the map creation and serves as validation for each step of the method. The coronary territories are presented in section 3.1. Registration results are presented in section 3.2 and quantification of viability is described in section 3.3. The augmented viability maps are presented in section 3.4.

3.1 Coronary territories

For each patient we compute the coronary territories over the surface of the myocardium in three dimensions. These territories are projected onto a 2D map and can be depicted in color coded regions or only drawn as borders. For each case the volume and geodesic surface models are shown as well as the color coded coronaries. The territories are then pictured in 3D and over a circular map.

Patient 1

The CTA volume for the first patient is shown in Figure 3.1. The upper right visualization window in this figure is the 3D rendered view of the whole CTA where the white axes are the principal directions found with PCA. The upper left visualization window presents the short axis multi-planar reconstruction (MPR) view and the MPR

plane appears in other windows as a blue axis. The two lower windows show the anterior and head MPRs, identified respectively by the green and red axes. The pre-segmented LV surface models obtained from the method described in [183] is also visible in Figure 3.1. The endocardium model is rendered as interconnected points in green in Figure 3.2 and composed of 2016 points, the same number as for the epicardial model.

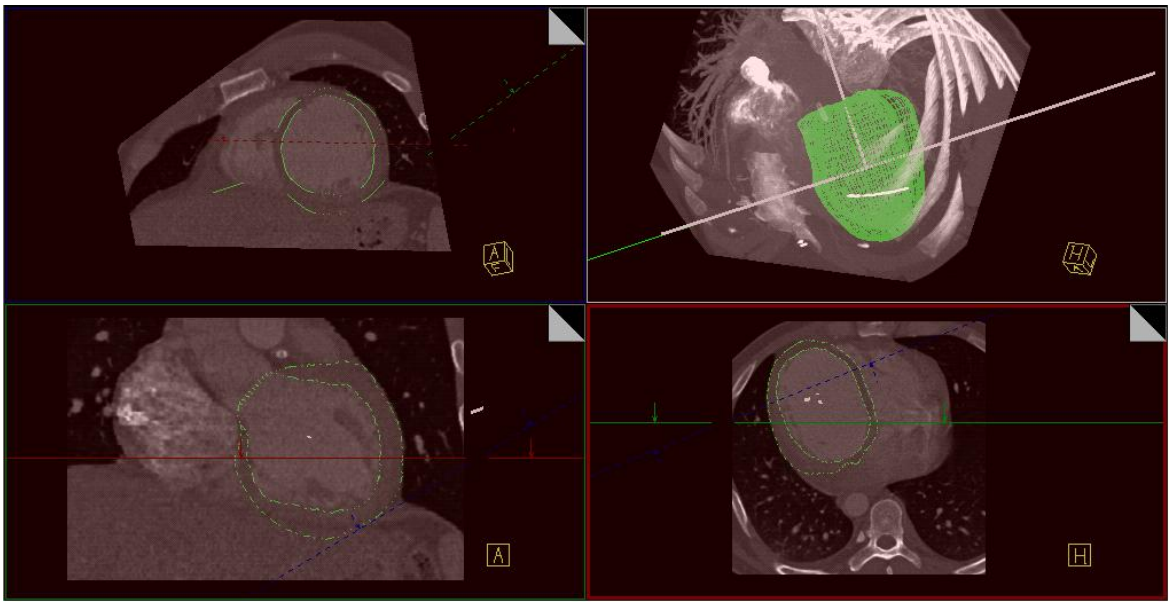

Figure 3.1: The CTA volume for Patient 1 with the geodesic model of the LV in green. The white lines describe a coordinate system for the left ventricle.

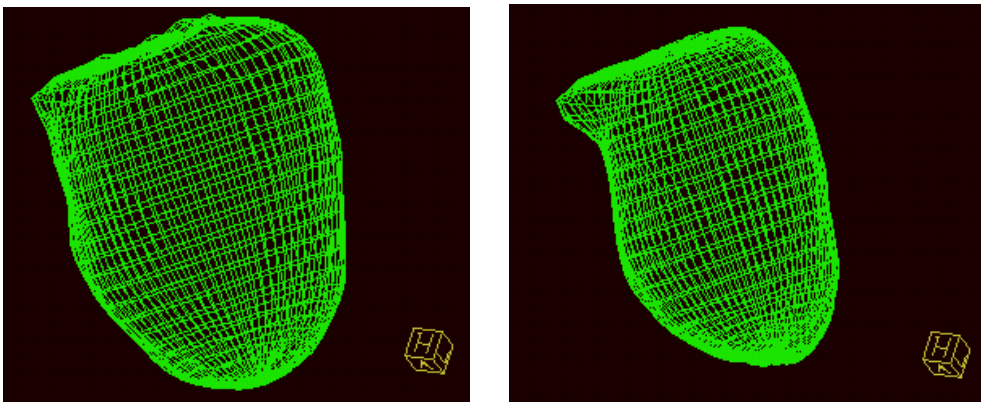

(a) (b)

Figure 3.2: Epicardium (a) and endocardium (b) models of the LV identified in the CTA for Patient 1.

Coronary paths are described by an interpolation of series of points whose position were chosen by an experienced physician examining CTA data. Each point is assigned to a coronary and given a color according to the color code presented in Table 2-1. The paths of the coronaries given for patient 1 are shown, color coded, inside the CTA volume in Figure 3.3. A stent is visible for this patient at the start of the LAD (black arrow in the image). They are again shown in Figure 3.4 and over the epicardial geodesic model with a three coronary group classification. The clinician provided us with an alternate classification with a branch off the LAD shown in Figure 3.5, therefore creating a fourth coronary group in the classification.

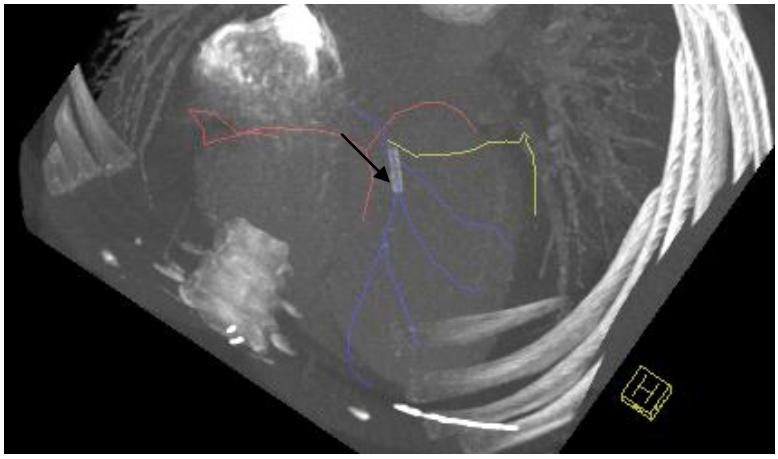

Figure 3.3: Color coded coronary points delineated by a physician seen over a volume rendered view of CTA. A coronary stent is visible (black arrow) close to the base of the heart in the LAD.

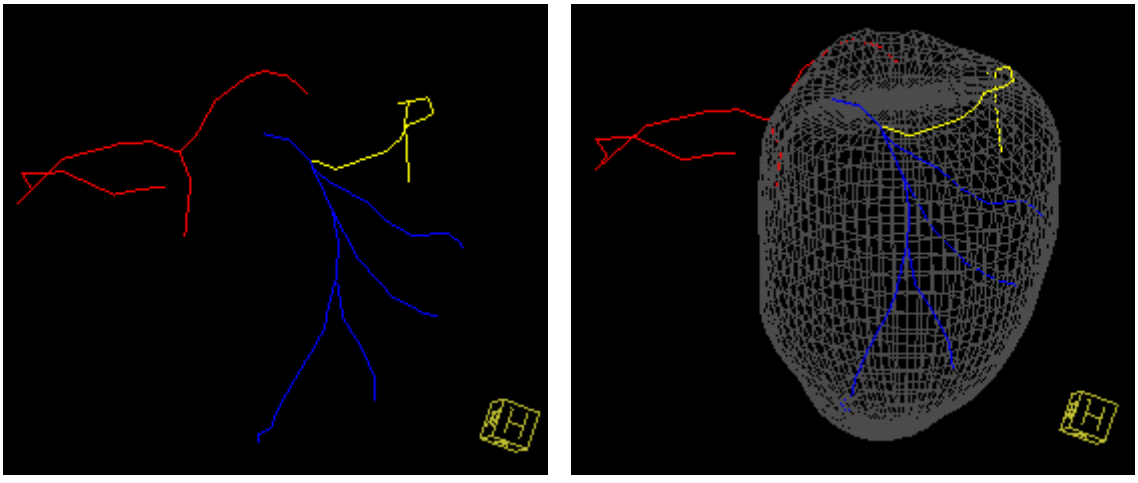

(a) (b)

Figure 3.4: Color coded coronaries for patient 1 in 3D (a) and over the geodesic model of the epicardium (b).

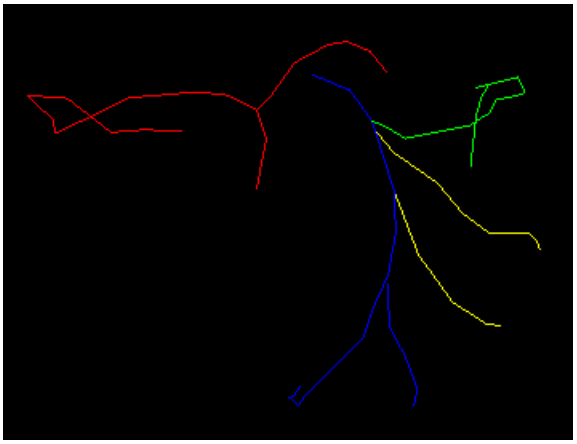

Figure 3.5: Color coded coronaries in 3D with a four group classification (yellow is for branch vessel off from the LAD).

After minor adjustments for the RCA segmentation in the septum area, the computed territories using our method are shown in 3D an on a 2D map in Figure 3.6. The LAD for this patient reaches the apex and wrap slightly around towards the posterior of the LV. This is visible in the coronary territories in 2D in Figure 3.6 as shown by the black arrow. For this patient, the clinician provided us with a fourth group for coronary classification (branches off the LAD). This particular case is shown in Figure 3.7. The fourth territory only spreads over the LV surface previously associated with the LAD, from the base (close to the left main coronary) to a position close to the apex however not reaching it.

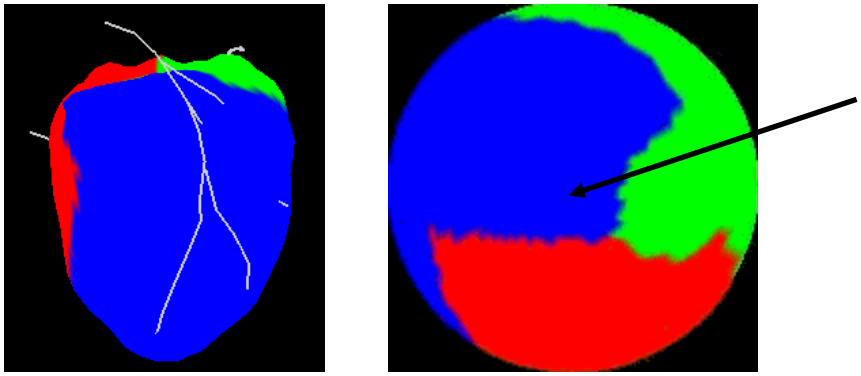

(a) (b)

Figure 3.6: Result of automatic computation of coronary territories for patient 4 with 3 group classification: LAD (blue), LCX (green), RCA (red) in 3D with coronary segmentation (a) and in 2D map (b). The black arrow points the apex.

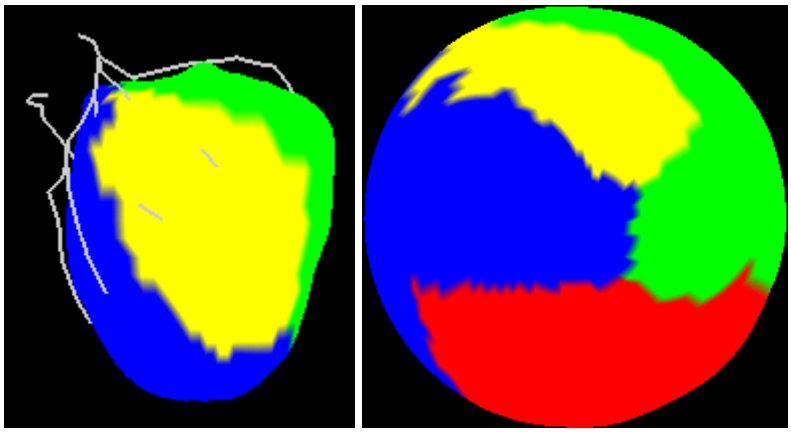

(a) (b)

Figure 3.7: Coronary territories for patient 1 with a 4 group classification: LAD (blue), RCA (brown), LCX (green) and a branch off the LAD (yellow) in 3D (a) and on a 2D territory map (b).

Patient 2

The available CTA volume, LV model, and coronary segmentation are presented in Figure 3.8 and Figure 3.9 for Patient 2. The territories computed by our method are shown in the polar projection in Figure 3.10 next to the Green Lane result. In our computed territory model, the apex is covered by the LAD as shown by the territory colored in blue. There is a variation from the result of the Green Lane method: the right coronary artery stops shorter in our model and does not seem to feed the inferolateral surface of the LV (the yellow arrow in Figure 3.10).

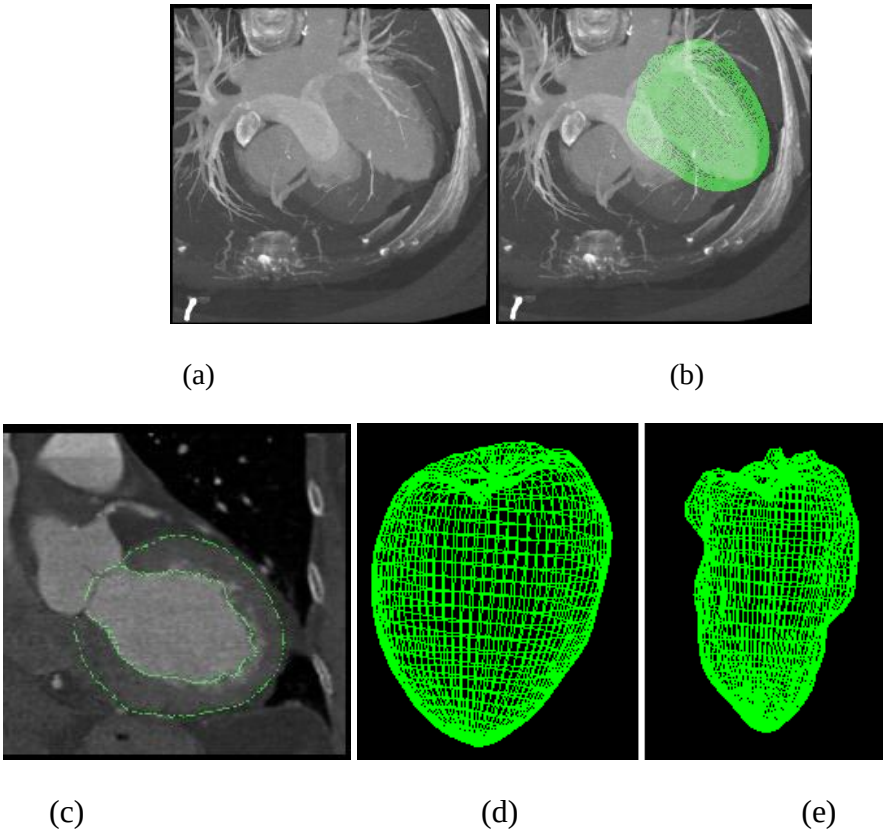

(a) (b)

(c) (d) (e)

Figure 3.8: CTA volume of Patient 2 (a), with LV segmentation (b-c). LV segmentation model: epicardium (d) and endocardium (e).

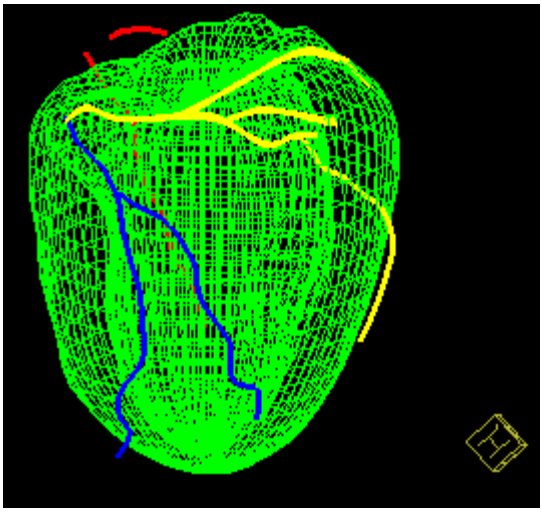

Figure 3.9: Color coded coronaries for Patient 2, with 3 coronaries: LAD (blue), LCX (yellow) and RCA (red).

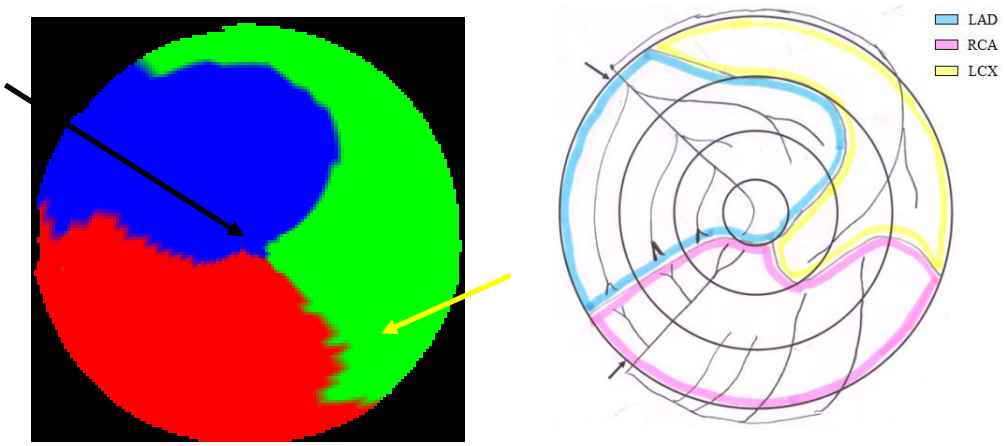

Figure 3.10: Result of the automatic computation of coronary territories for Patient 2 (to the left) and territory map following the Green Lane method.The black arrow points to the apex. The yellow arrow points to a variation with regards to the Green Lane model.

Patient 3

The available CTA volume, LV model, and coronary segmentation are presented in Figure 3.11 and Figure 3.12 for Patient 3. The Green Lane result is compared to the 17-segment model in Figure 3.13. The computed territories by our method are shown in 3D along with the polar projection in Figure 3.14. The computed LAD territory spreads towards the inferolateral surface of the LV however the clinician found it was rather oriented towards the inferoseptal surface of the LV.

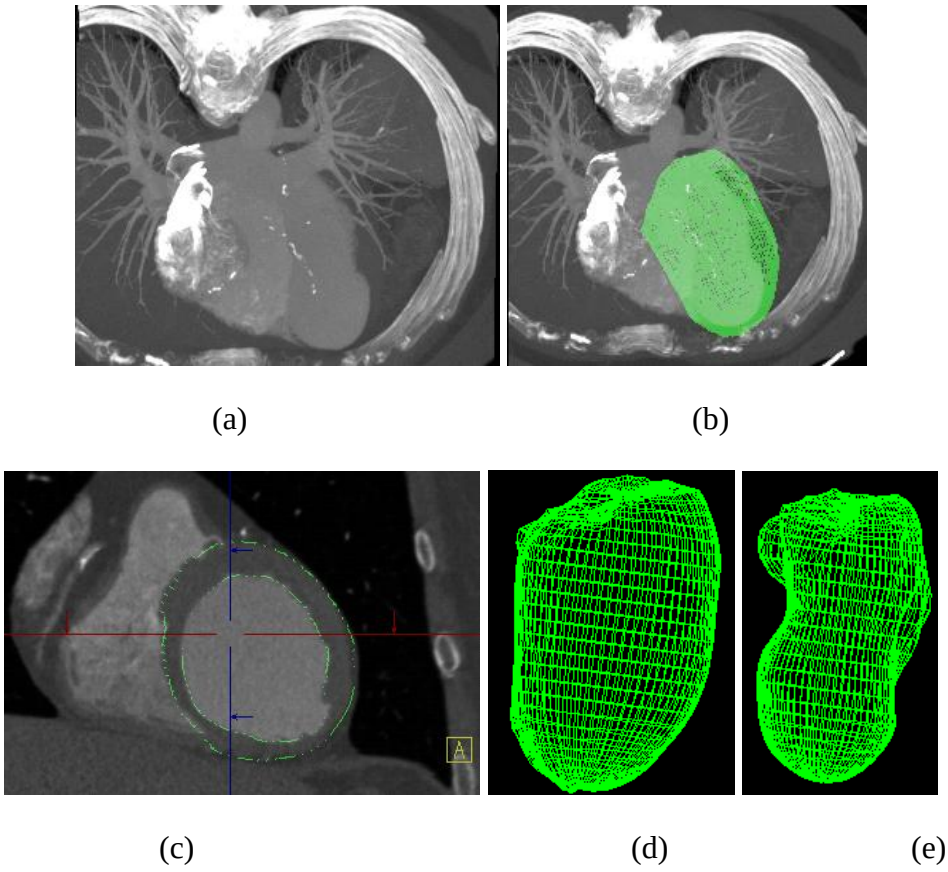

(a) (b)

(c) (d) (e)

Figure 3.11: CTA volume of patient 3 (a), with LV segmentation (b-c). LV segmentation model: epicardium (d) and endocardium (e).

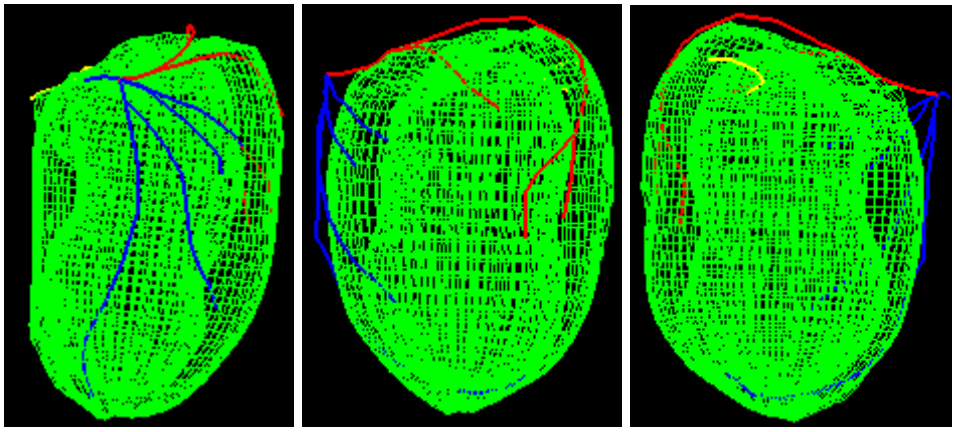

Figure 3.12: Color coded coronaries for Patient 3, with 3 coronaries: LAD (blue), LCX (yellow) and RCA (red).

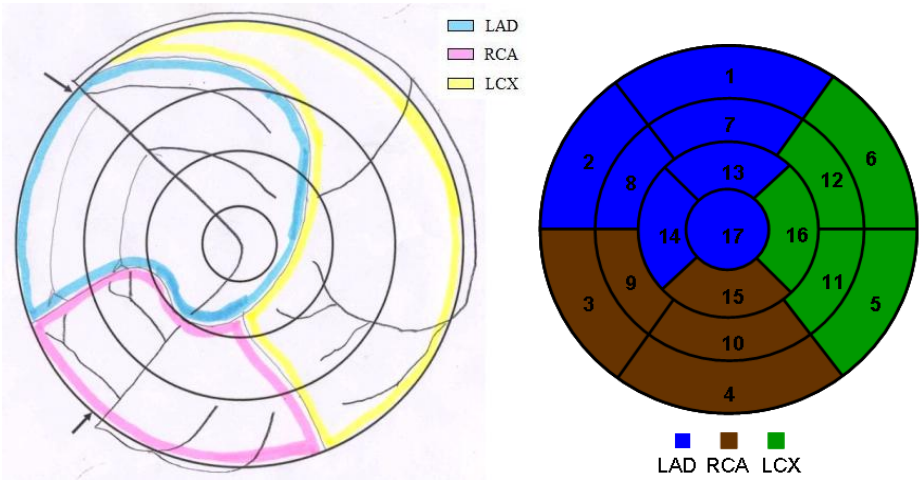

Figure 3.13: Color coded coronaries for patient 3, with 3 coronaries: LAD (blue), LCX (yellow) and RCA (red).

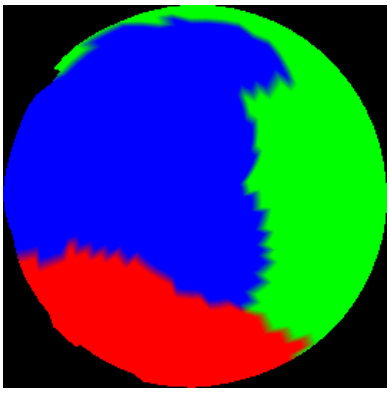

Figure 3.14: Result of automatic computation of coronary territories for patient 3 with previous method.

Patient 4

The available CTA volume, LV model, and coronary segmentation are presented in Figure 3.15 and Figure 3.16 for Patient 4. The computed territories by our method are shown in 3D in Figure 3.17. For this patient, the Green Lane method was available. A comparison of our method, the Green Lane and the 17-segment model is shown in Figure 3.18.

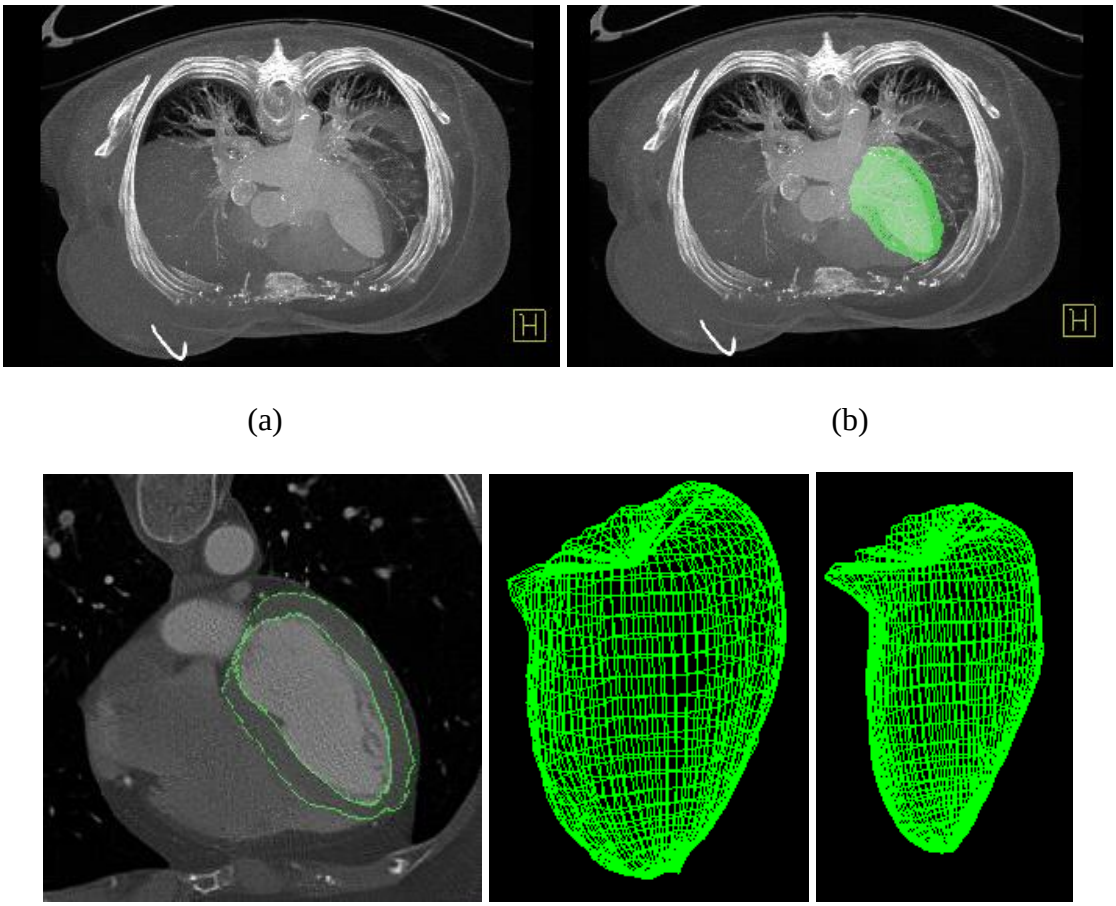

(a) (b)

(c) (d) (e)

Figure 3.15: CTA volume of Patient 4 (a), with LV segmentation (b-c). LV segmentation model: epicardium (d) and endocardium (e).

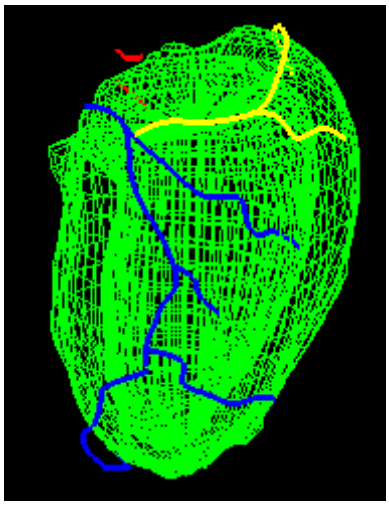

Figure 3.16: Color coded coronaries: LAD (blue), LCX (yellow) and RCA (red) over LV model extracted from CTA (green) for Patient 4.

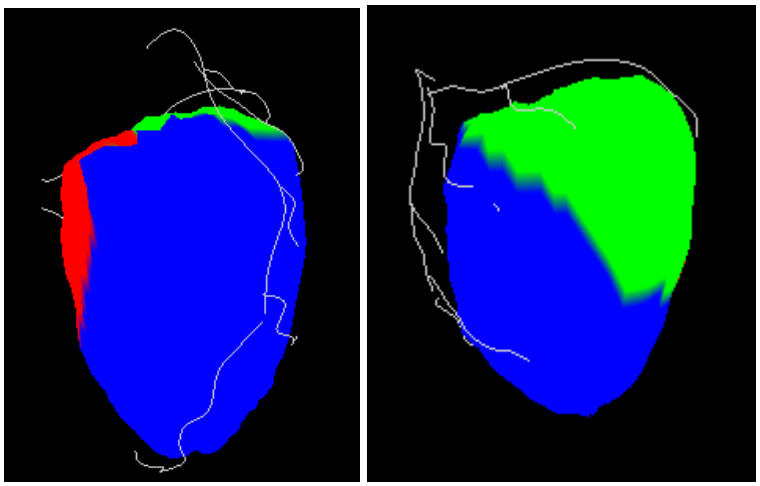

Figure 3.17: Color coded coronary territories for patient 4 over LV model from CTA, with 3 coronaries: LAD (blue), LCX (green) and RCA (red).

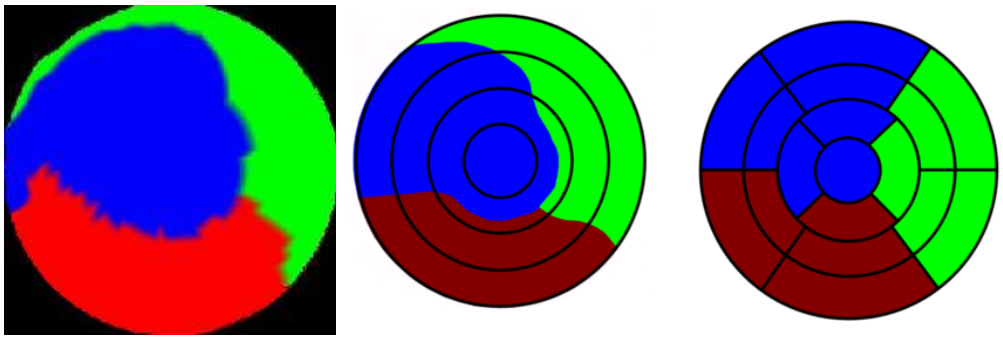

(a) (b) (c)

Figure 3.18: Comparison of our CT-derived model for patient 4 (a) with the Green Lane (b) and the 17-segment model (c). The black concentric lines drawn in figure (b) have been placed for comparison purposes.

Validation

The Green Lane method provided the ground truth for a comparison with our method as well as for a comparison with the 17-Segment model. The 17-segment model comparison resulted in a correlation of 79%. Table 3-1 presents the comparison on a per patient basis of our technique versus the ground truth opposed to the 17-Segment model versus the ground truth. In each case, the area of overlap for a territory is divided by the total area and multiplied by 100%. When our models were compared with the ground truth we had a correlation of 95% for Patient 1, 83% for Patient 2, 87% for Patient 3 and 84% for Patient 4 (see). Overall, the average percent correlation between our CTA-derived maps and the ground truth was 87%. Results indicate the percentage of myocardial pixels which agree between the techniques.

Table 3-1: Comparison as a percentage of correspondence of our computed coronary territory maps and the 17-Segment model to the map obtained with the Green Lane method as the ground truth.

	Computed vs. Ground Truth	17-segment vs. Ground Truth
Patient 1	95.28	79.1
Patient 2	83.14	73
Patient 3	87.17	81.7
Patient 4	84.8	81.4
Average	87.59	78.8

3.2 3D Registration

Registration of DEMR and CTA is necessary to obtain correspondence between the projected coronary territories map and the viability map. Results after each step of our method will be displayed only for patient 1. Initialization result with PCA is first shown and will be followed by the results of the thin plate spline deformation of the model. The final registrations for each patient are then shown as determined by MI.

3.2.1 Registration based on Principal Components

The registration result based on alignment of the principle component axes of the functional and structural model for patient 1 is shown in Figure 3.19, where the white

axes represent the principal component directions. The first principal component represents the vertical axis and traverses the longitudinal direction of the heart. The second and third modes found by PCA are horizontal in Figure 3.19 and tend to lie close to the short axis plane. This process can only serve as an initialization for a refined registration algorithm since there is no point correspondence for the geodesic models of both modalities and they are rotationally underconstrained: the RV identified in DEMR is clearly not aligned with the RV in the CTA volume (see Figure 3.19 (b) and Figure 3.20).

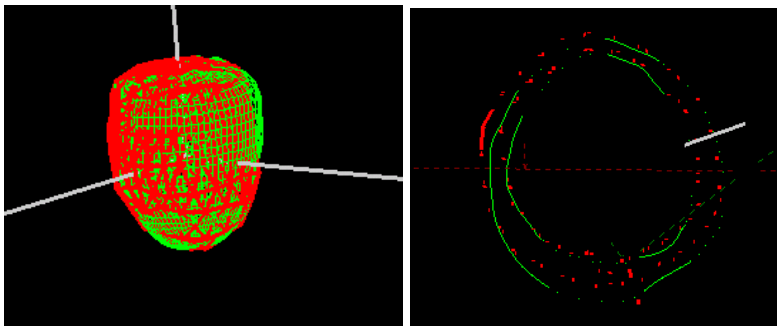

(a) (b)

Figure 3.19: Geodesic models of DEMR and CTA after PCA registration for Patient 1 in 3D (a) and in a short axis view (b).

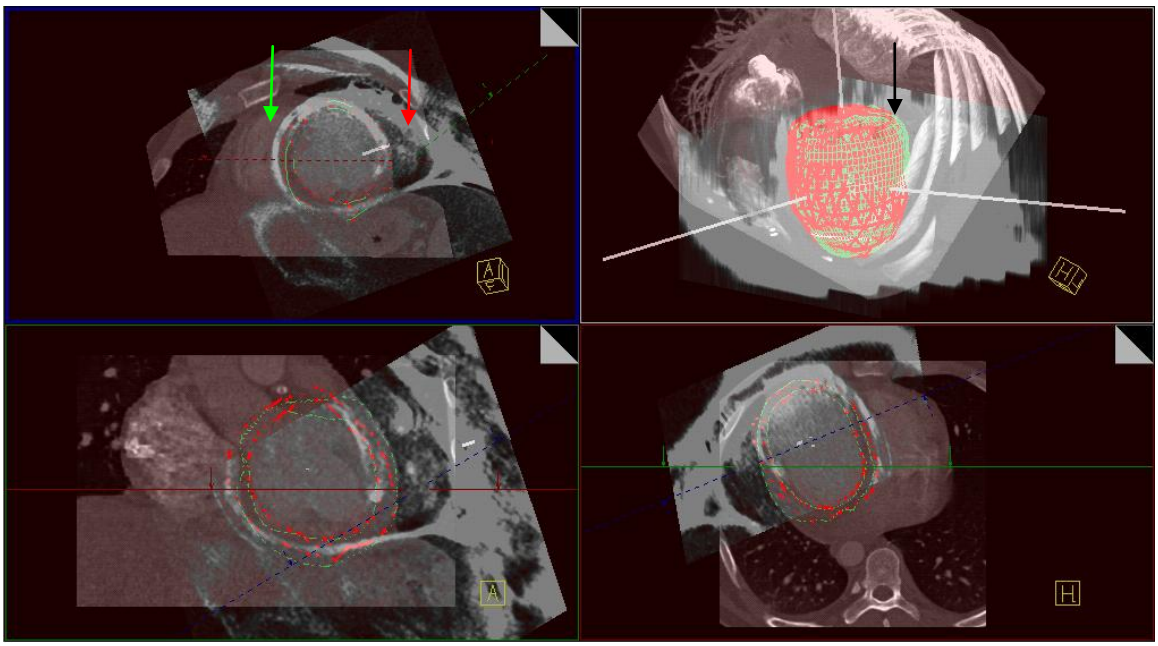

Figure 3.20: Result of registration initialization using principal components for Patient 1. The black arrow seen in the rendered volume view indicates the location of misalignment of LV surface points from DEMR and CTA. The top left view shows the difference in orientation noticeable with the orientation of the RV in DEMR (red arrow) and CTA (green arrow).

3.2.2 Thin Plate Spline-based Registration

Figure 3.21 shows results for Patient 1. In this image, the green mesh is the segmentation model found in the CTA volume and the red mesh is the DEMR model after deformation following a TPS deformation. Both models are successfully matched to a common shape (these results will show the CTA image volume only for clarity of presentation).

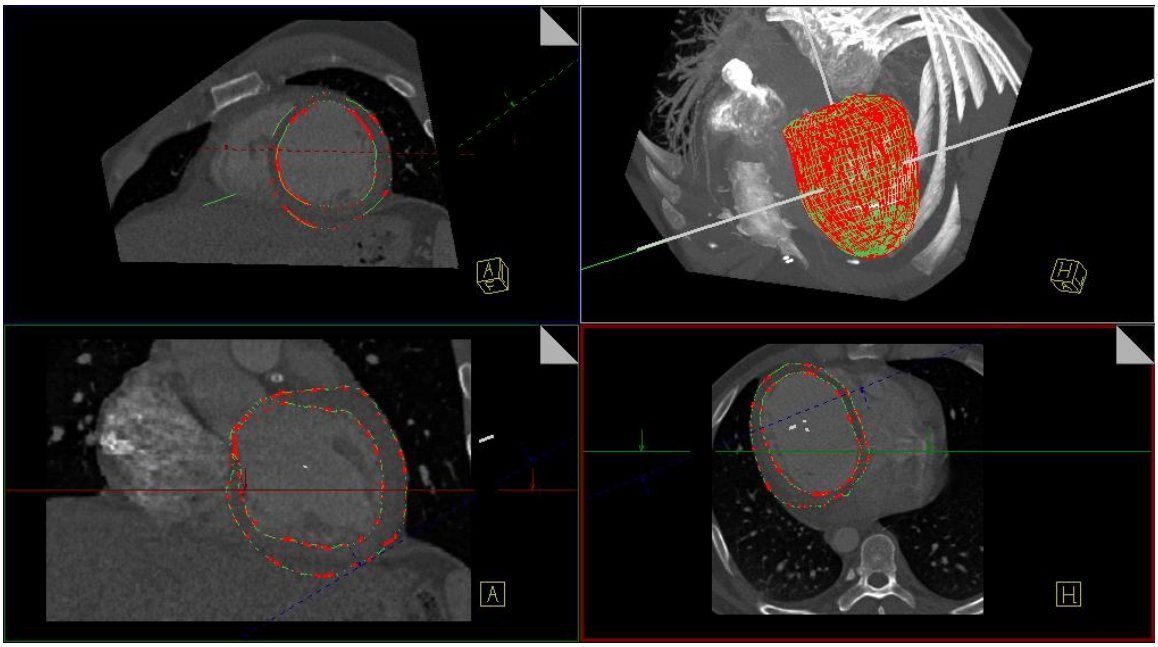

Figure 3.21: Geodesic models after TPS algorithm for patient 1. Only CTA volume is shown for clarity of presentation.

3.2.3 Mutual information and final registration results

The results of registration via maximizing mutual information is given as a series of rotation angles around the left ventricle center (as determined by the PCA algorithm). The rotation angles are ϕ_{SAN}, which describes the inclination of the principal axes of the model found in DEMR image, and θ_{SAN} refers to the rotation angle of the moving image in the short axis plane.

Patient 1

The pose of CTA volume and slices of DEMR after initial registration via PCA for Patient 1 is shown in Figure 3.22. Registration result following our method for this

patient is shown individually and in correspondence in Figure 3.23. Since the insertion points of the right ventricle stand as reference for registration, it is clear that registration is close after PCA. However the overlay of the right ventricles in the two volumes is more precisely aligned after our method. The filter applied to DEMR images was composed of a step of 0.1, an alpha factor of 1 and a proportion of shock/diffusion of 1 (therefore applying only diffusion). The numerical values for the registration are found in Table 3-2. The highest value (1.00187) indicates an optimal rotation of -30 degrees of DEMR images around the SAN, itself tilted of 7 degrees with regards to its original direction.

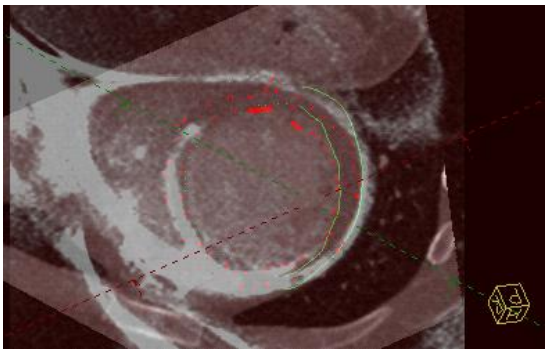

(a)

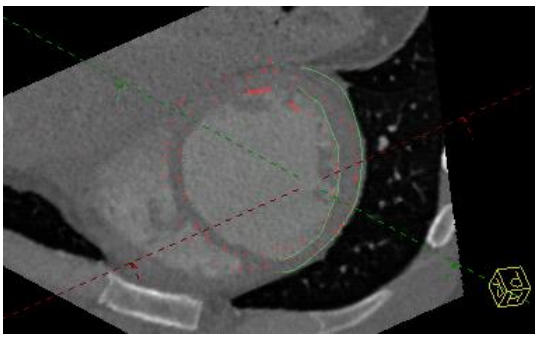

(b)

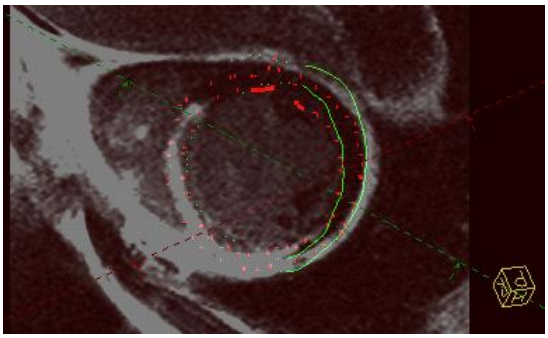

(c)

Figure 3.22: DEMR and CTA volume for Patient 1 before registration.

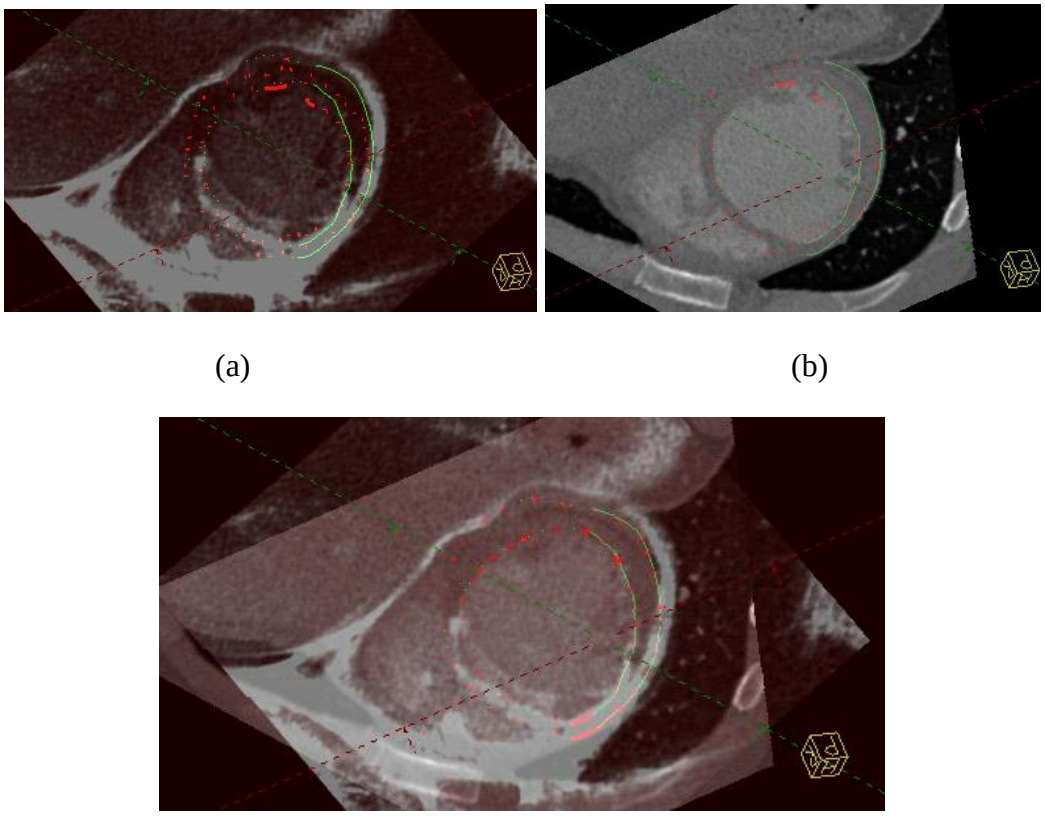

(a) (b)

(c)

Figure 3.23: Registration result for Patient 1. DEMR images (a), CTA volume (b) and overlay of both in the short axis view (c).

Table 3-2: Numerical results after mutual information registration for Patient 1.

Short axis normal (SAN) rotation		**Rotation of MR around SAN**	**Mutual information value**
θ_{SAN}	ϕ_{SAN}	θ	
0	7	-60	1.00178
0	7	-50	1.00184
0	7	-40	1.00178
0	7	-30	**1.00187**
0	7	-20	1.00154
0	7	-10	1.00142

Patient 3

Mutual information values are presented in Table 3-3 and the registration results are showin in Figure 3.24. The highest value after mutual information (1.002157) as found in Table 3-3 indicates an optimal rotation of -5 degrees of DEMR images around the SAN tilted of -5 degrees with regards to its original direction. There is a slight offset for this patient and the alignment is not exact. This can be noticed by analyzing the limit of the lung region in Figure 3.24. Nevertheless the RV aligns correctly. The filter applied to the DEMR images of this patient was composed of a step of 0.5, and alpha factor of 0.8 and a portion of shock/diffusion of 1.

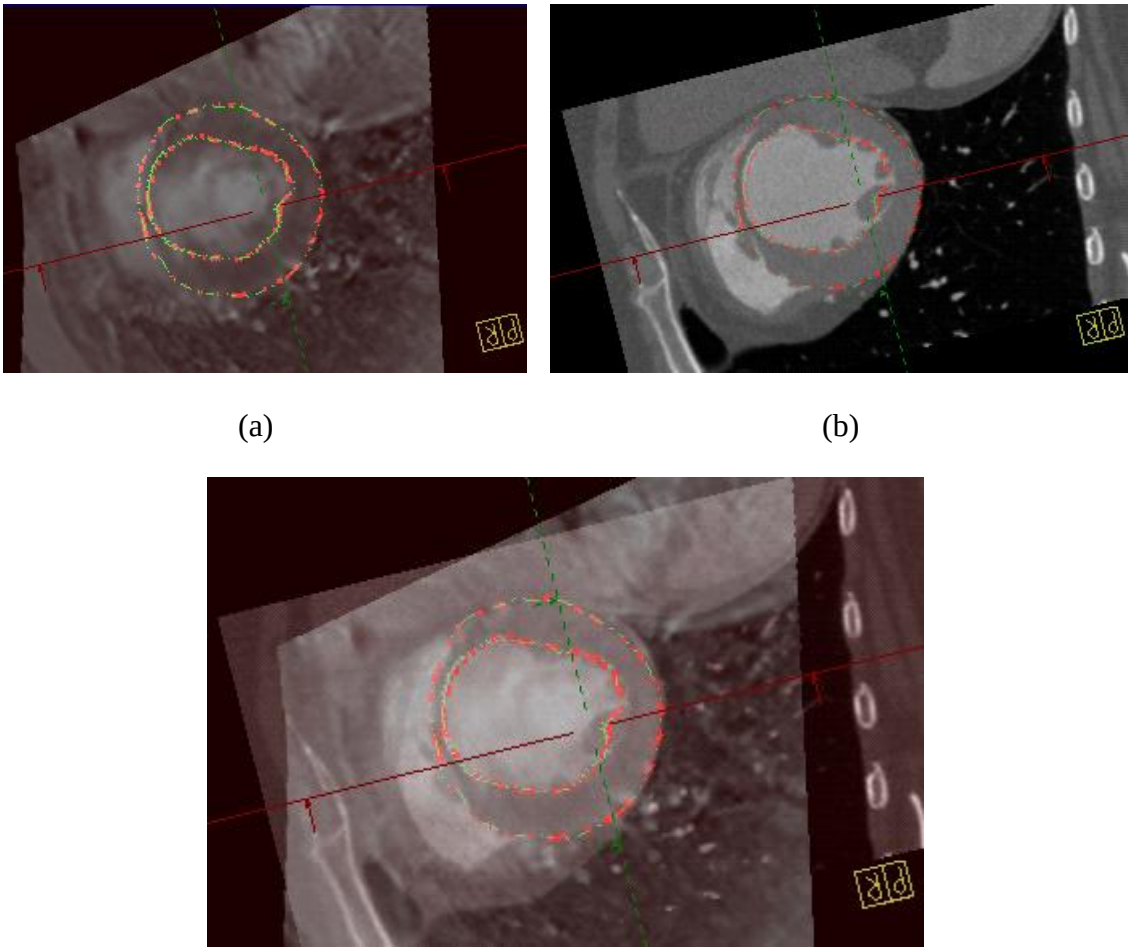

(a) (b)

(c)

Figure 3.24 : Registration result for Patient 3: DEMR (a), CTA (b) and both (c).

Table 3-3: Numerical results after mutual information registration for Patient 3.

Short axis normal (SAN) rotation		**Rotation of MR around SAN**	**Mutual information value**
θ_{SAN}	ϕ_{SAN}	θ	
0	-10	-10	1.001314
0	-10	-5	1.001280
0	-10	0	1.001717
0	-10	5	1.001607
0	-5	-10	1.001281
0	-5	-5	**1.002157**
0	-5	0	1.001700
0	-5	5	1.001919
0	-5	10	1.001826

Patient 5

Before registration the RV found in DEMR and CTA are clearly not aligned as can be seen in Figure 3.25. The registration results for our method are shown for Patient 5 in Figure 3.26 where the CTA volume and slices of DEMR are shown individually and in correspondence. There is good match in the orientation of the right ventricle in the short axis view in the registration. However since the deformation algorithm is focused on the

heart, no exact matching can be observed. This statement is valid for surrounding organs to the left ventricle, for example for the rib cage that is visible in the lower right portion of the images. Numerical values for this patient are presented in Table 3-4. The filter applied to DEMR images was composed of a step of 0.1, an alpha factor of 1 and a proportion of shock/diffusion of 1 (therefore applying only diffusion). The highest value after mutual information (1.01661) as found in Table 3-4 indicates an optimal rotation of -130 degrees of DEMR images around the SAN tilted of 10 degrees with regards to its original direction.

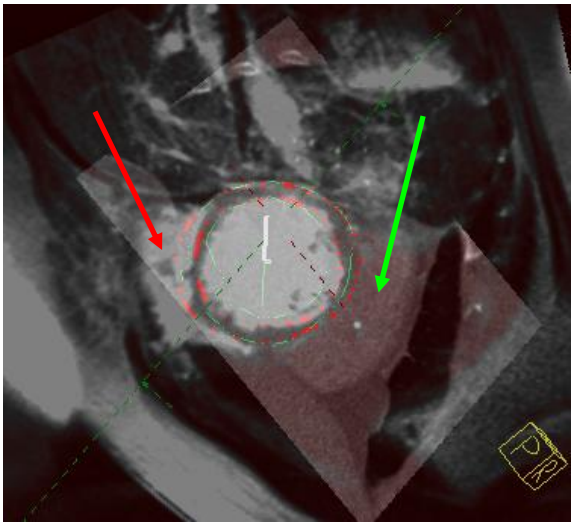

Figure 3.25 : DEMR and CT for Patient 5 before registration. Arrows indicate position of the RV in DEMR (red) and CT images (green).

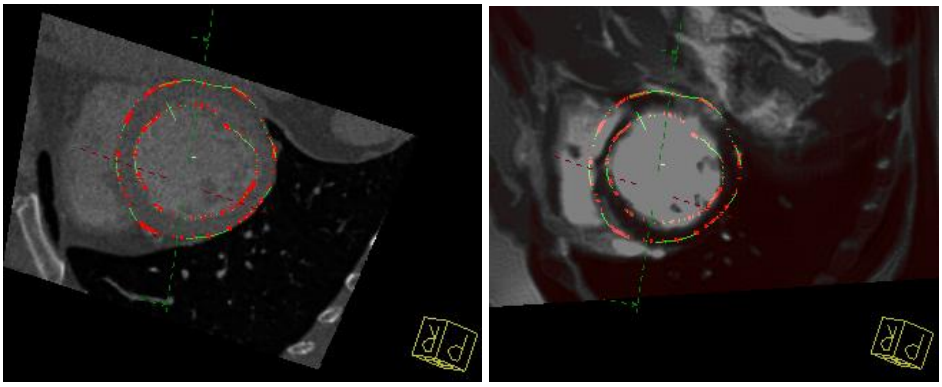

(b) (c)

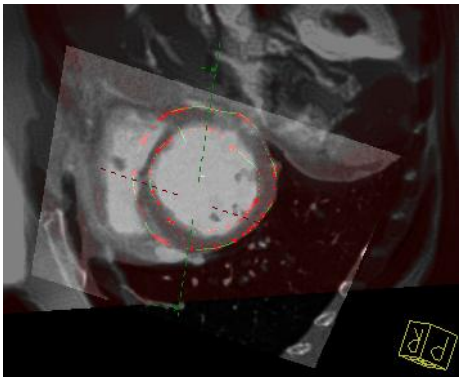

(d)

Figure 3.26: Registration result for Patient 5 showing orientation of CTA volume (a), DEMR slice (b) and the actual correspondence of the two (c).

Table 3-4 : Numerical results after mutual information registration for Patient 5.

Short axis normal (SAN) rotation		**Rotation of MR around SAN**	**Mutual information value**
θ_{SAN}	ϕ_{SAN}	θ	
0	10	-160	1.01485
0	10	-150	1.01555
0	10	-140	1.01468
0	10	-130	**1.01661**
0	10	-120	1.01609
0	10	-110	1.0157

Patient 6

Orientation of volumes for Patient 6 before registration can be observed in Figure 3.27. The right ventricle seen in the DEMR images (Figure 3.27 a) is slightly off when compared to that of the CTA volume (Figure 3.27 b). Moreover we can rely on the lungs (dark regions) for orientation with this patient. The upper limit of the lung reaches higher in the images for CTA volume than in the DEMR images as indicated with arrows in Figure 3.27 (c). The final registration result is presented in Figure 3.28. The numerical values associated with the results are presented in Table 3-5. The filter was not applied for this patient. The highest value (1.0118) indicates an optimal rotation of -35 degrees of DEMR images around the SAN tilted of -3 degrees and rotated of -10 degrees around its original direction.

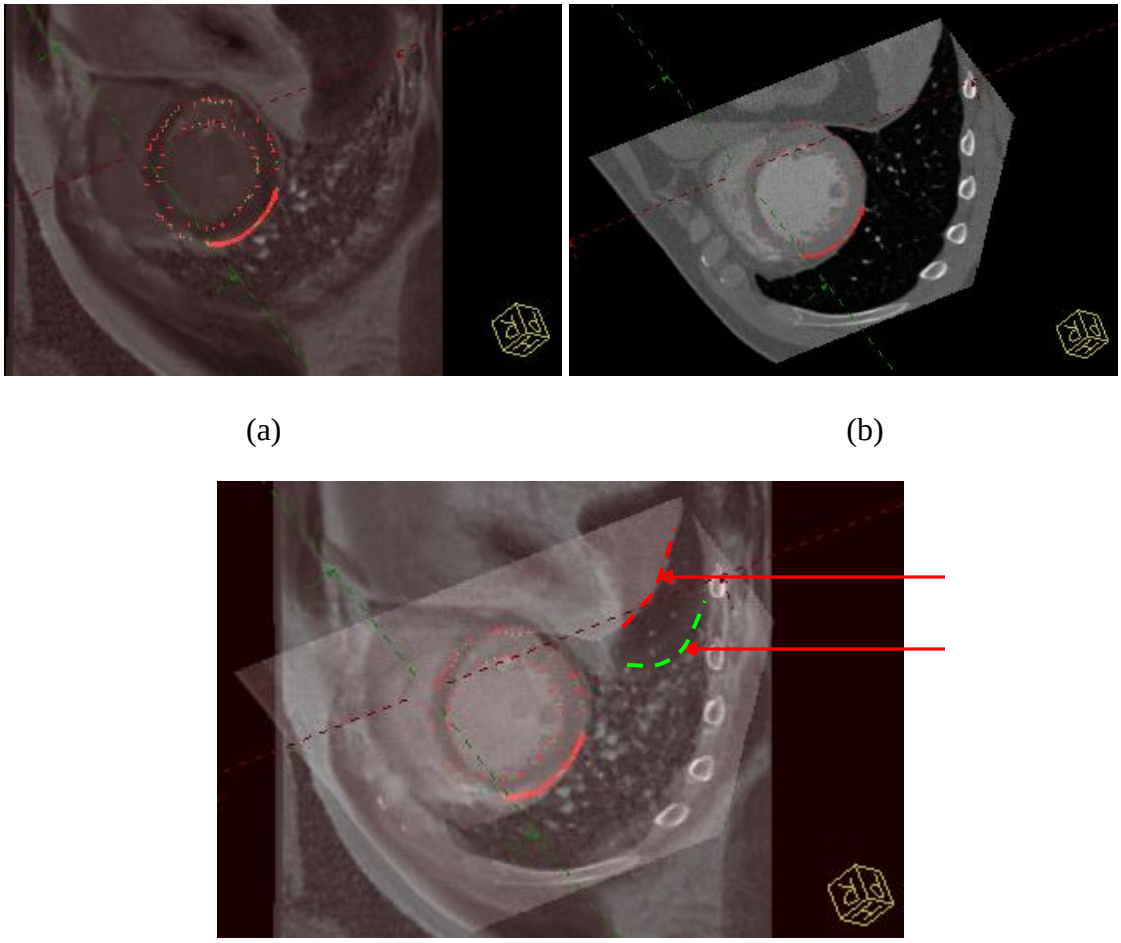

(a) (b)

(c)

Figure 3.27: Orientation of images for Patient 6 after principal component analysis and before registration with thin plate spline and mutual information; DEMR (a), CTA (b) and overlay of both images in the short axis view (c). Arrows in (c) indicate the end of lung region in CTA (dashed red line) and DEMR (dashed green line).

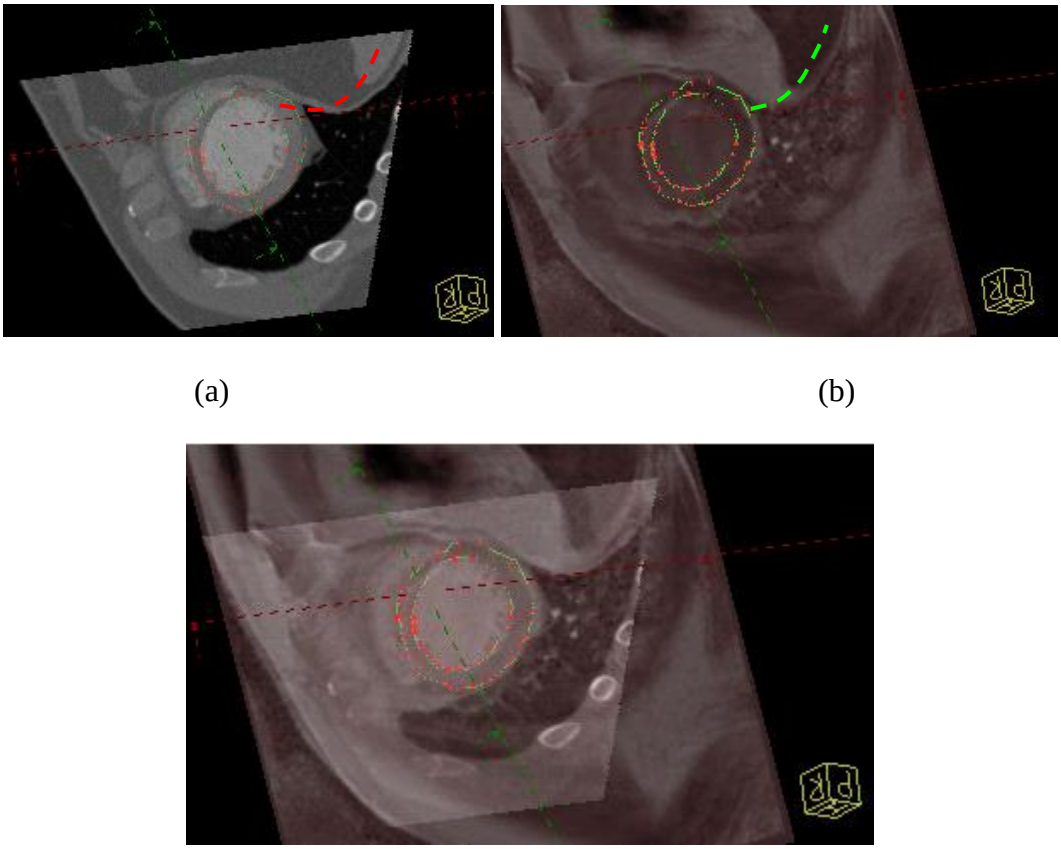

(a) (b)

(c)

Figure 3.28: Final registration result for Patient 6; CTA (a), DEMR (b) and overlay of both images in the short axis view (c). Dashed lines in (a) and (b) indicate the end of the lung region in CTA (dashed red line) and in DEMR (dashed green line) images.

Table 3-5 : Numerical values after mutual information registration for Patient 6.

Short axis normal rotation		**Rotation of MR around SAN**	**Mutual information value**
θ_{SAN}	ϕ_{SAN}	θ	
-10	-3	-55.00	1.01058
-10	-3	-45.00	1.01039
-10	-3	-35.00	**1.0118**
-10	-3	-25.00	1.01087
-10	-3	-15.00	1.01163
-10	-3	-5.00	1.01106

3.3 Myocardial Function from DEMR

For each patient, quantification of myocardial function is done by evaluating the transmural extent of scar between the epicardium and the endocardium of the heart in DEMR images. The rendered DEMR volume is shown as well as the surface model for the epicardium and endocardium. An average of intensities is calculated and shown in 3D as well as after projection on a circular map.

Patient 1

The DEMR images available for Patient 1 are presented in Figure 3.29 where it is possible to see the overlaid 3D geodesic model in red. Figure 3.30 shows the DEMR volume and LV model more precisely in different views. The geodesic models were obtained automatically in the DEMR images with a segmentation method described in [182] and were corrected manually to fit to borders with a software tool developed at Siemens Corporate Research. The epicardial model is composed of 258 points, similarly for the endocardium model and shown in Figure 3.31. A spherical coordinate system was determined as describedin section 2.4 and result of the viability projection is presented in Figure 3.32. This patient has 100% blockage of the LAD, with no significant stenosis of the LCX and 70% blockage of the RCA, reflected in the bright regions in the upper left region of the viability map.

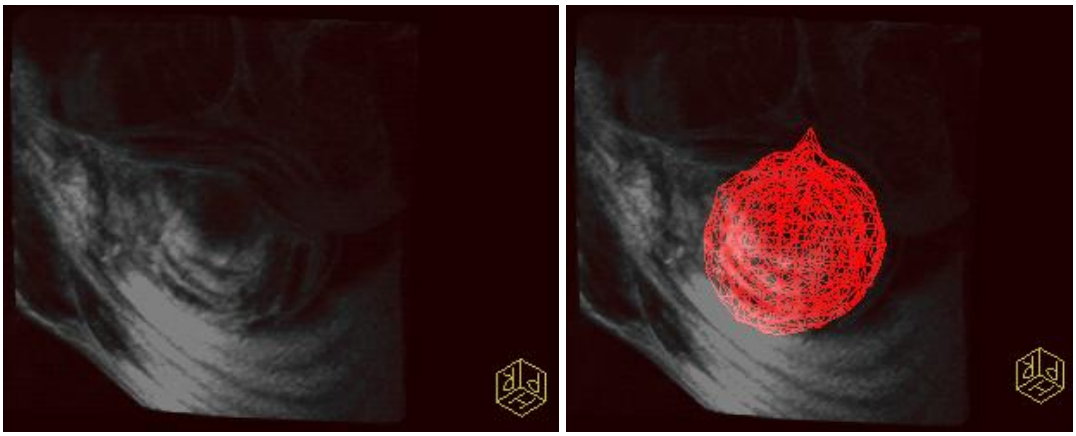

(a) (b)

Figure 3.29: The volume rendered DEMR of Patient 1 in the short axis view (a) and the same volume with the surface model of the left ventricle (b).

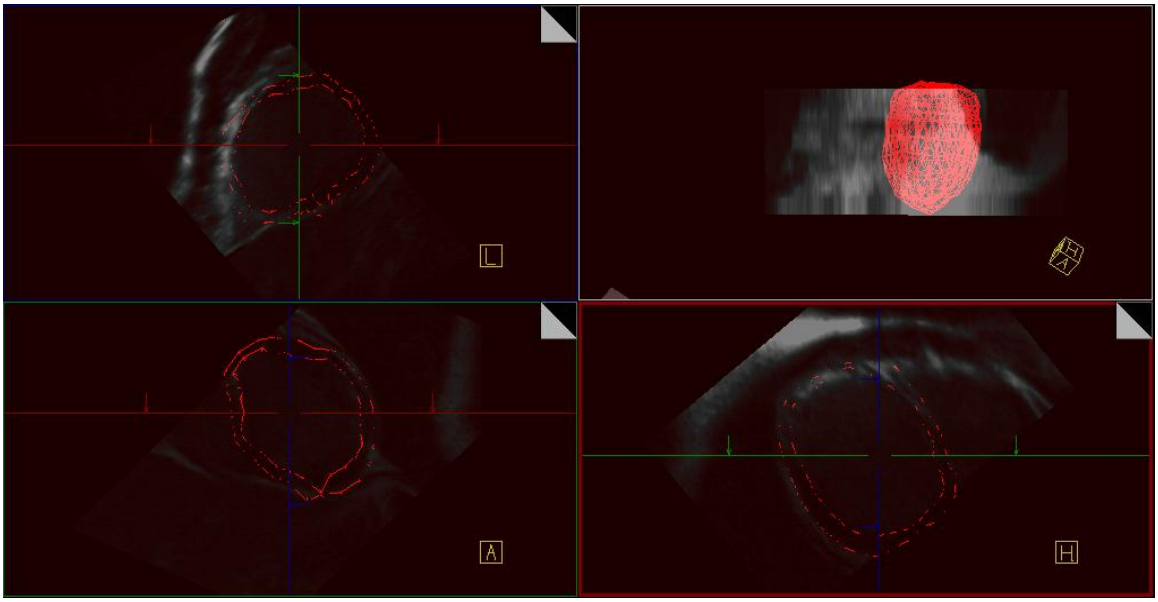

Figure 3.30: The DEMR volume for Patient 1 with the geodesic model of the LV in red.

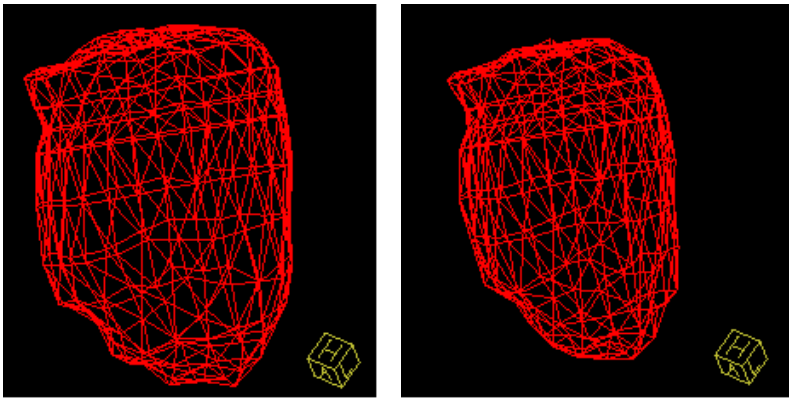

Figure 3.31: Epicardium (to the left) and endocardium (to the right) models of the LV identified in the DEMR for Patient 1.

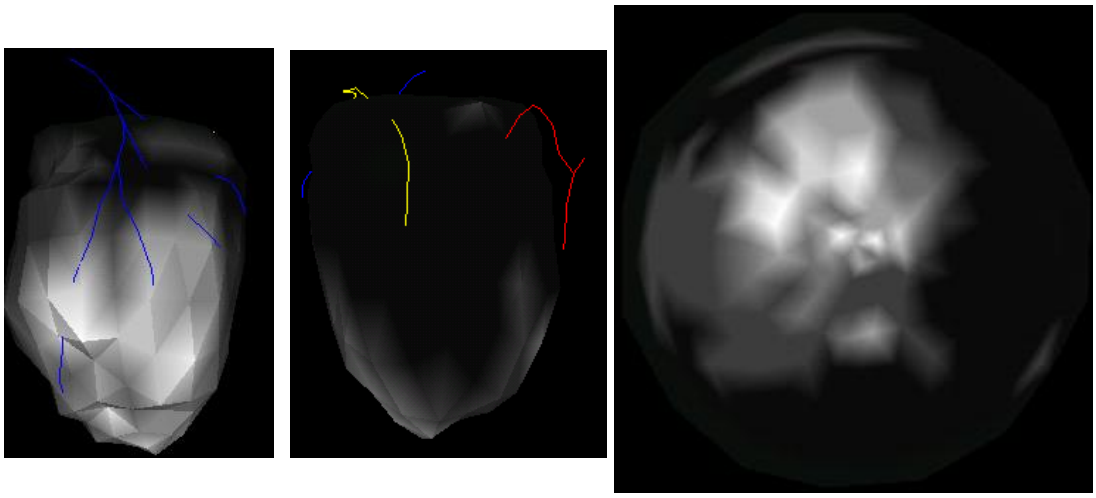

(a) (b) (c)

Figure 3.32 : Viability map for Patient 1 as computed by our method, in 3D with colored coronaries (a and b) and in 2D (c).

Patient 3

The DEMR images available for Patient 3 are shown in the short axis direction in Figure 3.33 where it is possible to see the overlaid 3D surface model points in red. The LV epicardium model is composed of 258 points, similarly for the endocardium model and shown in Figure 3.34. The model expands outside the DEMR sequence of images as can be seen in Figure 3.33 c). The viability model is presented in Figure 3.35 in 3D with the coronary structure, and over a 2D viability map. Points that fall outside the image are assigned the color blue. The region close to the apex is absent and the middle of the continuous viability map is therefore colored as such. Areas of loss of viability are located between the LAD and the RCA.

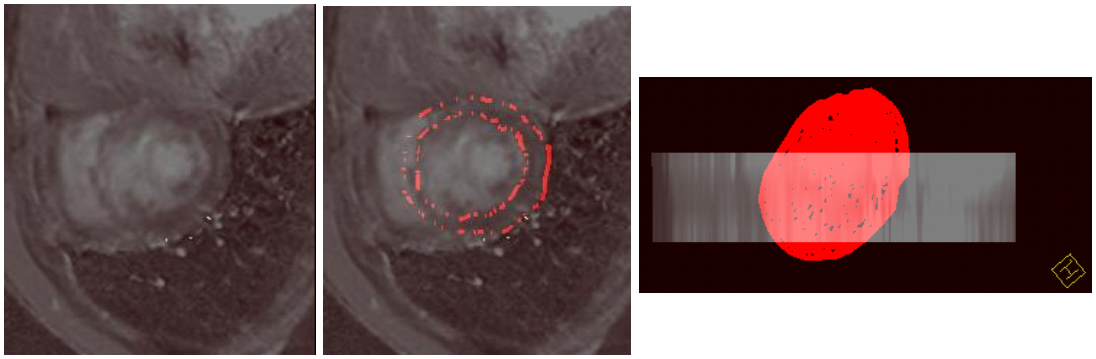

(a) (b) (c)

Figure 3.33 : The DEMR volume for Patient 3 (a) with the LV surface points and their interconnections drawn in red (b) (c).

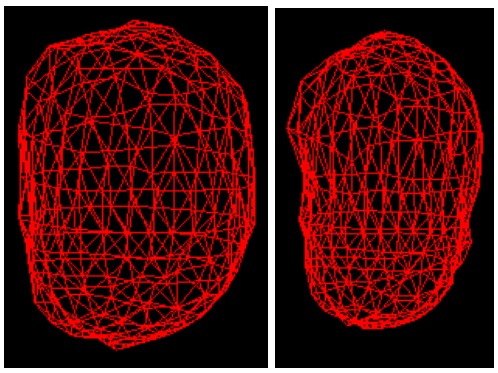

Figure 3.34 : LV surface model (epicardium to the left and endocardium to the right) from DEMR for Patient 3.

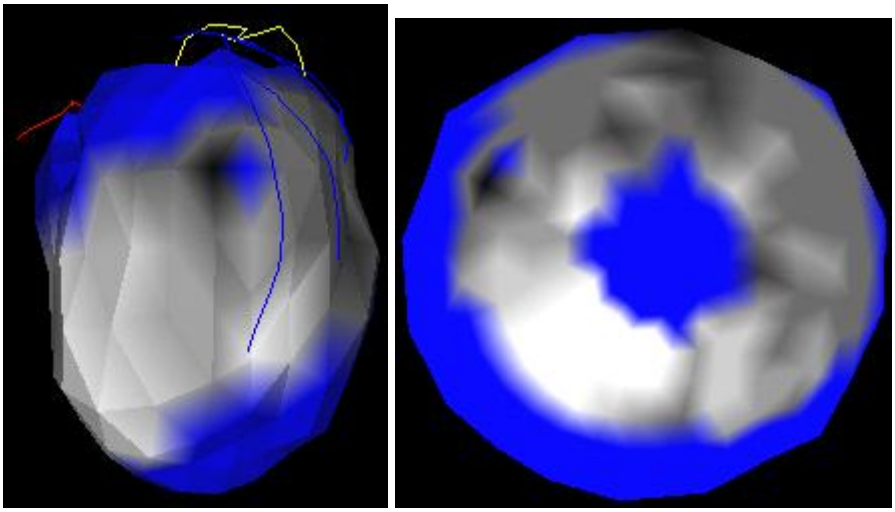

Figure 3.35 : Viability map for Patient 3 in 3D and over a 2D map.

Patient 5

The DEMR images available for Patient 5 are shown in the short axis direction in Figure 3.36 where it is possible to see the overlaid 3D surface model points in red. The LV epicardium model is composed of 258 points, similarly for the endocardium model and shown in Figure 3.37. The viability projection is presented in Figure 3.38.

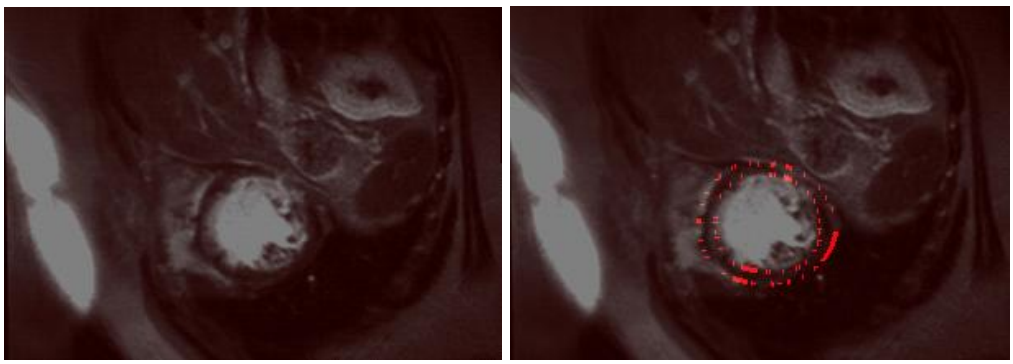

Figure 3.36 : DEMR multiplanar reconstruction in the short axis direction for Patient 5.

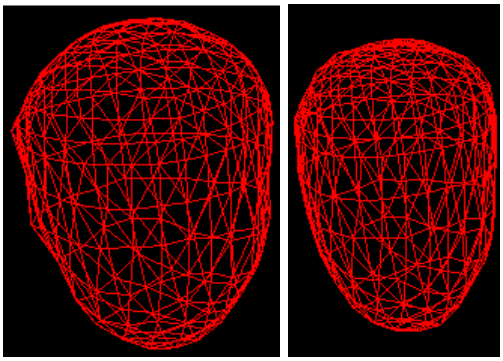

Figure 3.37 : Epicardium (to the left) and endocardium (to the right) models of the LV identified in the DEMR for Patient 5.

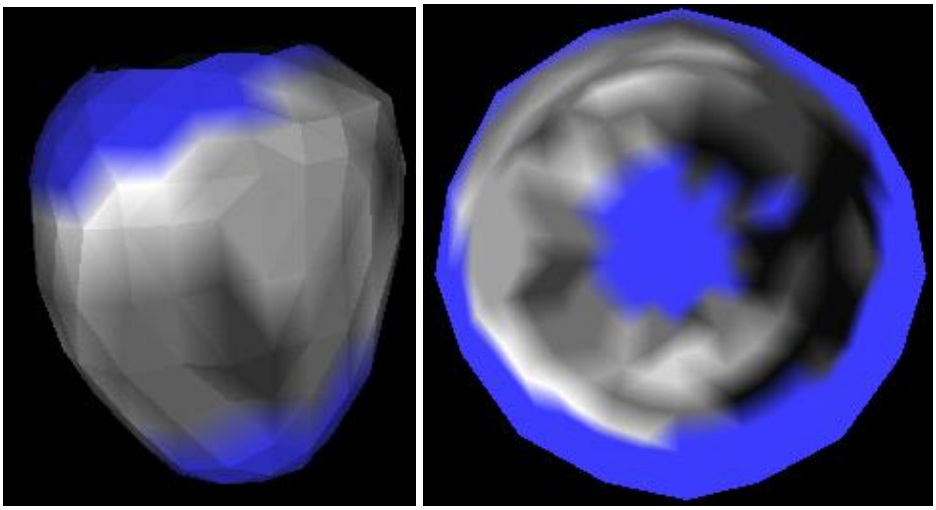

Figure 3.38 : Viability in 3D and 2D for Patient 5 as computed by our method.

Patient 6

The DEMR for Patient 6 is shown in the short axis direction in Figure 3.39 where points of the 3D LV model are shown in red. The LV epicardium model is composed of 258 points, similarly for the endocardium model and shown in Figure 3.40. For this patient the DEMR images did not reach the cardiac base, which is depicted by the blue region in

the viability map Figure 3.41). Moreover the DEMR volume does not cover the apex and this region is therefore blue as well in the continuous viability map.

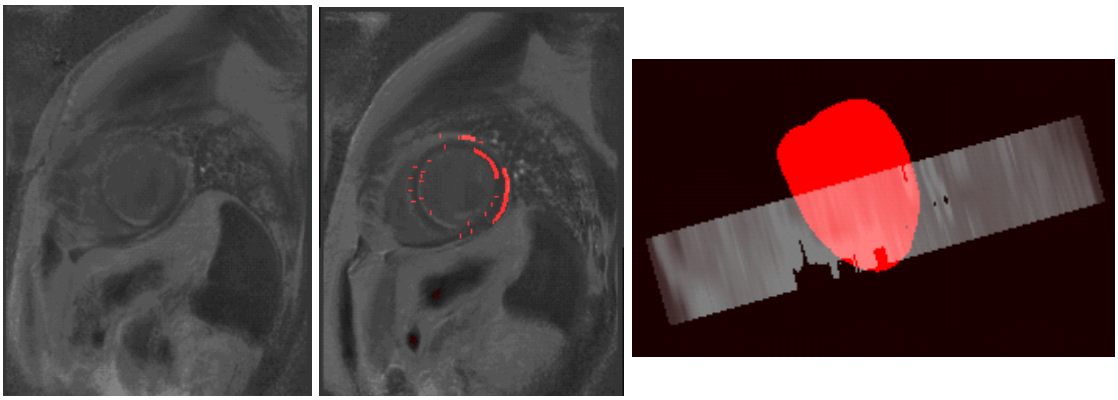

(a) (b) (c)

Figure 3.39 : DEMR multiplanar reconstruction in the short axis direction for Patient 6 (a) and with LV surface points in red (b) and in a 3D rendered view (c).

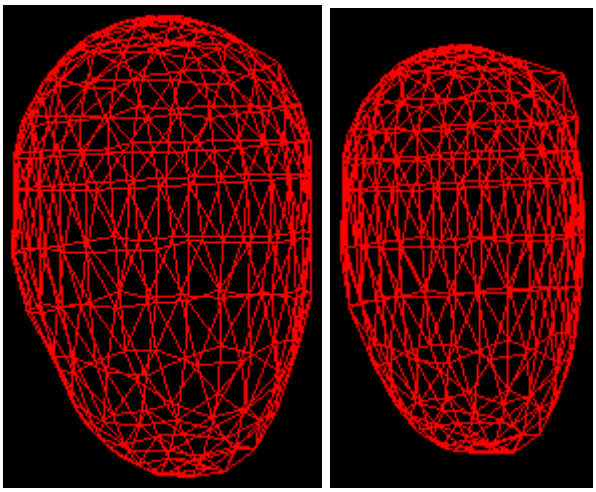

Figure 3.40: LV epicardial (to the left) and endocardium (to the right) surface from DEMR for Patient 6.

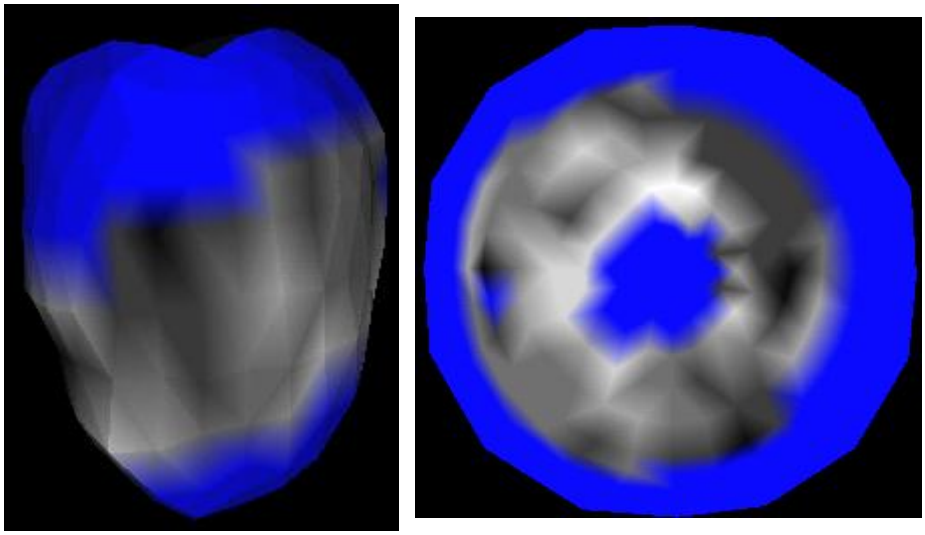

(a) (b)

Figure 3.41 : Viability map for Patient 6 in 3D (a) and 2D (b).

3.4 Viability Map

The fusion of CT-derived maps with DEMR image studies are presented over the circular map. Coronary perfusion territories are overlaid the viability map and together created an augmentd model where the clinician can identify dead myocardial cells and infer the responsible diseased coronary. The coronary territories are rendered as boundaries and are denoted by colored lines: blue/green separates the LAD and the LCX territories, blue/brown separates the LAD from RCA and green/brown separates CFX and RCA. Results for patient 1 are shown in Figure 3.42. This patient has 100% blockage of the LAD, with no significant stenosis of the LCX and 70% blockage of the RCA, reflected in the bright regions in the LAD territory with mildly increased signal intensity in the RCA territory. Result for patient 3 is shown in Figure 3.43.

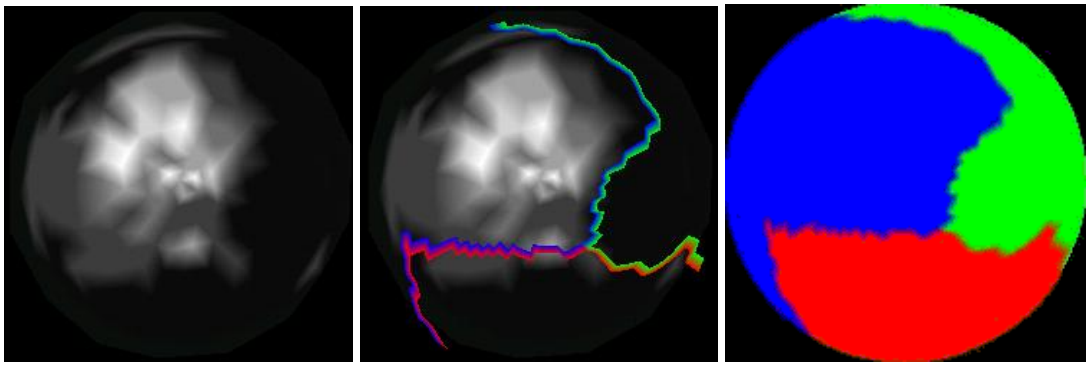

(a) (b) (c)

Figure 3.42: Viability map for Patient 1 (a), with overlaid coronary territory borders (b) and for comparison the color coded territory map (c) (LAD blue, LCX green and RCA red).

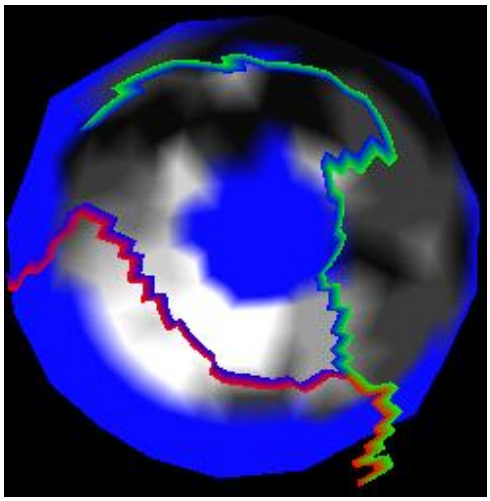

Figure 3.43: Coronary territories overlaid viability map for patient 3.

CHAPITRE 4 DISCUSSION

The general objective was to create a patient-specific diagnostic tool that would allow visualization of myocardial viability and determine which coronary is responsible for its perfusion. We have achieved our goal and presented a continuous map depicting coronary territories over viability information over a 2D map similar to the 17-segment model. However there are limits to the model that are presented in this section.

4.1 Coronary Territories

Coronaries found in the CTA volume are generally clear enough for the clinician to identify them directly on slices. However coronaries grow smaller in diameter as they leave their birth place at the ostia. They are therefore harder to identify distally. It is important to understand that the patient-specific map that we compute is directly dependant on coronary identification by the physician. We compare our coronary territory map to the one created with the Green Lane method. In this method the coronaries are identified with an angiogram which makes it easier to correctly select the position of coronaries and their branches. On the other hand, the territories found with the Green Lane method are prone to a certain amount of error since the coronary territories are traced by hand after a clinician mentally interprets the 2D projection back to 3D. We therefore expected a difference in the shape of the coronary territories in our patient-specific map as compared to the results of the Green Lane method. Even so, the percentage area of overlap seems to validate the correspondence of coronary territories.

It is possible to observe the superior concordance of our result with regards to the Green Lane method as compared to the 17-segment model versus the Green Lane model. This is explained by the fact that our method adapts to the patient’s coronary structure and we

should have a better correspondence when a patient's anatomy varies from the general population. Our maps therefore accurately represent the specific coronary structure of an individual patient based on the information from CTA volumes.

The association between the points on the model and closest coronaries has been resolved using Dijkstra's algorithm. It has proven a reliable method and is the basis of many distance algorithms. It requires the surface of the geodesic model to be taken as graph. The execution time of the algorithm is reasonable. However the algorithm is first used to calculate the shortest distance of all points of the model to points of the coronaries and the shortest path is determined afterwards. The fact that the algorithm expands in all directions uniformly before reaching the target adds computation time. This two step method can be optimized and many other methods could be considered. The Marching Cubes method has recently been used [175].

4.2 Registration of perfusion territories over viability

Since both images are from different modalities and acquired at differing times, it is hard to guarantee that the images represent the exact same time in the cardiac cycle. Even the precision of the ECG gated acquisition does not guarantee that the images are taken at precisely the same moment during the ECG cycle. Moreover, myocardium in CHD patients might undergo shape variation due to the molecular impact of the disease on the organ.

The presence of contrast agent in the myocardium in images from DEMR and the absence of this agent in the myocardium (though not the coronaries) from CTA volume make it harder to have a registration method that is intensity-based. The results we have

obtained are satisfying for the available datasets. The deformation is dictated by thin plate spline registration method that acts only on the geodesic models. The absence of control points in the other areas of the available datasets exposes our assumption that surrounding organs do not deform. This explains why there is absence of correspondence of surrounding organs following the registration. These factors might explain why the final mutual information transformation values in the cardiac regions are not significantly higher than in the rest of the transformation domain. This registration method is therefore sensitive and should undergo more improvement to be more robust.

Using the thin plate spline method with our data has been successful. However time of execution is long due to the high number of landmarks. The registration is also directly dependant on the quality of the segmentation in both modalities. It is in fact possible to see the effect of an outlier point on the final registration method. A landmark positioning error should have been included to prevent such a deformation to take place.

In segmenting the myocardium border, the endocardium is harder to identify since it undergoes more movement than the epicardium points, however the epicardium border isn’t as clear and distinctive which also makes it hard to identify. A landmark positioning error was excluded from this project after it proved too difficult to predict the exact possible errors automatically.

One limitation of the validation of registration is due to the paucity of available LV segmentations as landmarks. A pure intensity-based registration method could have been validated using a distance metric over the segmentation in both models. However such a method is difficult to apply considering the contrast agents involved in the acquisitions, as was previously discussed. This limits the validation to a qualitative evaluation.

Unfortunately, the distance measure between insertion points of the LV in both modalities is considered a qualitative evaluation since the insertion points are chosen manually.

4.3 Viability map

While projecting functional information from DEMR over the circular map, two different locations on the LV might be projected onto the same point on the map. A choice of projected intensities has to be made in the case of MR projection. Since loss of viability is indicated by higher intensities, the highest intensities are the ones kept during spherical projection. The 3D texture is therefore altered when projected and the physician has to be made aware that the uniformity of the viability is not kept intact. However locations of non-viability are not overwritten since brighter intensities are kept. The clinician can therefore be sure to see all of the location of non-viability on the map that he would normally be able to see in 3D.

4.4 Projection of structure and function from 3D to 2D

The orientation of the axis of the heart influences the result of the projection from 3D to 2D. Since this orientation is found with the PCA method previously described, there might be problems for patients whose hearts have anomolous shapes, a possibility in the presence of CHD. This might result in the long axis found with PCA not going through the exact position of the apex of the heart of the patient. We have not encountered such a situation but would need investigation with patients showing this particularity to address it properly. Specific cases of leaking coronaries into the blood pool of the LV have previously been brought to our attention however we have not encountered such cases in

our database. There would again be a need for further investigation to determine the result of our method in such cases.

Based on past studies, a greater variability of coronary distribution around the apex was expected compared to the 17-segment model. This was observed in our computed coronary territory maps. In some cases the LAD wraps around the apex and feeds the posterior portion of the heart. There is some discordance of territory shape at the base (outermost ring) where the LCX seems to wrap around to the left main in most models (from the top right to the top left of the territory map). This could be due to distortion during projection of texture from 3D to 2D. However this is also seen in the Green Lane model it could therefore be explained by the continuous property of both models: the birth place of the LCX is from the ostia and it wraps around the LV base to reach the anterolateral surface of the LV.

CONCLUSION

We have achieved our goal of creating a patient-specific coronary territories map overlay a viability map presenting the functional as well as structural information of interest to the clinician during diagnosis of CHD. The different coronaries and their respective territories are visible over a color coded map of myocardial viability. The territories computed with our method show overall correspondence with regards to the ground truth available for each patient. The overlay of myocardial viability should allow the clinician to establish a correspondence between a loss of viability and a specific coronary. Moreover our method allows the clinician to associate a territory with any branch vessel. That is, it is possible to create a patient-specific viability map depicting an extra region of interest in addition to the standard three vessel classification of the standard 17-segment model. Moreover we have improved the registration method with regards to past manual registration methods [38], [33].

The computed map presents results in a continuous fashion (all viability information is projected into the map) whereas the 17-segment model presents viability in a discrete manner. Our viability map therefore contains more information regarding the location and geometry of affected myocardial tissue.

While the presented results are an improvement over the 17-segment model, some criticism can be formulated for each step of our method and there is place for improvement at different levels.

The method of identification of coronaries has room for improvement. An automatic identification of coronaries would be the optimal and most desired solution, leaving the clinician only to verify the exactness of coronary position.

Since clinicians are interested in localization of non-viable tissues, a simple polar projection is chosen. However one potential improvement could be a different choice of projection to visualize loss of viability. Many projection methods exist. For example the interrupted Goode homolosine projection would result in unwrapping of the heart along the long axis of the heart, as would the Mercador projection. However the clinicians are used to studying a circular map such as the 17-segment model and the use of any other kind of projection would require an adaptation on their part, with the associated time to understand and interpret the model. However it is known that with the currently developed map, it is still difficult for the clinician to quantify how the non-viable myocardial cells are spread over the myocardium due to distortion introduced during the projection. Many projection results could be tried as an investigation of information presentation.

Moreover it is also arguable that the coronary territories would be decided only by the distance of a point on the surface to a coronary. We have effectively seen this with the RCA wrapping around the RV: points from this coronary that wrap around the RV had to be removed since they do not participate in the septum perfusion being at the opposite side of the RV. This is confirmed by more precise perfusion studies [144].

Our fused model showing myocardial viability and coronary structure should allow the clinician to establish a correspondence between a loss of viability and a specific coronary. Moreover our method allows the clinician to associate a territory with any branch vessel.

The method we have developed is an improvement over the previous one that required manual adjustments during registration. Although there are some improvements to bring to the model, we have advanced with regards to the previous methods. Further development of the method could lead to a diagnosis tool usable in clinical practice.

REFERENCES

[1] National Heart, lung and blood institute, Disease and condition index, "What is coronary artery disease", http://www.nhlbi.nih.gov/health/dci/Diseases/Cad/CAD_WhatIs.html

[2] "Heart Disease and Stroke Statistics", American Heart Association, 2009 update, http://www.americanheart.org

[3] Besl P.J., McKay N.D., "A Method for Registration of 3-D Shapes", IEEE Transactions on Pattern Analysis and Machine Intelligence, vol. 14, no. 2, pp. 239-256, 1992.

[4] Kanderian A.S., Renapurkar R., Flamm S.D., "Myocaridal viability and revascularization", Heart Fail Clin., vol. 5, no. 3, vi, 2009.

[5] Widmaier E.P., Raff H., Strang K.T. "Vander, Sherman, Luciano's Human Physiology: The Mechanisms of body function", 9th edition, McGraw-Hill Companies, 2004.

[6] NewYork – Presbiterian Hospital, "Heart Anatomy", http://nyp.org/health/cardiac-anatomy.html, accessed December 2009.

[7] Kaimkhani Z.A., Ali M.M., Faruqi A.M., "Pattern of coronary arterial distribution and its relation to coronary artery diameter", Journal of Ayub Medical College, Abbottabad: JAMC, vol. 17, no. 1, pp. 40-43, 2005.

[8] Ortale J.R., Keiralla L.C.B., Campinas L.S., "The posterior ventricular branches of the coronary arteries in the human heart", Arquivos Brasileiros de Cardiologia, Volume 82, No 5, May 2004.

[9] Ilia R, Rosenshtein G, Weinstein J, Cafri C, Abu-Ful A, Gueron M., "Left anterior descending artery length in left and right coronary artery dominance", Coron Artery Dis., vol. 12, no. 1, pp. 77-78, 2001.

[10] McKellar S.H., "Cardiac Anatomy", http://www.ctsnet.org/doc/4693, accessed December 2009.

[11] Nerantzis CE, Papachristos JC, Gribizi JE, Voudris VA, Infantis GP, Koroxenidis GT., "Functional dominance of the right coronary artery: incidence in the human heart.", Clin Anat., vol. 9, no.1, pp. 10-13, 1996.

[12] Musselman DR, Tate DA., "Left coronary dominance due to direct continuation of the left anterior descending to form the posterior descending coronary artery", Chest., vol. 102, no. 1, pp. 319-320, 1992.

[13] Baptista CA, DiDio LJ, Teofilovski-Parapid G., "Variation in length and termination of the right coronary artery in man", Jpn Heart J., vol. 30, no.6, pp.789-798, 1989.

[14] Vasheghani-Farahani A, Kassaian SE, Yaminisharif A, Davoodi G, Salarifar M, Amirzadegan A, Darabian S, Fotouhi A, Sadigh G, Razavi SA, Hakki E., "The association between coronary arterial dominancy and extent of coronary artery disease in angiography and paraclinical studies", Clin Anat., vol. 21, no. 6, pp. 519-523, 2008.

[15] Saidi HS, Olumbe AO, Kalebi A., "Anatomy and pathology of coronary artery in adult black Kenyans.", East Afr Med J., vol. 79, no. 6, pp. 323-327, 2002.

[16] Goldberg A, Southern DA, Galbraith PD, Traboulsi M, Knudtson ML, Ghali WA, "Coronary dominance and prognosis of patients with acute coronary syndrome.", Am Heart J., vol. 154, no. 6, pp. 1116-22, 2007.

[17] Kaimkhani ZA, Ali MM, Faruqi AM., "Pattern of coronary arterial distribution and its relation to coronary artery diameter.", J Ayub Med Coll Abbottabad., vol. 17, no. 1, pp.40-43, 2005.

[18] Gorlin R., “Coronary anatomy”, Major Probl Intern Med., vol. 11, pp. 40-58, 1976.

[19] Berne R.M., Levy M.N., “Cardiovascular Physiology”, The Mosby Physiology Monograph Series, Eight Edition.

[20] The Free Dictionary by Farlex, “Cardiac Cycle”, Dorland's Medical Dictionary for Health Consumers, http://medical-dictionary.thefreedictionary.com/cardiac+cycle, accessed December 2009.

[21] American Heart Association website: http://www.americanheart.org/. Accessed: December 2009.

[22] Moebus S., Stang A., Möhlenkamp S., Dragano N., Schmermund A., Slomiany U., Hoffmann B., Bauer M., Broecker-Preuss M., Mann K., Siegrist J., Erbel R., Jöckel K.H., Heinz Nixdorf Recall Study Group., “Association of impaired fasting glucose and coronary artery calcification as a marker of subclinical atherosclerosis in a population-based cohort-results of the Heinz Nixdorf Recall Study.”, Diabetologia, 2008 Nov 1. [Epub ahead of print].

[23] Maintz J.B.A., Viergever M.A., “A Survey of Medical Image Registration”, Medical Image Analysis, vol. 2, no. 1, pp. 1-36, 1998.

[24] Dictionnaire Merriam Webster en ligne, http://www.merriam-webster.com, accessed November 2009.

[25] Sahni D., Kaur G.D., Jit H., Jit I., “Anatomy & distribution of coronary arteries in pig in comparison with man”, Indian J Med Res., vol. 127, no.6, pp.564-570, 2008.

[26] Vieira T.H., Moura P.C. Jr, Vieira S.R., Moura P.R., Silva N.C., Wafae G.C., Ruiz C.R., Wafae N., “Anatomical indicators of dominance between the coronary arteries in swine”, Morphologie., vol.92, no. 296, pp. 3-6, 2008.

[27] Stary H.C, Chandler A.B., Glagov S.,Guyton J.R., Insull W., Rosenfeld M.E., Schaffer S.A., Schwartz C.J., Wagner W.D., Wissler R.W. “A Definition of Initial, Fatty

Streak, and Intermediate Lesions of Atherosclerosis, A Report From the Committee on Vascular Lesions of the Council on Arteriosclerosis, American Heart Association", Circulation, vol. 89, pp. 2462-2478, 1994.

[28] Herbert C.S., Bleakley A.C., Dinsmore R.E., Fuster V., GlagovS., Insull W., Rosenfeld M.E, Schwartz C.J., Wagner W.D., Wissler R.W., "A definition of Advanced Types of Atherosclerosis Lesions and a Histological Classification of Atherosclerosis. A report from the Committee on Vascular Lesions of the Council on Arteriosclerosis, American Heart Association", Circulation, vol. 92, pp. 1355-1374, 1995.

[29] MedLine Plus, "Atherosclerosis", http://www.nlm.nih.gov/medlineplus/ency/imagepages/18050.htm, accessed December 2009.

[30] Lu Z., Chen W., "Fast and Robust 3-D Image registration Algorithm Based on Principal Component Analysis", The 1st International Conference on Bioinformatics and Biomedical Engineering, 2007, ICBBE 2007. pp. 872-875.

[31] Tsao J., "Interpolation artifacts in multimodality image registration based on maximization of mutual information", IEEE Trans Med Imaging., vol.22, no. 7, pp. 854-64, 2003.

[32] Canal E., "The Cardiac Muscle", Springer-Verlag, 1986, Handbook of microscopic anatomy; vol. II, 7.

[33] Beliveau P., Setser R.M., Cheriet F., White R.D., O'Donnell T., "Computation of Coronary Perfusion Territories from CT Angiography", Computers in Cardiology, vol. 34, pp. 753−756, 2007.

[34] Cerqueira M.D., Weissman N.J., Dilsizian V., Jacobs A.K., Kaul S., Laskey W.K., Pennell D. J., Rumberger J.A., Ryan T., Verani M.S., "Standardized myocardial segmentation and Nomenclature for tomographic imaging of the heart", Circulation, vol. 105, pp. 539-542, 2002.

[35] Yale Atlas of Echocardiography, “Atlas of Echocardiography”, accessed December 2009.

[36] Vogel-Claussen J., Rochitte C.E., Wu K.C., Kamel I.R., Foo T.K., Lima J.A.C., Bluemke D.A., “Delayed Enhancement MR Imaging: Utility in Myocardial Assessment”, RadioGraphics, vol. 26, pp. 795-810, 2006.

[37] Bonow R.O., “Identification of Viable Myocardium,” Circulation, vol. 94, pp. 2674-2680, 1996.

[38] Setser R.M., O’Donnell T.P., Smedira N.G., Sabik J.F., Halliburton S.S., Stillman A.E., White R.D., “Co-registered MRI myocardial viability maps, MDCT coronary angiogram displays and surgical revascularization planning: Initial experience.” Radiology, vol.237, pp. 465-473, 2005.

[39] “What is a coronary angiogram”, American Heart Association, 2007, www.americanheart.org, accessed November 2009.

[40] MedLine Plus, “Coronary Angiography”, http://www.nlm.nih.gov/medlineplus/ency/imagepages/18129.htm, accessed December 2009.

[41] Gunduz H., Akdemir R., Özhan H., Arinc H., Uyan C., “Iatrogenic Left Main Coronary Artery Thrombosis During Percutaneous Coronary Intervention”, Turkish Society of Cardiology, Turk Kardiyol Dern Ars, vol. 32, pp. 197-200, 2004.

[42] Canty J.M., Fallavollita J.A., “Hibernating myocardium”, J. Nucl. Cardiology, vol 12, pp. 104-19, 2005.

[43] Gerber B.L., Thanh H.T., Roelants V., Pasquet A., Vancraeynest D., Vanoverschelde J.L.J., “Flow-function relationships in chronic left-ventricular ischemic dysfunction: Impact of the transmurality of infarction”, J. Nucl. Cardiology, vol. 15, no. 3, pp. 363-74, 2008.

[44] Mueller R.L., Sanborn T.A., “The history of interventional cardiology: Cardiac catheterization, angioplasty, and related interventions”, Am Heart J, vol. 129, pp. 146-172, 1995.

[45] MedLine Plus, “Cardiac Catheterization”, http://www.nlm.nih.gov/medlineplus/ency/imagepages/1080.htm, accessed December 2009.

[46] MedLine Plus, “Coronary artery balloon angioplasty - series”, http://www.nlm.nih.gov/medlineplus/ency/presentations/100160_6.htm, accessed December 2009.

[47] Bainey K.R., Norris C.M., Graham M.M., Ghali W.A., Knudtson M.L., Welsh R.C., “Clinical in-stent restenosis with bare metal stents: Is it truly a benign phenomenon”, International Journal of Cardiology, vol. 128, pp. 378-382, 2008.

[48] Marieb E.N., Laurendeau G., “Anatomie et Physiologie Humaines”, Éditions du Renouveau Pédagogique Inc., 1993.

[49] Foussas S.G., Tsiaousis G.Z., “Revascularization treatment in patients with coronary artery disease”, Hiiokratia, vol. 12, no.1, pp. 3-10, 2008.

[50] “Coronary Artery Bypass Graft (CABG) Surgery”, Cleveland Clinic, Heart and Vascular Institute, https://www.clevelandclinic.org/heartcenter/pub/guide/disease/cad/treatment_heartsurg.htm, accessed December 2009.

[51] MedLine Plus, “Heart bypass surgery - series”, http://www.nlm.nih.gov/medlineplus/ency/presentations/100190_4.htm, accessed December 2009.

[52] Cleveland Clinic Website, http://my.clevelandclinic.org/default.aspx, accessed November 2009.

[53] “Arterial Coronary Artery Bypass Grafts, Internal thoracic artery (ICA, also called mammary artery) graft”, Cleveland Clinic Website: http://my.clevelandclinic.org/default.aspx, accessed November 2009.

[54] Berman D.S., Abidov A., Kang X., Hayes S.W., Friedman J.D., Sciammarella M.G., Cohen I., Gerlach J., Waechter P.B., Germano G., Hachamovitch R., “Prognostic validation of a 17-segment score derived from a 20-segment score for myocardial perfusion SPECT interpretation”, Journal of Nuclear Cardiology, vol. 11, no. 4, pp. 414-423, 2004.

[55] Partridge J.B., Anderson R.H., “Left ventricular anatomy: its nomenclature, segmentation, and planes of imaging”, Clin. Anat., vol. 22, no. 1, pp. 77-84, 2009.

[56] Hoffman JW Jr, Gilbert TB, Poston RS, Silldorff EP., “Myocardial reperfusion injury: etiology, mechanisms, and therapies.”, J Extra Corpor Technol., vol. 36, no. 4, pp. 391-411, 2004.

[57] Kloner R.A., Rezkalla S.H., “Preconditioning, postconditioning and their application to clinical cardiology”, Cardiovasc Res., vol. 70, no. 2, pp. 297-307, 2006.

[58] Zhao Z.Q., Corvera J.S., Halkos M.E., Kerendi F., Wang N.P., Guyton R.A., Vinten-Johansen J., “Inhibition of myocardial injury by ischemic postconditioning during reperfusion: comparison with ischemic preconditioning”, Am J Physiol Heart Circ Physiol. 2003 Aug;285(2):H579-88

[59] Hausenloy D.J., “Signalling pathways in ischaemic postconditioning”, Thromb Haemost., vol. 101, no. 4, pp. 626-34, 2009.

[60] van Vuuren D., Lochner A., “Ischaemic postconditioning: from bench to bedside”, Cardiovasc J Afr., vol. 19, no. 6, pp. 311-20, 2008.

[61] Lin E.C., “Coronary computed tomography angiography: principles of contrast material administration”, Journal of Cardiovascular Computed Tomography, vol. 1, pp. 162-165, 2007.

[62] Hawman E. G., Rempel T. D., Vija, A. H., Engdahl, J. C., “Line array transmission sources for SPECT attenuation correction: design and reconstruction”, Medical Imaging 2005: Physics of Medical Imaging, Proceedings of the SPIE, vol. 5745, pp. 79-89, 2005.

[63] Motomura N., Takahashi M., Nakagawara G., Iida H., “Evaluation of a SPECT attenuation correction method using CT data registered with automatic registration software”, Nuclear Science Symposium Conference Record, IEEE, Vol.4, pp. 2676-2680, 2003.

[64] Fricke E., Fricke H., Weise R., Kammeier A., Hagedorn R., Lotz N., Lindner O., Tschoepe D., Burchert W., “Attenuation Correction of Myocardial SPECT Perfusion Images with Low-Dose CT: Evaluation of the Method by Comparison with Perfusion PET”, Journal of Nuclear Medicine, vol. 46, no. 5, pp. 736-744.

[65] Bajc M., Olsson B., Palmer J., Jonson B., “Ventilation/Perfusion SPECT for diagnostics of pulmonary embolism in clinical practice”, J Intern Med., vol. 264, no. 4, pp. 379-87, 2008.

[66] Catafau A.M., “Brain SPECT in Clinical Practice. Part I: Perfusion”, Journal of Nuclear Medicine Vol. 42 No. 2 259-271

[67] Utsunomiya D., Nakaura T., Honda T., Shiraishi S., Tomiguchi S., Kawanaka K., Morishita S., Awai K., Ogawa H., Yamashita Y., “Object-specific attenuation correction at SPECT/CT in thorax: optimization of respiratory protocol for image registration.”, Radiology., vol. 237, no. 2, pp. 662-9, 2005.

[68] Kashiwagi T., Yutani K., Fukuchi M., Naruse H., Iwasaki T., Yokozuka K., Inoue S., Kondo S., “Correction of nonuniform attenuation and image fusion in SPECT imaging by means of separate X-ray CT”, Ann Nucl Med., vol. 16, no. 4, pp. 255-261, 2002.

[69] Dey D., Slomka P.J., Hahn L.J., Kloiber R., "Automatic three-dimensional multimodality registration using radionuclide transmission CT attenuation maps: a phantom study", J Nucl Med., vol. 40, no. 3, pp. 448-55, 1999.

[70] Goetze S., Wahl R.L., "Prevalence of misregistration between SPECT and CT for attenuation-corrected myocardial perfusion SPECT", J. Nucl Cardiol., vol. 14, no. 2, pp. 200-206, 2007.

[71] Kumita S., Cho K., Nakajo H., Toba M., Fukushima Y., Mizumura S., Kumazaki T., "Clinical Applications of ECG-gated Myocardial Perfusion SPECT", J. Nippon Med. Sch. 2006; 73 (5).

[72] Di Carli M.F., Dorbala S., Meserve J., El Fakhri G., Sitek A., Moore S.C., "Clinical myocardial perfusion PET/CT", J Nucl Med., vol. 48, no. 5, pp. 783-93, 2007.

[73] Bateman T.M., "Cardiac positron emission tomography and the role of adenosine pharmacologic stress", The American Journal of Cardiology, vol. 94, no. 2, pp. 19-24, 2004.

[74] Chua S.C., Ganatra R.H., Green D.J., Groves A.M., "Nuclear cardiology: myocardial perfusion imaging with SPECT and PET", Imaging 18, 166-177, 2006.

[75] Ben-Haim S., Kupzov E., Tamir A., Israel O. , "Evaluation of 18F-FDG uptake and arterial wall calcifications using 18F-FDG PET/CT", J Nucl Med., vol. 45, no. 11, pp. 1816-21, 2004.

[76] Williams G., Kolodny GM., "Retrospective study of coronary uptake of 18F-fluorodeoxyglucose in association with calcification and coronary artery disease: a preliminary study", Nucl Med Commun., vol. 30, no. 4, pp. 287-91, 2009.

[77] Goetze S., Wahl R.L., "Prevalence of misregistration between SPECT and CT for attenuation-corrected myocardial perfusion SPECT", Journal of Nuclear Cardiology, vol. 14, no. 2, pp. 200-6, 2007.

[78] Guetter C., Wacker M., Xu C., Hornegger J., “Registration of cardiac SPECT/CT data through weighted intensity co-occurrence priors”, Int Conf Med Image Comput Comput Assist Interv., vol. 10, pt. 1, pp. 725-33, 2007.

[79] Walimbe V., Zagrodsky V., Raja S., Jaber W.A., DiFilippo F.P., Garcia M.J., Brunken R.C., Thomas J.D., Shekhar R., “Mutual information-based multimodality registration of cardiac ultrasound and SPECT images: a preliminary investigation”, Int J Cardiovasc Imaging., vol. 19, no. 6, pp. 483-94, 2003.

[80] Misko J., Dziuk M., Skrobowska E., Szalus N., Pietrzykowski J., Warczynska A., “Co-registration of cardiac MRI and rest gated SPECT in the assessment of myocardial perfusion, function and viability”, J Cardiovasc Magn Reson., vol. 8, no. 3, pp. 389-97, 2006.

[81] Aladl U.E., Hurwitz G.A., Dey D., Levin D., Drangova M., Slomka P.J., “Automated image registration of gated cardiac single-photon emission computed tomography and magnetic resonance imaging.”, J Magn Reson Imaging., vol. 19, no. 3, pp. 283-90, 2004.

[82] Faber T.L., McColl R.W., Opperman R.M., Corbett J.R., Peshock R.M., “Spatial and temporal registration of cardiac SPECT and MR images: methods and evaluation”, Radiology, vol. 179, no. 3, pp. 857-61, 1991.

[83] Zhang W., Noble J.A., Brady J.M., “Spatio-temporal registration of real time 3D ultrasound to cardiovascular MR sequences.”, Int Conf Med Image Comput Comput Assist Interv., vol. 10, pt. 1, pp. 343-50, 2007.

[84] Nekolla S.G., Martinez-Moeller A., Saraste A., “PET and MRI in cardiac imaging: from validation studies to integrated applications”, Eur J Nucl Med Mol Imaging., vol. 36 suppl. 1, pp. S121-30, 2008.

[85] Schwitter J., “Myocardial perfusion imaging by cardiac magnetic resonance”, J Nucl Cardiol., vol. 13, no. 6, pp. 841-54, 2006.

[86] Kwong R.Y., Korlakunta H., “Diagnostic and prognostic value of cardiac magnetic resonance imaging in assessing myocardial viability”, Top Magn Reson Imaging., vol. 19, no. 1, pp. 15-24, 2008.

[87] Simonetti O.P., Kim R.J., Fieno D.S., Hillenbrand H.B., Wu E., Bundy J.M., Finn J.P., Judd R.M., “An improved MR imaging technique for the visualization of myocardial infarction”. Radiology, vol. 218, pp. 215-223, 2001.

[88] Strzelczyk J., Attili A., “Cardiac Magnetic Resonance Evaluation of Myocardial Viability and Ischemia”, Cardiac Imaging, Part II, vol. 43, no. 3, pp. 193-203, 2008.

[89] Reddy G.P., Pujadas S., Ordovas K.G., Higgins C.B., “MR imaging of ischemic heart disease”, Magn Reson Imaging Clin N Am., vol. 16, no. 2, pp. 201-12, 2008, viii.

[90] Jerosch-Herold M., Kwong RY., “Magnetic resonance imaging in the assessment of ventricular remodeling and viability”, Curr Heart Fail Rep., vol. 5, no. 1, pp. 5-10, 2008.

[91] Wu H.D., Kwong R.Y., “Cardiac Magnetic Resonance Imaging in Patients with Coronary Disease”, Curr Treat Options Cardiovasc Med., vol. 10, no. 1, pp. 83-92, 2008.

[92] Beach S., Syed MA., “Current and upcoming roles of CT and MRI in clinical cardiac imagery”, Curr Cardiol Rep., vol. 9, no. 5, pp. 420-427, 2007.

[93] Klein S., Staring M., Pluim J.P., “Evaluation of optimization methods for nonrigid medical image registration using mutual information and B-splines”, IEEE Trans Image Process., vol. 16, no. 12, pp. 2879-90, 2007.

[94] Nakajo H., Kumita S., Cho K., Kumazaki T., “Three-dimensional registration of myocardial perfusion SPECT and CT coronary angiography”, Ann Nucl Med., vol. 19, no. 3, pp. 207-15, 2005.

[95] Goetze S., Brown T.L., Lavely W.C., Zhang Z., Bengel F.M., “Attenuation correction in myocardial perfusion SPECT/CT: effects of misregistration and value of reregistration”, J. Nucl. Med., vol. 48, no. 7, pp. 1090-5, 2007.

[96] Jin J., “Electromagnetic Analysis and Design in Magnetic Resonance Imaging”, Biomedical Engineering, CRC Press Inc., 1962.

[97] Purcell E.M., Torrey H.C., Pound R., “Principles of Magnetic Resonance Imaging”, http://www.easymeasure.co.uk/principlesmri.aspx, 2002, accessed September 2009.

[98] Liang Z.-P., Lauterbur P.C. “Principles of Magnetic Resonance Imaging: A Signal Processing Perspective”, Wiley-IEEE Press, 1999.

[99] Ozben B., Cinçin A.A., Mutlu B., “Assessment of myocardial viability with cardiac magnetic resonance imaging”, Anadolu Kardiyol Derg. 8 Suppl 2, pp. 71-6, 2008.

[100] Huang X., Moore J., Guiraudon G., Jones D., Bainbridge D., Ren J., Peters T., “Dynamic 2D Ultrasound and 3D CT Image Registration of the Beating Heart”, IEEE Trans Med Imaging., vol. 28, no. 8, pp. 1179-89, 2009.

[101] Klein G.J., Thirion J.P., “Cardiovascular imaging to quantify the evolution of cardiac diseases in clinical development”, Biomarkers., 10 Suppl 1:S1-9, 2005.

[102] White J.A., Pflugfelder P.W., Boughner D.R., Kostuk W.J., “Validation of a three-dimensional intravascular ultrasound imaging technique to assess atherosclerotic burden: potential for improved assessment of cardiac allograft coronary artery disease”, Can J Cardiol., vol. 19, no. 10, pp. 1147-53, 2003.

[103] Kasprzak J.D., Drozdz J., Peruga J.Z., Rafalska K, Krzemińska-Pakuła M., “Definition of flow parameters in proximal nonstenotic coronary arteries using transesophageal Doppler echocardiography”, Echocardiography., vol. 17, no. 2, pp. 141-50, 2000.

[104] Han H.C., “An echocardiogram-based 16-segment model for predicting left ventricular ejection fraction improvement”, J Theor Biol., vol. 228, no.1, pp. 7-15, 2004.

[105] Koszegi Z., Balkay L., Galuska L., Varga J., Hegedus I., Fulop T., Balogh E., Jenei C., Szabo G., Kolozsvari R., Racz I., Edes I., “Holistic polar map for intergrated

evaluation of cardiac imaging results", Computerized Medical Imaging and Graphics, vol. 31, pp. 577-586, 2007.

[106] de Sá Rebelo M., Meneghetti J.C., Gutierrez M.A., "Functional bull's eye based on three dimensional velocity information to quantify left ventricle motion in gated-SPECT", Conf Proc IEEE Eng Med Biol Soc., pp. 209-13, 2008.

[107] Viola P.A, "Alignment by Maximization of Mutual Information", Ph.D. Thesis, Massachusetts Institute of Technology, 1995.

[108] Powel M.J.D., "An efficient method for finding the minimum of a function of several variables without calculating derivatives", Computer Journal, 7, pp. 155-162, 1964.

[109] Brent R.P., "Algorithm for function minimization without derivatives", Englewood Cliffs, NJ: Prentice Hall, 1973.

[110] R. V. L. Hartley, "Transmission of information," Bell Syst. Tech. J., vol. 7, pp. 535–563, 1928.

[111] Viola P., Wells W.M. III, "Alignment by maximization of mutual information", International Conference on Computer Vision, IEEE Computer Society Press, Los Alamitos, CA., pp. 16-23, 1995.

[112] Collignon A., Vandermeulen A., Suetens P., Marchal G., "3D Multi-modality Medical Image Registration Based on Information Theory", Computational Imaging and Vision 3, pp. 263-274, Kluwer Academic, Dordrechth.

[113] Studholme C., Hill D.L.G., Hawkes D.J., "An overlap invariant entropy measure of 3D medical image alignment", Pattern Recognit., vol. 32, no. 1, pp. 71–86, 1999.

[114] Maes F., Collignon A., Vandermeulen D., Marchal G., Suetens P., "Multimodality image registration by maximization of mutual information", IEEE Trans Med Imaging., vol. 16, no. 2, pp. 187-98, 1997.

[115] Pluim J.P.W., Maintz J.B.A., Viergever M.A., “Interpolation Artefacts in Mutual Information-Based Image Registration”, Computer Vision and Image Understanding, vol. 77, no. 9, pp. 211-232, 2000.

[116] Chen H., Varshney P.K., “Mutual Information-Based CT-MR Brain Image Registration Using Generalized Partial Volume Joint Histogram Estimation”, IEEE Transactions on Medical Imaging, vol. 22, no. 9, pp. 1111-1119, 2003.

[117] Lu X., Zhang S., Su H., Chen Y., “Mutual information-based multimodal image registration using a novel joint histogram estimation”, Comput Med Imaging Graph., vol. 32, no. 3, pp. 202-209, 2008.

[118] Seppa M., “Continuous Sampling in Mutual Information”, IEEE Transactions on Image Processing, vol. 17, no.5, pp. 823-826, 2008.

[119] Makela T., Clarysse P., Sipila O., Pauna N., Pham Q.C., Katila T., Magnin I.E., “A Review of Cardiac Image Registration Methods”, IEEE Transactions on Medical Imaging, vol. 21, no.9, pp. 1011-1021, 2002.

[120] Besl P.J., McKay N.D., “A Method for Registration of 3D shapes”, IEEE Transactions on Pattern Recognition and Machine Intelligence, vol. 14, no.2, pp. 239-256, 1992.

[121] Zheng G., “Effective incorporation of spatial information in a mutual information based 3D-2D registration of a CT volume to X-ray images”, Int Conf Med Image Comput Comput Assist Interv., vol. 11, pt. 2, pp. 922-929, 2008.

[122] Maes F., Vandermeulen D., Suetens P., “Comparative evaluation of multiresolution optimization strategies for multimodality image registration by maximization of mutual information”, Med Image Anal., vol. 3, no. 4, pp. 373-86, 1999.

[123] Chenoune Y., Bouaoune Y., Delechelle E., Petit E., Garot J., Rahmouni A., “MR/CT Multimodal Registration of Short-Axis Slices in CT Volumes”, Proceedings of

the 29th Annual International Conference of the IEEE EMBS, Cite Internationale, Lyon, France, pp. 4496-4499, 2007.

[124] Wells III W.M., Viola P., Atsumi H., Nakajima S., Kikinis R., "Multi-modal volume registration by maximization of mutual information", Medical Image Analysis, vol. 1, no. 1, pp. 35-51, 1996.

[125] Bulow H., Dooley L., Wermser D., "Application of principal axes for registration of NMR image", Pattern Recognition Letters, vol. 21, pp. 329-336, 2000.

[126] Lu Z., Chen W., "Fast and Robust 3-D Image Registration Algorithm Based on Principal Component Analysis", Int. Conf. on Bioinformatics and Biomedical Engineering, pp. 872-875, 2007.

[127] Sturm B., Powell K.A., Stillman A.E., White R.D., "Registration of 3D CT angiography and cardiac MR images in coronary artery disease patients", Int. J. of Cardiovascular Imaging, vol. 19, pp. 281-293, 2003.

[128] Hurtut T., Cheriet F., Joncas J., Dansereau J., "Enhancement and Segmentation of Scar Color Images after a Scoliosis Surgery", Digital Imaging Computing: Technique and Applications (DICTA), Sydney IAPR & IEEE Conference, pp. 233-242, 2003.

[129] Kadoury S., Cheriet F., "X-ray image restoration with adaptive PDE filter for an accurate 3D reconstruction of the human spine", Proc. Int. Conf. Comp. Assisted Radiol. Surg., vol. 1, pp. 470, 2006.

[130] Weickert J., "Coherence-Enhancing Diffusion Filtering", Int. J. of Comp. Vision, vol. 31, pp. 111-127, 1999.

[131] Osher S., Rudin L.I., "Feature-oriented image enhancement using shock filters", SIAM Journal on Numerical Analysis, vol. 27, no. 4, pp. 919-940, 1990.

[132] Alvarez L., Mazorra L., “Signal and image restoration using shock filters and anisotropic diffusion”, SIAM Journal on Numerical Analysis, vol. 31, no. 2, pp. 590-605, 1994.

[133] Remaki L., Cheriet M., “Numerical schemes of shock filter models for image enhancement and restoration," Journal of Mathematical Imaging and Vision, vol. 2, pp. 129-143, 2003.

[134] Studholme C., Hill D., Hawkes D., “An overlap invariant entropy measure of 3D medical image alignment”, Pattern Recognition, vol. 32, no.1, pp. 71-86, 1999.

[135] Pluim J.P.W., Fitzpatrick J.M., “Image Registration”, IEEE Transactions on Medical Imaging, vol. 22, no. 11, pp.1341- 1343, 2003

[136] Hill D.L.G., Batchelor P.G., Holden M., Hawkes D. J., “Medical image registration,” Phys. Med. Biol., vol. 46, pp. R1–R45, 2001.

[137] Waldura R., “Dijkstra's Shortest Path Algorithm in Java”, http://renaud.waldura.com/doc/java/dijkstra/, accessed December 2007.

[138] Pluim J.P.W., Maintz J.B.A., Viergever M.A., “Mutual Information Based Registration of Medical Images: A Survey”, Medical Imaging, IEEE Transactions on, vol. 22, no. 8, pp. 986-1004, 2003.

[139] Loeckx D., Slagmolen P., Maes F., Vandermeulen D., Suetens P., “Nonrigid image registration using conditional mutual information”, Inf Process Med Imaging., vol. 20, pp. 725-37, 2007.

[140] Pluim J.P.W., Maintz J.B.A., Viergever M.A., “Image registration by maximization of combined mutual information and gradient information”, IEEE Transactions on medical imaging, 19(8), 2000.

[141] Gan R., Chung A.C., “Multi-dimensional mutual information based robust image registration using maximum distance-gradient-magnitude”, Inf Process Med Imaging., vol. 19, pp. 210-21, 2005.

[142] Gan R., Chung A.C., Liao S., “Maximum distance-gradient for robust image registration”, Med Image Anal., vol. 12, no. 4, pp. 452-68, 2008.

[143] Haber E., Modersitzki J., “Intensity gradient based registration and fusion of multi-modal images”, Methods Inf Med., vol. 46, no. 3, pp. 292-9, 2007.

[144] Liu J., Tian J., Dai Y., “Multi-modal medical image registration based on adaptive combination of intensity and gradient field mutual information”, 28th Annual International Conference of the IEEE Engineering in Medicine and Biology Society, pp. 1429-1432, 2006.

[145] Liu J., Tian J., “Registration of Brain MRI/PET Images Based on Adaptive Combination of Intensity and Gradient Field Mutual Information”, Int J Biomed Imaging. 93479, 2007.

[146] Oghabian M.A., Mehdipour S., Alam N.R., “An Investigation on RF Non-homogeneity in MRI when Different Materials are Scanned”, Proceeding (364) Visualization, Imaging, and Image Processing – 2002.

[147] Knops Z.F., Maintz J.B., Viergever M.A., Pluim J.P., “Normalized mutual information based registration using *k*-means clustering and shading correction”, Med Image Anal., vol. 10, no. 3, pp. 432-9, 2006.

[148] Mihara H., Iriguchi N., Ueno S., “A method of RF inhomogeneity correction in MR imaging”, Magnetic Resonance Materials in Physics, Biology and Medicine 7, pp. 115-120, 1998.

[149] Guillemaud R., “Uniformity correction with homomorphic filtering on region of interest”, Proceedings International Conference on Image Processing, vol. 2, pp. 872-875, 1998.

[150] Ardizzone E., Pirrone R., Gioe C., “Illumination correction on MR images”, J Clin Monit Comput., vol. 20, no. 6, pp. 391-8, 2006.

[151] Ardizzone E., Pirrone R., Gioe' C., Gambino O., “Homomorphic Approach to RF – Inhomogeneity Removal Based on Gabor Filter”, EUROCON, 2007. The International Conference on "Computer as a Tool", pp. 323-330, 2007.

[152] Lindahl D., Palmer J., Pettersson J., White T., Lundin A., Edenbrandt L., “Scintigraphic diagnosis of coronary artery disease: myocardial bull's-eye images contain the important information”, Clin Physiol., vol. 18, no. 6, pp. 554-61, 1998.

[153] Gilardi M.C., Rizzo G., Savi A., Fazio F., “Registration of multimodal biomedical images of the heart”, Q. J., Nucl. Med., vol. 40, no. 1, pp. 142-150, 1996.

[154] Declerck J., Feldmar J., Goris M.L., Betting F., “Automatic registration and alignment on a template of cardiac stress and rest SPECT images”, IEEE Trans. Med. Imag., vol.16, pp. 727-737, 1997.

[155] Termeer M., Bescos J.O., Breeuwer M., Vilanova A., Gerritsen F., Groller M.E., “CoViCAD: Comprehensive Visualisation of Coronary Artery Disease**”**, IEEE Transactions on Visualization and Computer Graphics”, vol. 13, no. 6, pp. 1632-1639, 2007.

[156] Termeer M., Bescós J.O., Breeuwer M., Vilanova A., Gerritsen F., Gröller M.E., Nagel E., "Visualization of Myocardial Perfusion Derived from Coronary Anatomy," IEEE Transactions on Visualization and Computer Graphics, vol. 14, no. 6, pp. 1595-1602, 2008.

[157] Yao J., De Castro S., Delabays A., Masani N., Udelson J.E., Pandian N.G., “Bulls-eye display and quantitation of myocardial perfusion defects using three-dimensional contrast echocardiography”, Echocardiography., vol. 18, no. 7, pp. 581-8, 2001.

[158] Klein J.L., Garcia E.V., DePuey E.G., Campbell J., Taylor A.T., Pettigrew R.I., D'Amato P., Folks R., Alazraki N., “Reversibility bull's-eye: a new polar bull's-eye map to quantify reversibility of stress-induced SPECT thallium-201 myocardial perfusion defects”, J Nucl Med., vol. 31, no. 7, pp. 1240-6, 1990.

[159] Gnanasegaran G., Buscombe J.R., Hilson A.J.W., “Use of Quantification in Cardiac Reporting: How does it change the Clinical Result?”, World Journal of Nuclear Medicine, vol. 4, no. 4, 2005.

[160] Castillo E., Lima J.A.C., Bluemke D.A., “Regional Myocardial Function: Advances in MR Imaging and Analysis”, RadioGraphics, 23, pp. S127–S140, 2003.

[161] Johnson T.K., Hasegawa D.L., Sklar J., Hendee W.R., Steele P.P., “Early description of "bull's-eye" plot for emission cardiac tomography”, J Nucl Med., vol. 29. no. 2, pp. 267-8, 1988.

[162] Klein C., Nekolla S.G., Bengel F.M., Momose M., Sammer A., Haas F., Schnackenburg B., Delius W., Mudra H., Wolfram D., Schwaiger M., “Assessment of myocardium viability with contrast-enhanced magnetic resonance imaging: comparison with positron emission tomography”, Circulation, vol. 105, no. 2, pp. 162-167, 2002.

[163] Chen T., Chung S., Axel L., “2D motion analysis of long axis cardiac tagged MRI”, Med Image Comput Comput Assist Interv Int Conf Med Image Comput Comput Assist Interv., vol. 10, pt. 3, pp. 469-76, 2007.

[164] Shekhar R., Zagrodsky V., Castro-Pareja C.R., Walimbe V., Jagadeesh J.M., “High-speed registration of three- and four-dimensional medical images by using voxel similarity”, Radiographics., vol. 23, no. 6, pp. 1673-81, 2003.

[165] Shams R., Barnes S., “Speeding up Mutual Information Computation Using NVIDIA CUDA Hardware”, 9th Biennial Conference of the Australian Pattern Recognition Society on Digital Image Computing Techniques and Applications, pp. 555-560, 2007.

[166] Yuping Lin; Medioni, G., “Mutual information computation and maximization using GPU”, IEEE Computer Society Conference on Computer Vision and Pattern Recognition Workshops, pp. 1-6, 2008.

[167] Shams R., Kennedy R. A., “Efficient Histogram Algorithms for NVIDIA CUDA Compatible Devices”, Proc. Int. Conf. on Signal Processing and Communications Systems (ICSPCS), Australia, pp. 418-422, 2007.

[168] Bookstein F.L., “Principal Warps: Thin-Plate Splines and the Decomposition of Deformations”, IEEE Transactions on Pattern Analysis and Machine Intelligence, vol. 11, no. 6, 1989.

[169] Rohr K., Stiehl H.S., Sprengel R., Buzug T.M., Weese J., Kuhn M.H., “Landmark-Based Elastic Registration Using Approximating Thin-Plate Splines”, IEEE Trans. Med. Im., vol. 20, no. 6, 2001.

[170] Chen T., Wang X., Metaxas D., Axel L., “Fast motion tracking of tagged MRI using angle-preserving meshless registration”, Int Conf Med Image Comput Comput Assist Interv., vol. 11, pt. 2, pp. 313-320, 2008.

[171] McInerney T., Terzopoulos D., “A dynamic finite element surface model for segmentation and tracking in multidimensional medical images with application to cardiac 4D image analysis”, Comput Med Imaging Graph., vol. 19, no. 1, pp. 69-83, 1995.

[172] Slomka P.J., Nishina H., Berman D.S., Kang X., Akincioglu C., Friedman J.D., Hayes S.W., Aladl U.E., Germano G., “"Motion-frozen" display and quantification of myocardial perfusion”,. J Nucl Med., vol. 45, no. 7, pp. 1128-34, 2004.

[173] Lauschke A., "Shortest Path Problem", http://mathworld.wolfram.com/ShortestPathProblem.html, 1999-2007 Wolfram Research, Inc., accessed February 2009.

[174] Martinez D., Velho L., Carvalho P.C., "Computing Geodesics on Triangular Meshes", Computers & Graphics Journal, Vol. 29, No. 5, 2005.

[175] Termeer M., Bescós J.O., Breeuwer M., Vilanova A., Gerritsen F., Gröller M.E., Nagel E., "Patient-Specific Coronary Artery Supply Territory AHA Diagrams", Abstracts of the 12th Annual SCMR Scientific Sessions, Journal of Cardiovascular Magnetic Resonance, pp. 164-165, 2009.

[176] Beliveau P., Setser R., Cheriet F., O'Donnell T., "Patient-specific coronary territory maps", Proceedings Vol. 6511, 2007.

[177] Dijkstra E. W., "A Note on Two Problems in Connection with Graphs", Numerische Mathematik, vol. 1, pp. 269–271, 1959.

[178] Ubachs J.F., Engblom H., Hedström E., Selvester R.H., Knippenberg S.A., Wagner G.S., Gorgels A.P., Arheden H., "Location of myocardium at risk in patients with first-time ST-elevation infarction: comparison among single photon emission computed tomography, magnetic resonance imaging, and electrocardiography", Journal of Electrocardiology, vol. 42, no. 2, pp. 198-203, 2009.

[179] Brandt P.W.T., Partridge J.B., Wattie W.J., "Coronary angiography: method of presentation of the arteriogram report and a scoring system", Clin Radiol, vol. 28, pp. 361-365, 1997.

[180] Sensky P.R., Hudson N.M., Keal R.P., Samani N.J., Cherryman G.R., "Interpreting regional myocardial magnetic resonance imaging data: a new method for collation with angiographic findings in patients with coronary artery disease", Clin Radiol, vol. 57, pp. 498-501, 2002.

[181] Castro-Pareja C.R., Jagadeesh J.M., Shekhar R., “FAIR: a hardware architecture for real-time 3-D image registration”, IEEE Trans Inf Technol Biomed., vol. 7, no. 4, pp. 426-34, 2003.

[182] O'Donnell T., Funka-Lea G., "3-D Cardiac Volume Analysis Using Magnetic Resonance Imaging," Fourth IEEE Workshop on Applications of Computer Vision, pp. 240, 1998.

[183] Grady L., “Fast, Quality, Segmentation of Large Volumes: Isoperimetric Distance Trees”, Lecture notes in computer science, 9th European Conference on Computer Vision, Part III, Lecture Notes in Computer Vision, vol. 3953, pp. 449-462, 2006.

APPENDIX A - PUBLICATIONS

Reference of the articles presented, in order of presentation:

1 - Beliveau P., Setser R.M., Cheriet F., O'Donnell T., "Patient-specific coronary territory maps", in SPIE Medical Imaging 2007, Proceedings vol. 6511.

2 - Beliveau P., Setser R.M., Cheriet F., White R.D., O'Donnell T., "Computation of Coronary Perfusion Territories from CT Angiography", in 34th Annual Computers in Cardiology Conference, vol. 34, pp. 753-756, 2007.

Patient-Specific Coronary Territory Maps

Pascale Beliveau[1,2], Randolph Setser[3], Farida Cheriet[1] , Thomas O'Donnell[2]

[1]Dept of Computer Engineering, École Polytechnique Montreal, Montreal, QC
[2] Dept of Imaging and Visualization, Siemens Corporate Research, Princeton, NJ 08540
[3] Dept of Diagnostic Radiology, Cleveland Clinic Foundation, Cleveland OH, 44195

ABSTRACT

It is standard practice for physicians to rely on empirical, population based models to define the relationship between regions of left ventricular (LV) myocardium and the coronary arteries which supply them with blood. Physicians use these models to infer the presence and location of disease within the coronary arteries based on the condition of the myocardium within their distribution (which can be established non-invasively using imaging techniques such as ultrasound or magnetic resonance imaging). However, coronary artery anatomy often varies from the assumed model distribution in the individual patient; thus, a non-invasive method to determine the correspondence between coronary artery anatomy and LV myocardium would have immediate clinical impact. This paper introduces an image-based rendering technique for visualizing maps of coronary distribution in a patient-specific approach. From an image volume derived from computed tomography (CT) images, a segmentation of the LV epicardial surface, as well as the paths of the coronary arteries, is obtained. These paths form seed points for a competitive region growing algorithm applied to the surface of the LV. A ray casting procedure in spherical coordinates from the center of the LV is then performed. The cast rays are mapped to a two-dimensional circular based surface forming our coronary distribution map. We applied our technique to a patient with known coronary artery disease and a qualitative evaluation by an expert in coronary cardiac anatomy showed promising results.

Keywords: 3D Visualization, Computer-assisted therapy, Image-based Rendering, Region Growing, Cardiovascular disease.

1. INTRODUCTION

In clinical practice, empirically-derived models which segment the left ventricle (LV) into 17 regions are commonly used to relate coronary artery anatomy to the corresponding regions of LV myocardium. Thus, the location and severity of disease in a particular coronary artery can be determined by comparing the model to regions of LV myocardium which are found to exhibit functional or perfusion deficits, or contain non-viable tissue, as determined by non-invasive imaging (e.g. ultrasound, magnetic resonance imaging). While the 17-segment model [Cerqueira] has been proven invaluable in this regard, it is an average taken over a population and not specific to an individual.

It has been shown that the coronary anatomy in the individual patient can deviate from the 17-segment model, most commonly near the LV apex. As an example, a recent study assessed the accuracy of a 17-segment LV model relating coronary anatomy with myocardial regions using monoplane coronary angiography in 135 patients [Bonow]. Although the distribution model showed good agreement with actual coronary anatomy on average, there was discordance in >4 segments in 27 patients (20%), and discordance in >5 segments in 13 patients (10%), 8 of whom had left dominant coronary distributions (the model assumes right dominance). However, the clinical impact (if any) of these errors was not addressed by that study.

Similarly, Setser et. al. [Setser], published a study which used co-registered MRI and MDCT images to assess the correspondence of individual patients (n=26) to a generic coronary distribution model. In these patients, it was found that 22 patients were discordant in at least 1 segment (85%). Overall, 17% (76/442) of myocardial segments differed from their assignment by the generic model.

Thus, as these studies indicate, although generic distribution models can accurately represent coronary anatomy on average, they are unable to account for the possibly significant variability in coronary anatomy that can exist between individuals.

In this paper, we present a method for generating a patient-specific model of the coronary territories given a segmented LV and coronary artery paths. Our ultimate goal is to employ this map with a functional image to target coronary arteries for intervention. For the purposes of this paper, however, we propose a method by which the maps may be constructed.

The paper is organized as follows: in section 2, we expose the methodology that was used to obtain the coronary maps (i.e., we describe the prerequisite data necessary and the techniques employed such as ray tracing and competitive region growing). Section 3 shows the results obtained, comparing our map with the known 17-segment model. Section 4 concludes the paper and presents the ongoing progress and future work to be done on the coronary mapping.

2. METHODOLOGY

2.1 Prerequisite Data

The proposed image-based rendering technique requires the 3D shape of the left ventricle (LV) and the 3D structure of the coronary tree acquired from a multi-detector computed tomography (MDCT). This modality was chosen for this application because MDCT images enable precise delineation of both the LV myocardium and epicardial coronary arteries. In the proposed algorithm, we assume both the existence of a segmentation of the LV myocardium (represented by a set of voxels) as well as the paths of the coronary arteries, obtained from CT volumes. In addition, we require the center of the LV as well as the orientations of the horizontal long axis (HLA), vertical long axis (VLA) and short axis (SA).

Paths of the coronary arteries are generated manually by a physician as an interpolated series of points. These paths must be classified by the physician. That is, the arteries and the diagonals which branch from them are grouped under one of three categories:

- LAD: Left Anterior Descending. This group includes the left main coronary and possibly any diagonal branches as specified by the physician.
- RCA: Right coronary artery, the posterior descending artery (PDA), and associated branches.
- LCX: Left circumflex and any branches of the LCX.

Optionally, a diagonal branch or group of branches may form its own category. This is particularly helpful when an anomalous branch irrigates a region not typically associated with its parent artery. Our formulation differs in this respect from the standard 17-segment model which contains only the three categories LAD, RCA, and CFX. We feel this ability to form new categories based on the individual's anatomy is one of the strengths of our approach.

2.2 Ray tracing

The epicardial surface is extracted from the myocardial mask in the CT volume using a ray tracing method as follows: let M be the set of n voxels M_1, M_2 … M_n which describe the myocardium volume. The short axis normal (SAN), horizontal long axis normal (HLAN), and vertical long axis normal (VLAN) form a coordinate system that may be swept out by a ray in spherical coordinates. Starting from the center of the LV, this ray is cast towards the outer surface of the heart. Stepping along this ray, the epicardial surface position is determined as the last voxel encountered that belongs to M.

2.3 Competitive Region Growing

Each region of the myocardium can be associated with the specific coronary which feeds it. We establish these regions using a competitive region growing algorithm [Adams] over the epicardial surface acquired above. The region growing is initialized with a group of seeds. These seeds are defined as the closest surface point from the ground truth coronary paths. Let the surface points be defined as the set of points *A*. Each seed point is assigned to one of the coronary categories previously identified in section 2.1. The n regions, $P_{1..n}$ into which the surface of the heart is to be divided are initially empty. The algorithm starts by finding the neighbors, k, to the points contained in P_i respecting the condition:

$$k = \left\{ x \in A \mid N(x) \in A \mid N(x) \cap \bigcup_{i=1}^{n} Pi \neq 0 \right\} \quad (1)$$

where N(x) is the set of neighbors to point x.

The following iterations consist of progressing along the surface, finding neighbors in the list of unassigned points belonging to A, and assigning them to the appropriate set P. The algorithm stops once the list of unassigned points is empty. The epicardial surface is subsequently colored, based on the regions associated with the corresponding coronaries (see Figure 5, in Results).

2.4 Coronary Map

To obtain the final coronary map, the 3D cup-like LV model is flattened to a 2D disk (i.e., we project the LV surface in 3D spherical coordinates onto a 2D polar coordinate frame). To accomplish this, from the LV segmentation, we use the center of the segmented LV chamber along with the local coordinate system based on HLAN, VLAN, and SAN. The surface of the LV is then sampled in a spherical coordinate system.

Specifically, the spherical coordinate system is centered in the chamber and has φ sweeping out the apex to base direction (longitudinally) and θ sweeping 360 degrees equatorially (Figure 1).

The apex of the LV ($\varphi = -\pi/2$) becomes the center of the disk while the base ($\varphi = \pi/2$) comprises the outer rim (in practice we do not sample all the way to $\varphi = \pi/2$, rather we stop near the valve plane, $\varphi = 7\pi/8$). The angle $\theta = 0$ points toward the lateral wall while $\theta = \pi$ points towards the septum. Rays are cast to sample the gray levels of the epicardial surface. For each ray cast, the voxels surrounding this intersection were collected and projected onto a two dimensional disk. The disk is then painted with colors representing the coronary territories computed earlier.

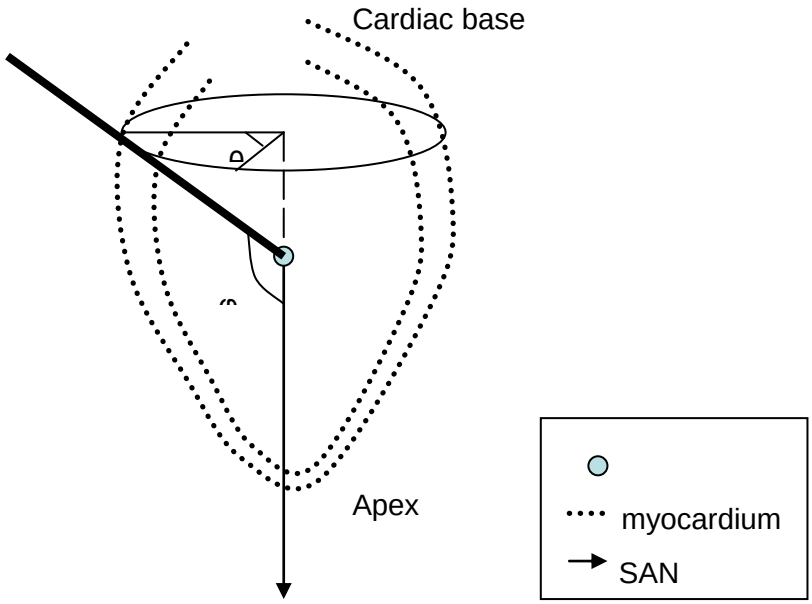

Fig. 1. Sampling the surface of the myocardium using a spherical coordinates system.

3. RESULTS

In this section, we show the results from applying our method to a specific patient with known coronary artery disease. The results were presented to an expert from the Cleveland Clinic, who validated them qualitatively.

3.1 LV projection

The coronary arteries are identified in Figure 2. Figures 3 and 4 show the result of the flattening of the cup-like LV and identify the coronaries on the flat disk.

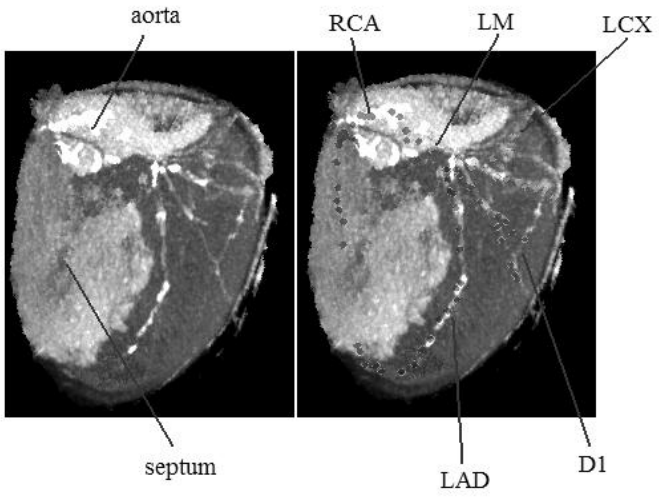

(a) (b)

Fig. 2. 3D view of the segmented LV from a patient with known coronary artery disease. Segmented coronary arteries are shown as groups of seed points in (b). Coronary arteries are labeled as follows: left main (LM), left anterior descending (LAD), left circumflex (LCX), first diagonal branch of the LAD (D1) and right coronary artery (RCA). For orientation purposes, the interventricular septum and aortic root are also shown.

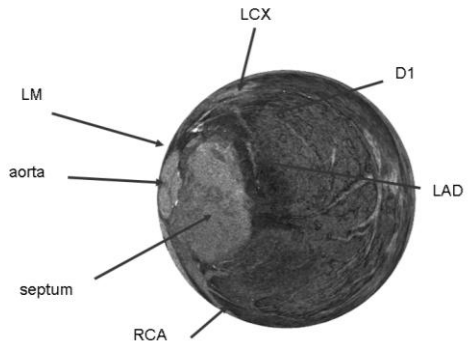

Fig. 3. Flattened disk view of the LV from the patient shown in previous figure. As above, coronary arteries are labeled as follows: left main (LM), left anterior descending (LAD), left circumflex (LCX), first diagonal branch of the LAD (D1) and right coronary artery (RCA). For orientation purposes, the interventricular septum and aortic root are also labeled.

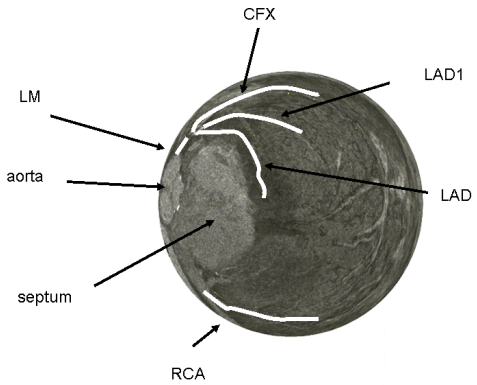

Fig. 4. As in the previous figure, flattened disk view of the LV in a patient with known coronary artery disease. Highlighted overlays are shown superimposed on the coronary arteries

3.2 Coronary Map

The results of competitive region growing are displayed in Figure 5, with the epicardial surface of the heart color coded based upon which coronary artery is expected to perfuse the underlying myocardium. Since the coronaries are situated outside the epicardial surface, for visualization purposes, the rendered values in the CT volume are those of the

myocardium and its surroundings (approximately 10mm taken outside the epicardial surface on each ray cast), explaining the white veil seen around the epicardium.

Figure 6 shows the flattened view of the LV, again color coded by coronary artery where a lexicon of the coronary arteries which were segmented for this patient has been added to the model. Each region is the result of the competitive region-growing algorithm superimposed on the flattened disk view of the LV shown in the previous section.

For comparison, the patient-specific coronary map and standard 17-segment model are shown side-by-side in Figure 7. Concentric circles have been added to the patient-specific model to allow the comparison with the 17-segment model (they do not correspond to any specific anatomy). In general, agreement between both models is considered good by the expert. Furthermore, in this patient, a diagonal branch of the LAD, identified as D1 in Figure 6 (red region), supplies myocardium typically associated with the LCX artery. The 17-segment model does not account for branch vessels, but rather lumps them with their parent artery. In the proposed patient-specific coronary map, the number of arteries included in the model is limited only by the resolution of the images and the time spent by the physician performing vessel segmentation.

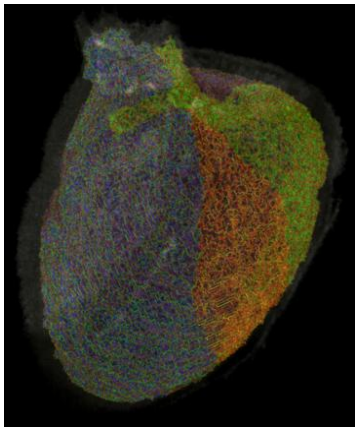

Fig. 5. The epicardium has been colored with respect to regions found with competitive region growing for each grouped coronary. The blue region is associated with the LAD, orange with the first diagonal off the LAD, green with the LCX and dark red with the RCA (last coronary group not visible in figure).

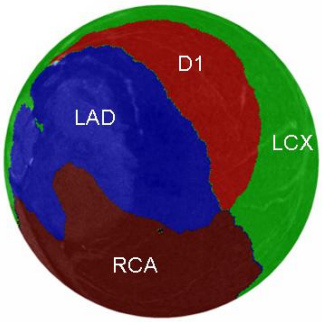

Fig. 6. Patient-specific coronary distribution map. Regions of myocardium are color-coded by coronary artery: LAD (blue), D1 (red), LCX (green), RCA (brown).

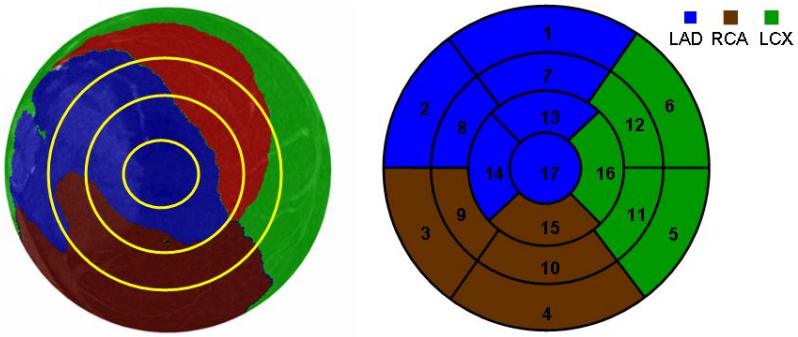

Fig. 7. Comparing the patient-specific coronary distribution map (left) with the empirically-derived 17-segment model (right).

4. CONCLUSION

In this paper, we proposed a model of the coronary irrigation which has improvements over the 17-segment model. The layout of the coronary territories over the myocardium is patient-specific and does not rely on an average over the population such as the 17-segment model. Moreover the 17-segment model is limited to 3 generic coronary arteries (LAD, LCX, and RCA) whereas the proposed model can incorporate the visualization of the territory of any branch vessels under observation by the physician.

Previous attempts to relate coronary anatomy and regional functional myocardial data have been cumbersome and manual, typically relying on coronary angiography for information regarding the coronary arteries [Brandt, Sensky]. Accordingly, these methods have not found widespread use.

Currently the LV segmentation and the vessel segmentation are done manually, or at most semi-automatically. An adaptive shock-diffusion PDE filter will be developed to attenuate the inherited distortion and noise introduced in the image formation process. The parameters of the filter will be adapted specifically to the image formation model and the structures of interest. The proposed filter will not only enhance the contrast of small vessels and the frontiers between different soft tissues but also attenuate noise to ensure the robustness and the reproducibility of the segmentation process. Furthermore, Bayesian regularization schemes will be used to integrate a priori knowledge of the vessel structures to provide coronary maps with small vessels.

An automatic segmentation of the LV and the coronary tree will provide a patient specific coronary territory maps with more details than the 17-segment model. Therefore, as technology improves, we anticipate the success of automatic segmentation algorithm will improve as well, allowing us to speculate that this type of model could be generated automatically in a near future.

We are currently validating the maps by fusing them with functional maps such as those acquired from SPECT, PET or Delayed Enhancement MR. Our future work will focus on the development of new algorithms for automatic registration of our patient-specific coronary territory maps obtained from MDCT images with functional images of the myocardium obtained from different modalities. A variational framework will be developed to perform the segmentation and the registration processes in an integrated scheme that minimizes an energy function computed from several descriptors, such as local curvature, of the structures of interest identified from the different modalities.

REFERENCES

[Cerqueira] Cerqueira M., Weissman N., et. al., "Standardized Myocardial Segmentation and Nomenclature for Tomographic Imaging of the Heart, ", Circulation 2002;105:539-542.

[Setser] Setser RM, O'Donnell TP, Smedira NG, Sabik JF, Halliburton SS, Stillman AE, White RD. Co-registered MRI myocardial viability maps, MDCT coronary angiogram displays and surgical revascularization planning: Initial experience. Radiology 2005;237:465-473.

[Brandt] Brandt PWT, Partridge JB, Wattie WJ. Coronary arteriography: method of presentation of the arteriogram report and a scoring system. Clin Radiol 1977;28:361-365.

[Sensky] Sensky PR, Hudson NM, Keal RP, Samani NJ, Cherryman GR. Interpreting regional myocardial magnetic resonance imaging data: a new method for collation with angiographic findings in patients with coronary artery disease. Clin Radiol 2002;57:498-501.

[Adams] R. Adams and L. Bischof, 'Seeded Region Growing," IEEE *Transactions on Pattern Analysis and machine intelligence*, vol. 16, No.6, June 1994.

[Bonow] Bonow RO., "Identification of Viable Myocardium," Circulation 1996;94:2674-2680.

Computation of Coronary Perfusion Territories from CT Angiography

P. Beliveau[1], R.M. Setset[2], F. Cheriet[1], R.D. White[4], T. O'Donnell[3]

[1]University of Montreal, Montreal, Quebec, Canada

[2]Cleveland Clinic, Cleveland, OH, USA

[3]Siemens Corporate Research, Princeton, NJ, USA

[4]University of Florida College of Medicine-Jacksonville, Jacksonville, FL, USA

Abstract

The assessment of myocardial viability in the left ventricle (LV) of patients with coronary artery disease is essential for determining prognosis and planning appropriate therapy. Typically, population-based models are used to associate regions containing non-viable (dead) myocardial tissue with a particular coronary artery. We propose a technique to automatically generate patient specific coronary distribution maps based on noninvasive multi-slice computed tomography (MSCT). We associate a region with the closest coronary using geodesic distance measurement over the LV epicardial surface. Projection of the coronary territories onto a flat disk allows our maps to be compared to standard models (i.e., the 17-Segment Model). This technique was applied to seven cases and an experienced cardiac radiologist examined the results for validation. Additionally, we register the patient-specific coronary territory maps with myocardial viability maps derived from noninvasive magnetic resonance imaging (MRI).

1. Introduction

Empirical models relating coronary arteries to underlying regions of left ventricular myocardium, such as the 17-segment model (see Figure 1) [1], are used routinely to describe the impact and severity of coronary artery disease. These population-based models have been shown to be accurate in large groups of patients and are a mainstay of interpretation of ultrasonographic, CT, MRI, and nuclear cardiac images. However, some studies have shown that these models are unable to take into account the clinically important variability in coronary anatomy between individuals. For instance, one recent study examined the accuracy of the 17-segment LV model in depicting the correspondence between coronary anatomy and regions of myocardium in 135 patients using monoplane coronary angiography [2]. The investigators found that the 17-segment model was accurate on average. However, in 27 patients (20%) there was discordance between the model and patient's anatomy in >4 segments. In 13 patients (10%) there was discordance in >5 segments; 8 of these patients had left dominant coronary distributions (the model assumes right dominance). Unfortunately, the clinical impact (if any) of these errors was not addressed in that study. In another study, co-registered MRI and MSCT images were used to assess the correspondence of individual patients' coronary anatomy (n=26) to a 17-segment coronary distribution model [3]. This study found that 22 patients were discordant in at least 1 segment (85%). Overall, 17% (76/442) of myocardial segments differed from their assignment by the 17-segment model.

To compute coronary territories, competitive region growing [5] was used in previous work [4]. However, it introduced a bias based on the order in which the regions expanded. In this study, we present a novel technique for deriving patient-specific coronary distribution maps from MSCT images by assigning a point on the surface to a territory based on the closest coronary.

2. Methods

In this study, validation of CT-derived coronary territory maps was performed using data from seven patients. All patients underwent both CT coronary angiography and selective x-ray coronary angiography at the Cleveland Clinic within 1 month of one another and with no interval surgical interventions (e.g. coronary bypass). CTA was performed in each patient using either a 16 slice (n=2) or 64 slice (n=5) scanner (Sensation 16/64, Siemens Medical Solutions, Forcheim, Germany), and were reconstructed at 55-70% of the cardiac cycle. Contrast agent transit time was determined using a 10-20 milliliter (mL) timing bolus (Ultravist 300, Berlex, Wayne, NJ). Furthermore, using data from 2 patients, we registered CT-derived coronary distributions maps with myocardial viability maps generated using a volume of delayed enhancement MR (DEMR) images, in order to determine the correspondence of dead tissue with the computed coronary territories.

2.1. Determining Coronary Territories

We assume the existence of a segmentation of the LV myocardium (including the LV center, and short axis and long axis normal orientations), as well as labeled segmentations of the coronary vessels (Left Anterior Descending (LAD), Left Circumflex (CFX), Right Coronary Artery (RCA) and their associated branches). A 3D polygonal triangulation model in the shape of an ellipsoid with a recursive geodesic tessellation level of 6, is scaled and projected on to the myocardial surface, which is obtained from an offline segmentation of the CT angiogram (CTA) volume to form the LV surface $\boldsymbol{S}$. The labeled coronary segmentations are projected onto $\boldsymbol{S}$ using the closest point method. For each node of $\boldsymbol{S}$, we compute the shortest path (the geodesic distance over the surface) using Dijkstra's algorithm [6, 7] to each of the projected coronary segmentations and associate that node with the closest projected coronary. The nodes of $\boldsymbol{S}$ are expressed in spherical coordinates $\boldsymbol{S}(\phi, \theta)$ and are projected onto a 2D disk, $\boldsymbol{D}$ in polar coordinates $\boldsymbol{D}(r, \theta)$ via:

$$\phi : [-\pi/2 , \pi/2] \rightarrow r\,[0,1] \quad (1)$$

In order to omit the valve plane we allow ϕ to range from $-\pi/2$ at the apex of the LV to $3\pi/8$, just before the mitral valve. The projected disk, ***D***, is then colored based on the classification of the nodes forming the territories.

2.2. Validation of Computed Coronary Territories

To validate the CTA-derived models, we used the Green Lane method, a systematic technique for assigning coronary arteries to specific myocardial regions, which has been previously described [8] and recently applied to tomographic imaging [9]. An expert cardiovascular imager manually transcribed each patient's coronary arteries, including branch vessels, onto a standard diagram, thus preserving the relative size and distribution of each vessel while allowing anatomical variation between patients. This technique is demonstrated schematically in Figure 1. From the segmentation of the myocardium in a corresponding DEMRI study [10], where dead or damaged tissues, (possibly caused by myocardial infarction) display increased signal intensity, we mapped a computed maximum intensity of the myocardial tissues onto ***S***. We then project from 3D spherical coordinates to 2D disk coordinates using (1) and register the two datasets manually, by aligning the septal insertion points and apex. We expect bright regions to be found in the territory fed by a blocked coronary.

3. Results

Figure 2 demonstrates CT-derived coronary distribution maps from 2 patients, along with the corresponding x-ray angiography derived ground truth maps. In addition, the generic 17-segment model is included for comparison. To determine the relative correspondence between the CT-derived maps and the ground truth maps, the maps from each patients

were aligned spatially and the area of correspondence (on a pixel basis) was computed. Results are shown in Table 1. Overall, the average percent correlation between CT-derived maps and the ground truth was 84%. Using this same approach, we compared the 17-segment model with the ground truth maps; in this case, the average correlation was 79%. In Figure 3 we present the registration of CT-derived maps to DEMRI studies in 2 patients. In DEMRI, dead or damaged regions exhibit increased signal intensity. From the coronary angiography studies these patients underwent, we know the condition of their coronary vessels. Our maps accurately predict the location of damaged tissues based on the information from the coronary angiograms.

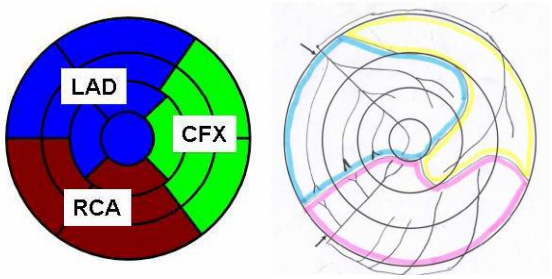

(a) (b)

Figure 1. (a) The 17-Segment Model: cross sections of the LV perpendicular to long axis (apex, apical, mid and basal portions). The septum is to the left. Three regions are found to be typically irrigated by the Left Anterior Descending (LAD), the Left Circumflex (CFX) and the Right Coronary Artery (RCA). (b) Green Lane Method: an experienced cardiac radiologist manually transcribes the coronary tree, with branch vessels, from a coronary angiogram onto a bull's eye plot. The plot is then divided into coronary distribution regions based on these projections (LAD blue, CFX yellow, RCA pink).

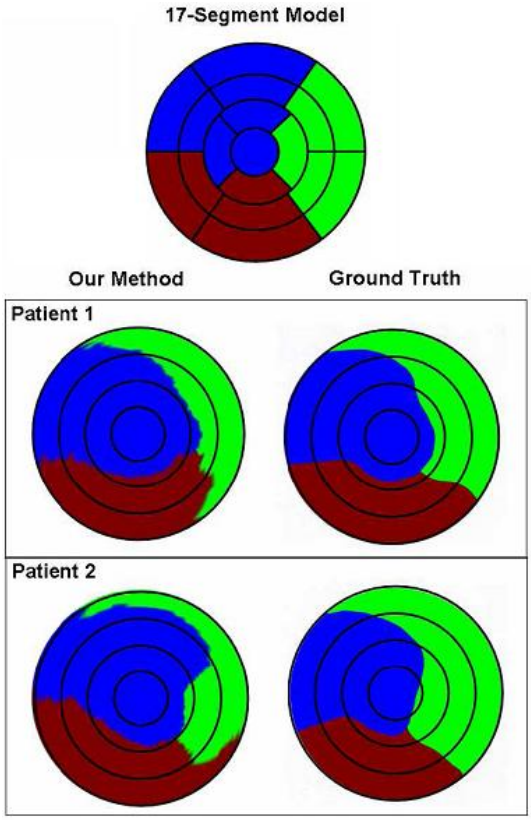

Figure 2. Comparisons of results for two patients. Top: The 17-Segment Model. Left: Our method. Right: Ground truth maps based on the Green Lane method applied to coronary angiography. In all cases, blue denotes myocardium supplied by the LAD artery, green by the CFX artery and brown by the RCA artery.

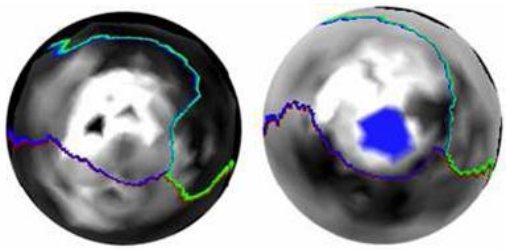

Figure 3. Coronary Territory maps registered with DEMR functional images. Boundaries between myocardial territories are denoted by colored lines: blue/green separates the LAD and the CFX territories, blue/brown separates the LAD from RCA and green/brown separates CFX and RCA. Left: Patient with 100% blockage of the LAD, no significant stenosis of the CFX, and 70% blockage of the RCA, reflected in the bright regions in the LAD territory with mildly increased signal intensity in the RCA territory. Right: Patient with occluded mid/distal LAD. No significant coronary disease was found in the CFX or RCA. The blue region in the center of the figure exists because the apical "cap" was not covered by the DEMR images.

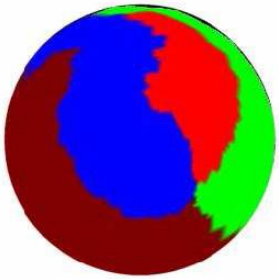

Figure 4. Our approach allows a flexible number of territories dependent upon patient characteristics. In this patient, myocardial regions perfused by a large diagonal branch of the LAD (red) are displayed separately from the LAD proper (blue), RCA (brown) and CFX (green) territories.

Table 1. Comparison on a per patient basis of our technique versus the 17-Segment Model using the Green Lane method on coronary angiography as the ground truth. Results indicate the percentage of myocardial pixels which agree between the techniques being evaluated. (p value .10).

Patient	Our Method vs. Ground Truth (%)	17-Segment vs. Ground Truth (%)
Patient 1	97.1	79.1
Patient 2	81.4	81.7
Patient 3	83.5	73
Patient 4	78.1	81.1
Patient 5	87.2	78.7
Patient 6	78.3	77.7
Patient 7	84.8	81.4
Average	84.3	79.0

4. Discussion and conclusions

One strength of our method is that it is not limited to the standard three territories. In many cases, inter-patient differences in coronary anatomy may cause a branch vessel to take on added significance. Our approach allows us to create as many territories as there are individual vessels visible in the CT images. Figure 4 illustrates an instance where an LAD (diagonal) branch is responsible for irrigating a region normally fed by the CFX. Our maps may be tailored to the specific characteristics of the patient.

Although we certainly believe that developing a patient-specific approach to relating coronary anatomy with the underlying LV myocardium represents an improvement over using empirically derived models, we also recognize several

limitations inherent in our approach as well as with our validation. First, our approach is limited by the spatiotemporal resolution of CT image acquisition (primarily temporal). The specification of myocardial regions is dependant upon a complete segmentation of the coronary tree, including branch vessels. However, complete visualization of small branch vessels, in particular the perforator vessels that supply the septum, is not currently possible with CTA to the extent that it is using coronary angiography. However, temporal resolution has decreased from approximately 250 msec to less than 100 msec over the past 3-5 years, so we anticipate the improvement of new generations of CT scanners.

In addition, there is inevitable distortion of the cardiac base during the flattening process of creating the patient-specific models. Distortion of the anatomical structures is introduced by the projection of a 3D texture onto a 2D frame, bringing stretching to the latitude rings projected onto the rings of the map.

Lastly, there are limitations with the Green Lane technique used for validation of our CTA-derived models. The LV myocardium is not visualized using coronary angiography. Thus, the Greene Lane technique represents a “best guess” by the physician as to the relationship between the coronary arteries and the underlying myocardium. However, this technique still represents one of the only systematic and validated methods for depicting this relationship. Furthermore, it mimics the mental integration of imaging data from disparate sources that has become clinical standard of cardiovascular care world-wide. Thus, we felt it was an appropriate validation method.

References

[1] Cerqueira M, Weissman N, et al. Standardized Myocardial Segmentation and Nomenclature for Tomographic Imaging of the Heart. Circulation 2002;105:539-542.

[2] Bonow RO. Identification of Viable Myocardium. Ciculation 1996;94:2674-2680.

[3] Setser RM, O’Donnell TP, Smedira NG, Sabik JF, Halliburton SS, Stillman AE, White RD. Co-registered MRI

myocardial viability maps, MDCT coronary angiogram displays and surgical revascularization planning: Initial experience. Radiology 2005;237:465-473

[4] Beliveau P, Setser R, Cheriet F, O'Donnell T, "Patient-specific coronary territory maps", Proceedings of the SPIE, Volume 6511, pp. 65111J (2007).

[5] Adams R, and Bischof L. "Seeded Regions Growing." IEEE *Transactions on Pattern Analysis and machine intelligence*, vol. 16, No.6, June 1994.

[6] Dijkstra EW. "A note on two problems in connexion with graphs", *Numerische Mathematik*, 1:269-271, 1959.

[7] Martinez D, Velho L, Carvalho PC. "Computing Geodesics on Triangular Meshes", Computer and Graphics, vol. 29, No.5, October 2005.

[8] Brandt PWT, Partridge JB, Wattie WJ. Coronary angiography: method of presentation of the arteriogram report and a scoring system. Clin Radiol 1997; 28:361-365.

[9] Sensky PR, Hudson NM, Keal RP, Samani NJ, Cherryman GR. Interpreting regional myocardial magnetic resonance imaging data: a new method for collation with angiographic findings in patients with coronary artery disease. Clin Radiol 2002;57:498-501.

[10] Hui L, O'Donnell T, "A 3-D Statistical Shape Model for the Left Ventricle of the Heart," Proceedings of Medical Image Computing and Computer-Asisted Intervention, 2001.